


5-2018

Glucose Level Estimation Based on Invasive Electrochemical, and Non-Invasive Optical Sensing Methods

Sanghamitra Mandal
University of Arkansas, Fayetteville

Follow this and additional works at: <http://scholarworks.uark.edu/etd>

 Part of the [Electronic Devices and Semiconductor Manufacturing Commons](#), [Nanoscience and Nanotechnology Commons](#), [Nanotechnology Fabrication Commons](#), and the [Semiconductor and Optical Materials Commons](#)

Recommended Citation

Mandal, Sanghamitra, "Glucose Level Estimation Based on Invasive Electrochemical, and Non-Invasive Optical Sensing Methods" (2018). *Theses and Dissertations*. 2731.
<http://scholarworks.uark.edu/etd/2731>

This Dissertation is brought to you for free and open access by ScholarWorks@UARK. It has been accepted for inclusion in Theses and Dissertations by an authorized administrator of ScholarWorks@UARK. For more information, please contact scholar@uark.edu, ccmiddle@uark.edu.

Glucose Level Estimation Based on Invasive Electrochemical, and Non-Invasive
Optical Sensing Methods

A dissertation submitted in partial fulfillment
of the requirements for the degree of
Doctor of Philosophy in Engineering with a concentration in Electrical Engineering

by

Sanghamitra Mandal
Uttar Pradesh Technical University
Bachelor of Technology in Electrical and Electronics Engineering, 2011
University of Sheffield
Master of Science in Semiconductor Photonics and Electronics Engineering, 2012

May 2018
University of Arkansas

This dissertation is approved for recommendation to the Graduate Council.

Omar Manasreh, Ph.D.
Dissertation Director

Simon Ang, Ph.D.
Committee Member

Jiali Li, Ph.D.
Committee Member

Jingxian Wu, Ph.D.
Committee Member

Timothy. J. Muldoon, M.D.
Committee Member

ABSTRACT

The purpose of this research is to design and fabricate sensors for glucose detection using inexpensive approaches. My first research approach is the fabrication of an amperometric electrochemical glucose sensor, by exploiting the optical properties of semiconductors and structural properties of nanostructures, to enhance the sensor sensitivity and response time. Enzymatic electrochemical sensors are fabricated using two different mechanisms: (1) the low-temperature hydrothermal synthesis of zinc oxide nanorods, and (2) the rapid metal-assisted chemical etching of silicon (Si) to synthesize Si nanowires. The concept of gold nano-electrode ensembles is then employed to the sensors in order to boost the current sensitivities by enhancing the rate of electron transfer during the electrochemical reaction. High crystallinity and good alignment of the nanostructures lead to increase in the electrode surface area, thereby leading to higher current sensitivities compared to other published works.

My second research approach is to design an optical sensor for evaluating long-term glycemic state in diabetic patients. Glycated hemoglobin (HbA1c) is a minor component of blood hemoglobin to which glucose is bound. The HbA1c test is a common medical test used to indicate the average blood glucose level over the past 12-16 weeks. The National Institute of Diabetes and Digestive and Kidney Diseases has established a direct relationship between the percentage of HbA1c and the blood sugar level. Our sensor instrumentation design is based on the Beer's law of optical absorption. Major device components include two commercial light emitting diodes, a cuvette holder, a Si photodiode, and an ATmega328P microcontroller. It is observed that the absorbance of diluted HbA1c samples and the corresponding photodiode output voltage are inversely related. The photodiode voltages as a function of HbA1c percentage concentrations show an exponentially decaying curve. An algorithm for multiple variable

regression analysis is then used for sensor calibration. The percentage of HbA1c is then anticipated based on the obtained output voltage using the calibrated curve results. The proposed portable optical sensor proves to be a promising step towards the prediction of the long-term glycemic levels in diabetic and pre-diabetic patients non-invasively.

ACKNOWLEDGEMENTS

I want to thank my research advisor and dissertation director, Prof. Omar Manasreh for making my research experience productive and stimulating. Under his supervision, I learned how to define a research problem, find a solution to it, and finally publish the results. It is a great honor to be one of Prof. Manasreh's Ph.D. students and I really appreciate all the time he took in guiding me throughout the course of my doctoral studies. Besides my advisor, I would like to thank my dissertation committee members Prof. Jiali Li, Prof. Timothy J. Muldoon, Prof. Jingxian Wu, and Prof. Simon Ang for their insightful comments and continuous encouragement. I express my sincere gratitude toward Dr. Muldoon for agreeing to serve on my dissertation committee on a short notice and for his ideas, suggestions, and the wealth of knowledge that helped me reach this point. I am grateful to Prof. Ang for allowing me to access and work at his laboratory during my doctoral research.

As a member of the Optoelectronics Laboratory at the University of Arkansas, Fayetteville, I take this opportunity to thank my fellow lab mates Mohammed Marie, Ramesh Vasan, Ahmad Nusir, Haider B. Salman, Wafaa Gebril, and Raad Haleoot for their continuous help and collaborative efforts in research. Special thanks to Vidit Agrawal, who was very important in the success of my Ph. D, for being the greatest source of my emotional support and for sharing his excellent knowledge.

Lastly, I would like to express my deepest gratitude to my parents and younger brother, who believed in me and supported me throughout my life. This dissertation would not have been possible without their warm love, continued patience and understanding.

TABLE OF CONTENTS

CHAPTER 1. INTRODUCTION.....	1
1.1 Literature Review.....	2
1.2 Motivation	6
1.3 Dissertation Objectives	8
1.4 Material Characterization Equipment	9
1.4.1 X-Ray Diffraction.....	9
1.4.2 Scanning Electron Microscopy	10
1.4.3 Absorbance Spectroscopy.....	12
1.4.4 Micro-Raman Spectroscopy.....	14
1.4.5 Electron Beam Evaporation	16
1.4.6 Source meter Keithley 2410.....	17
1.4.7 Gamry Reference 600 Potentiostat	18
1.5 References	19
CHAPTER 2. ELECTROCHEMICAL GLUCOSE SENSOR BASED ON ZINC OXIDE NANORODS.....	23
2.1 Chapter Overview.....	23
Abstract	23
2.2 Introduction	24
2.3 Experiment.....	25
2.4 Discussion.....	26
2.5 Conclusion.....	33
Appendix	34
2.6 Chapter Summary	34
2.7 References	34
CHAPTER 3. ELECTROCHEMICAL GLUCOSE SENSOR BASED ON SILICON NANOWIRES	37
3.1 Chapter Overview.....	37
Abstract	37
3.2 Introduction	38
3.3 Sensor Design and Fabrication.....	39
3.3.1 Silicon Nanowires Synthesis	39
3.3.2 Sensor Fabrication and Characterization	40
3.4 Results and Discussion.....	41

3.4.1 Structural and Optical Characterization of Si nanowires.....	41
3.3.2 Electrochemical Characterization and Testing of the Sensor	43
3.5 Conclusion	46
3.6 Chapter Summary	47
3.7 References	47
CHAPTER 4. ELECTROCHEMICAL GLUCOSE SENSOR BASED ON ZINC OXIDE NANORODS AND GOLD NANO-ELECTRODE ENSEMBLES.....	49
4.1 Chapter Overview	49
Abstract	49
4.2 Introduction	50
4.3 Experimental.....	52
4.3.1 Hydrothermal synthesis of ZnO nanorods.....	52
4.2.2 Electrochemical Glucose Sensor Design.....	54
4.4 Results and Discussion.....	54
4.4.1 Structural and optical characterization of ZnO nanorods	54
4.4.2 Electrochemical characterization of glucose sensor	58
4.4.2.1 Cyclic Voltammetry	60
4.4.2.2 Amperometric response to glucose	62
4.5 Conclusion.....	65
4.6 Chapter Summary	66
4.7 References	67
CHAPTER 5. OPTICAL GLUCOSE SENSOR PROTOTYPE DESIGN.....	70
5.1 Chapter Overview	70
Abstract	70
5.2 Introduction	71
5.3 Methodology.....	73
5.4 Results and Discussion.....	75
5.4.1 Molar Absorption Coefficient Calculation.....	80
5.4.2 Estimation of HbA1c percentage in a solution	85
5.5 Conclusions	86
Appendix A	88
Appendix B.....	94
Appendix C.....	96
5.6 Chapter Summary	97
5.7 References	97

CHAPTER 6. CONCLUSION	101
6.1 Summary of the Dissertation	101
6.2 Research Limitations and Recommendations.....	103
6.3 Future works	105

LIST OF FIGURES

Figure 1. 1	Schematic representation for the formation of glycated hemoglobin	5
Figure 1. 2	Diabetic, Pre-diabetic, and normal levels of percentage HbA1c.	7
Figure 1. 3	A schematic of incident rays interacting with the sample leading to constructive interference thereby satisfying Bragg’s Law.	9
Figure 1. 4	Philips PW-3040 XPert MRD High Resolution X-Ray Diffractometer [39].....	10
Figure 1. 5	FEI XL-30 Environmental Scanning Electron Microscope [40].....	12
Figure 1. 6	Snap shot of the Varian Cary 500 UV-VIS-NIR spectrophotometer in the lab.	13
Figure 1. 7	Schematic of Beer’s Law for transmitted intensity of incident light.	14
Figure 1. 8	The schematic of the Raman spectroscopy instrumentation.....	15
Figure 1. 9	Snap shot of the LabRAM HR Evolution – Horiba Raman-PL microscope in the lab.	16
Figure 1.10	Snap shot of the Angstrom Nexdep Electron Beam Evaporator in the lab.	17
Figure 1. 11	Snap shot of the Keithley 2410 source meter used in the lab.....	18
Figure 1. 12	Gamry Reference 600 potentiostat (at the High-Density Electronics Center, Engineering Research Center, University of Arkansas, Fayetteville).....	19
Figure 2. 1	(a) Absorbance spectrum of hydrothermally grown ZnO nanorods measured at room temperature. (b) Micro-Raman spectrum for ZnO nanorods grown on ITO coated glass substrate after hot plate annealing at 120°C.....	28
Figure 2. 2	(a) SEM image of ZnO nanorods grown using the sol-gel hydrothermal method on ITO and measured at room temperature. (b) Gonio-XRD pattern of ZnO nanorods at room temperature.	29
Figure 2. 3	(a) Nafion/GOx/ZnO nanorods/ITO electrode. (b) Schematic illustration of the electrochemical test cell with anode and cathode immersed in PBS.	30
Figure 2. 4	(a) Calibration curve plotted using the amperometric response measured at a potential of 0.80 V, for glucose concentration ranging from 0.01 – 20.0 mM, (b) Cyclic-voltammogram of electrochemical glucose sensor for a potential ranging from -0.80 V – 0.80 V with a sweep rate of 100 mV/sec.	32
Figure 3. 1	Schematic showing (a) Si nanowires on Si wafer with 50 nm coating of Au (b) Au NEEs in between Si nanowires.	40
Figure 3. 2	Absorbance spectrum of bare Si and Si nanowires. Inset: SEM image illustrating the top view of Si nanowires synthesized using MACE.	42
Figure 3. 3	Micro-Raman spectrum of bare Si wafer and Si nanowires measured at room temperature.	43
Figure 3. 4	Cyclic voltammograms obtained in the presence and absence (dotted line) of glucose at a sweep rate of 100, 200, and 300 mV/s.....	44
Figure 3. 5	Calibration curve derived from the amperometric measurements performed for a glucose concentration ranging from 0.01 – 7.0 mM. Inset: Steady state amperometric measurements at a constant potential of 0.60 V, for successive addition of 0.50 mM glucose.	46
Figure 4. 1	X-ray diffraction spectra measured at room temperature for as-grown ZnO nanorods on (a) ITO substrate (b) Au/glass substrate.....	56

Figure 4. 2	SEM images of ZnO nanorods grown using the hydrothermal sol-gel technique on (a) ITO and (b) Au.	57
Figure 4. 3	Micro-Raman spectra of as-grown ZnO nanorods on ITO (dotted line) and Au (straight line) measured at room temperature.	58
Figure 4. 4	Schematic illustration of (a) the working electrode with ZnO nanorods on Au/Ti/glass substrate, immobilized with GOx and covered with nafion membrane (b) the Au nanoelectrodes ensembles in between nanorods (c) experimental set up for the amperometric test carried at room temperature.....	60
Figure 4. 5	Cyclic voltammograms measured at room temperature for (a) ZnO nanorods on Au in the presence and absence of glucose (b) ZnO nanorods on ITO in the presence and absence of glucose (c) ZnO nanorods on Au in the presence of glucose at different scan rates of 20 mV/s, 50 mV/s, and 100 mV/s (d) ZnO nanorods on Au and ITO in the presence of glucose (e) ZnO nanorods on Au in the presence (straight line) and absence (dashed line) of glucose compared to sample without ZnO nanorods (dotted line) (f) ZnO nanorods on ITO in the presence (dotted line) and absence (green) of glucose compared to sample without ZnO nanorods (straight line).....	62
Figure 4. 6	Calibration curve of sensors at different glucose concentrations for an applied oxidation potential of 0.15 V. Inset: Amperometric response of sensors to successive additions of glucose with increasing molarity from 0.01 mM – 11.0 mM after every 10 s time at an applied potential of 0.15 V.....	64
Figure 5. 1	(a) The schematic of the experimental setup used to calibrate and test glycated hemoglobin concentration. (b) Snapshots of the designed prototype.	75
Figure 5. 2	Schematic showing a cuvette containing a red sample under the influence of (a) white light, we see the red color of the sample and (b) blue light, all photons are absorbed, and no photons are transmitted.....	78
Figure 5. 3	Electroluminescence of green and yellow LED measured at room temperature compared to the absorbance of Glycohemoglobin A1c, crystal violet, and rhodamine 6g solutions.	80
Figure 5. 4	Photodiode output voltage (averaged over 500 voltage readings) as a function of concentration of (a) Crystal Violet synthetic dye using the yellow LED and (b) Rhodamine 6g fluorescent dye using the green LED. The data points are fitted to an exponentially decaying equation model via a three-variable regression analysis to find molar absorption coefficient.	82
Figure 5. 5	(a) The absorption spectra of diluted concentrations of glycohemoglobin A1c solutions measured at room-temperature. (b) Photodiode output voltage (averaged over 500 voltage readings) as a function of concentration for diluted concentrations of glycated hemoglobin using green LED and (c) yellow LED. The data points are fitted to an exponentially decaying equation using a three-variable regression analysis.	85

LIST OF TABLES

Table 1. 1 Chart showing the relationship between percentage of HbA1c and the estimated average blood glucose levels in humans.....	6
Table 2. 1 Performance parameters of peer reported electrochemical glucose sensors.	33
Table 4. 1 The Performance Parameters for Glucose Sensors based on different nanomaterial growth Approachs.	65
Table 5. 1 Estimated percentage of glycated hemoglobin.....	86

ABBREVIATIONS

IFG	Impaired fasting glucose
IGT	Impaired glucose tolerance
eAG	Estimated average glucose
HbA1c	Glycated hemoglobin
Hb	Hemoglobin
1D	One dimensional
2D	Two dimensional
3D	Three dimensional
DI	De-ionized
ZnO	Zinc oxide
GOx	Glucose oxidase
Si	Silicon
Au	Gold
ITO	Indium tin oxide
HF	Hydrofluoric acid
AgNO ₃	Silver nitrate
HNO ₃	Nitric acid
NEEs	Nanoelectrode ensembles
MACE	Metal assisted chemical etching
CV	Cyclic voltammetry
H ₂ O ₂	Hydrogen peroxide
PBS	Phosphate buffered saline

LOD	Limit of detection
XRD	X-ray diffraction
SEM	Scanning electron microscopy
I-V	Current-voltage
UV-Vis	Ultraviolet-visible
LED	Light emitting diode
PL	Photoluminescence
CCD	Charge-coupled device
e-beam	Electron beam

LIST OF PUBLISHED PAPERS

- Chapter 2. **Mandal, Sanghamitra**, Marie, Mohammed, and Manasreh, Omar. "Fabrication of an Electrochemical Sensor for Glucose Detection using ZnO Nanorods." *MRS Advances* (2016), vol. 1, no. 13, pp- 861-867. <https://doi.org/10.1557/adv.2016.149>
- Chapter 3. **Mandal, Sanghamitra**, Marie, Mohammed, and Manasreh, Omar. "Fabrication of nanoelectrode ensembles using silicon nanowires in an electrochemical glucose sensor." *IEEE Sensors* (2016). <https://doi.org/10.1109/ICSENS.2016.7808447>
- Chapter 4. **Mandal, Sanghamitra**, et al. "Sensitivity enhancement in an in-vitro glucose sensor using gold nanoelectrode ensembles." *Journal of Materials Science: Materials in Electronics* (2017), vol. 28, no. 7, pp-5452-5459. <https://doi.org/10.1007/s10854-016-6207-5>
- Chapter 5. **Mandal, Sanghamitra**, and M. O. Manasreh. "In-Vitro Optical Sensor designed to estimate Glycated Hemoglobin Levels." *Sensors* (2018), vol. 18, no. 4, pp-1084. <https://doi.org/10.3390/s18041084>

CHAPTER 1. INTRODUCTION

Diabetes Mellitus is a serious metabolic disease that can strike any person at any age in their life. About 422 million people around the world are diabetic [1]. The chronic disorder arises due to insulin deficiency, thereby leading to increased blood glucose levels. Over 90% of these diabetic people have developed type-2 diabetes, which occurs when the body becomes resistant to insulin or is incapable to produce enough insulin [1]. Other common forms of diabetes are (1) type-1 diabetes that usually leads to absolute insulin deficiency, and (2) gestational diabetes mellitus that emerges with onset or first recognition during pregnancy. Classification of diabetes is important for determining the clinical diagnosis and disease progression. Western countries are at a greater risk of developing diabetes, particularly type-2. Obesity, poor diet, and lack of physical activity, mainly due to population ageing account for the common reasons in such countries. Family history is an unavoidable factor leading to the development of type-2 diabetes. Diabetes mellitus is capable of affecting almost every human body system. People with diabetes are twice as likely to be affected by heart diseases, kidney failure, stroke, eye cataracts, feet amputation, or sudden mortality. Regular glucose measurement is important for determining the daily insulin dosage, food diet type, and exercise schedule. Frequent, periodic, and accurate blood glycemic level detection is therefore crucial for diabetes prone patients. Pre-diabetes is classified into two levels of glucose concentrations: (1) impaired fasting glucose (IFG) level, ranging from 5.6 to 6.9 mM/L and (2) impaired glucose tolerance (IGT) level, ranging from 7.8 to 11.0 mM/L [2]. Both IFG and IGT are known as pre-diabetes conditions, where blood glucose levels are higher than normal but not high enough to be diagnosed as type-2 diabetes. Every year, there are more than 3 million American individuals that are diagnosed by Pre-diabetes. Recently, pre-diabetes is detected by slightly raised glycated

hemoglobin A1c (HbA1c) levels. Identifying pre-diabetes and taking precautionary measures is essential in reducing the overall type-2 diabetes cases around the world [3].

1.1 Literature Review

Sensors are devices that detect and respond to any change in the physical environment. All sensors comprise of an active sensing material and a signal transducer. Sensors are broadly classified into chemical sensors and biosensors. Electrochemical sensors are a combination of chemical sensors and biosensors, where electrochemical methods are used in the construction and the working of a biosensor [4]. During 1980s, the development of glucose biosensors became an important research topic. However, in 1962, Clark and Lyons from Cincinnati Children's Hospital, for the first time proposed an electrochemical glucose sensor incorporating glucose oxidase (GOx) enzyme-based electrode [5]. Today, there exist three electrochemical methods to detect blood glucose levels in diabetic patient namely (1) invasive, (2) minimally invasive, and (3) non-invasive methods [6].

The most successful, accurate, and economical glucose measuring technique is the invasive blood glucose monitoring method. However, such self-monitoring glucose sensors require pricking of finger tissues several times a day to extract capillary blood and are associated with several long-term disadvantages. The electrochemical glucose sensors, both enzymatic and non-enzymatic, have emerged as the most investigated device technologies in the past four decades [7]. The concept of electrochemical sensors for glucose detection first emerged in 1962 [5]. Since then various electrochemical and optical approaches are used to develop cost effective and highly sensitive glucose sensors for precise glycemic measurement and control [8] [9]. Minimally invasive glucose sensors reduce pain, and the risk of bio-fouling effects and infections [10] [11]. However, inaccurate sensor measurements due to noise and patients' movements, and

skin irritations due to direct sensor contact with dermal tissue hamper the use of minimally invasive sensors. Non-invasive glucose sensor technology is the most recent technique that is pain free and is attributed to direct measurement of glucose level through body tissues from the skin, eyes, or the tongue [6]. Recently, various alternative approaches are being explored, like reverse iontophoresis [12], tear glucose dynamics [13] [14], and dielectric spectroscopy [15], to develop cost effective and highly sensitive glucose sensors for precise glycemic control. Optical sensors are the least invasive form of biological instruments. Yet, testing glucose non-invasively using optical methods have not yielded consistent results so far in literature [16]. The development of advanced optical glucose sensing technologies would lead to better selectivity, stability, and accuracy of glucose monitoring.

In the recent decade, efficient electrochemical sensors are developed by utilizing the properties of nanostructures in the working electrode. Nanostructures increase the active sensing area and have properties like good mechanical stability, light weight, enhance the current sensing capability, and reduce the sensor operating potential. Zinc oxide (ZnO) is an inorganic compound that is soluble in water. It is a low cost, non-toxic, environmental-friendly, biocompatible, and biodegradable semiconducting material. Other significant properties of ZnO are high thermal stability, large binding energy (60 meV), piezo electric response, and a direct wide band gap of 3.37 eV. ZnO has a surface work function of 5.30 eV, melting point of 1975 °C, boiling point of 2360 °C, relative molecular mass of 81.37 g mol⁻¹, and density of 5.67 g cm⁻³. The crystal lattice constants of ZnO are a=3.25 Å and c=5.21 Å. ZnO has wurtzite hexagonal crystal structure with crystallographic group P6₃mc [17]. Nanostructures and thin-films of ZnO has vast device applications in light emitting diodes (LEDs) [18] , solar cells [19], gas sensors [20] [21], and optical waveguides [22]. The most commonly used and cost-effective method to

synthesis ZnO nanorods is called the sol-gel hydrothermal method. The word hydro refers to water and thermal means heat. In other words, the hydrothermal reaction is defined as any chemical reaction that takes place at an aqueous or non-aqueous solvent at a temperature above room temperature and pressure above 1 atm in a closed system [23]. The hydrothermal sol-gel recipe of ZnO nanorods synthesis used in this research is discussed in more details in chapter 2 and 4.

Silicon (Si) is a semiconductor that is an integral part of all electronic devices. The indirect band gap of bulk Si is about 1.1 eV, and therefore Si has a very poor optical radiative efficiency and produces light outside the visible range [24]. Black Si refers to Si surfaces that have nano- or micro-structures on the surface [25]. Such Si samples have low reflection that enhances optical properties like light scattering and absorption [25]. One dimensional (1D) nanostructures exhibit different electrical, optical, and physical properties compared to bulk and quantum dots [26]. The phenomenon of quantum confinement is obeyed by 1D nanostructures that leads to the enhancement of the electron-hole recombination rate, higher band gap energy (1.6 eV), and luminescence efficiency [26]. Nanowires based electrochemical sensors exploit the advantage of nanoscopic size scale, and aspect ratio to enhance the electron transport properties during the electrochemical reaction [4]. However, the electrical conductivity of the nanowires depends upon their crystalline structure. This means lower the defects, lesser the surface scattering in the nanowires, and better the electron transport behavior. There are various synthesis techniques that are used for the synthesis of Si nanowires depending upon the required sensor application, properties, dimensions, or morphology [4]. The metal assisted chemical etching technique for Si nanowires synthesis is discussed in further details in chapter 3.

Red blood cells are biconcave disk-shaped with an average diameter of about 7.0-8.5 μm , outer thickness of 2.0-2.5 μm and central thickness of 0.8-1 μm [27]. The cytoplasmic matrix of the red blood cells consists of the hemoglobin molecules [28]. Hemoglobin is the oxygen carrying protein that gives blood its red color. The most common hemoglobin type is called Hemoglobin A, where A stands for adult. Hemoglobin A comprises of 90% all hemoglobin molecules in the red blood cell. Only about 8% of the hemoglobin A is made up of minor components called A1c, A1b, A1a and A1a2 [29]. Hemoglobin (Hb) A1c is modified hemoglobin, where non-enzymatic attachment of glucose to the N-terminal of β -chains of hemoglobin takes place [30]. The formation of HbA1c in red blood cell is shown in Fig. 1.1. The percentage of HbA1c in blood is used as an indicator of long-term blood glycaemic level.

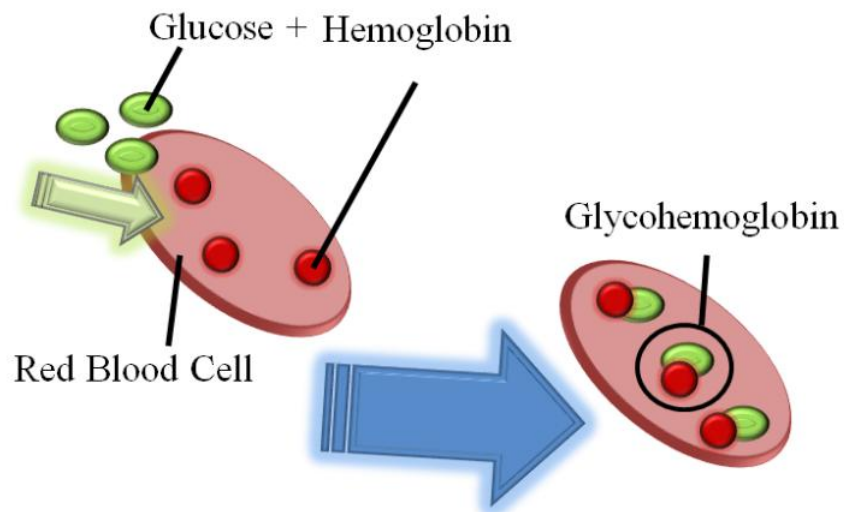


Figure 1. 1 Schematic representation for the formation of glycosylated hemoglobin

In normal individuals the HbA1c level is about 5% of the total hemoglobin but is about 15% in patients with diabetes mellitus [31]. The HbA1c level is tested to indicate the average blood glucose level over the past 12-16 weeks [32] as the average functional lifespan of red blood cells in human body is 120 days. Factors like genetic and medical conditions affect

HbA1c levels even at constant glucose levels [30]. In 1976, HbA1c was first used to monitor the degree of control of glucose metabolism in diabetic patients [33]. Since then several studies have been conducted to standardize HbA1c level in correlation to the average glucose measurements [34]. The American Diabetes Association has established the equations 1.1.1 and 1.1.2 to calculate the estimated Average Glucose (eAG) level from the percentage of HbA1c in blood hemoglobin [34], [35].

$$eAG \text{ (mmol/L)} = 1.59 \times HbA1c \text{ (\%)} - 2.59 \quad (1.1.1)$$

$$eAG \text{ (mg/dL)} = 28.7 \times HbA1c \text{ (\%)} - 46.7 \quad (1.1.2)$$

Using these equations, a direct relationship between the percentage of HbA1c and the estimated average glucose in units of mmol/L and mg/dL is established and is represented in Table 1. 1.

Table 1. 1 Chart showing the relationship between percentage of HbA1c and the estimated average blood glucose levels in humans.

HbA1c (%)	eAG (mmol/L)	eAG (mg/dL)	Stage
4	3.8	68	Super Optimal
4.5	4.6	82	
5	5.4	97	Optimal
5.5	6.2	111	Normal
6	7.0	126	Pre-diabetes
6.5	7.8	140	Diabetes
7	8.6	154	
7.5	9.4	169	
8	10.2	183	Dangerous

1.2 Motivation

Today about one out of three American adults are pre-diabetic [36]. The optimal percentage of HbA1c level for Diabetic, pre-diabetic and non-diabetic people is shown in Fig. 1.

2. Pre-diabetic people are on the path to develop type-2 diabetes and over 90% of them are unaware of their current health condition. During the pre-diabetic state, the risk of cardiovascular diseases is moderately increased. However, pre-diabetes could be treated by early diagnosis and by taking precautionary measures [36]. Continuous glucose monitoring devices play an important role toward indicating and controlling glycemic state in such patients. An alternative method to estimate glycemic level in blood is through a compound called glycated hemoglobin (HbA1c) found in red blood cells. In normal individuals, the HbA1c level is about 5% of the total hemoglobin but is about 15% in patients with poor glycemic levels [31]. The HbA1c level is tested to indicate the average blood glucose level over the past 3-4 months [32] as the average functional lifespan of red blood cells in human body is 120 days. The currently available commercial electrochemical HbA1c sensors are based on liquid chromatography, immunoassay, electrophoresis, or spectrophotometry techniques that require invasive blood extraction. The invasive needle based electrochemical sensors are associated with disadvantages like excessive pain, damaged finger tissues, and high risks of blood infections like tetanus. Therefore, there is a pressing need for the development of advanced non-invasive optical HbA1c sensors with better selectivity, stability, and accuracy.

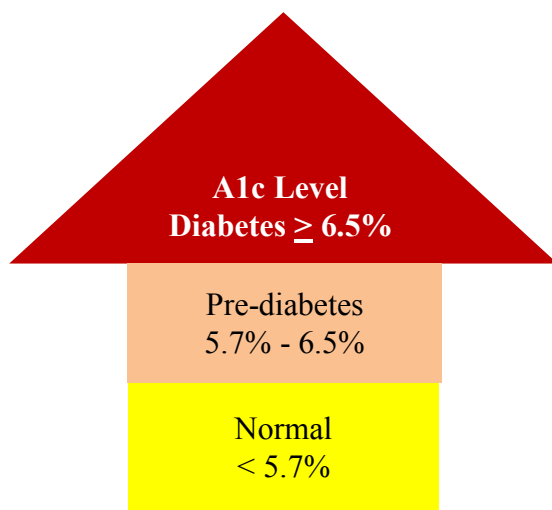


Figure 1. 2 Diabetic, Pre-diabetic, and normal levels of percentage HbA1c.

1.3 Dissertation Objectives

The first part of this dissertation aims toward the fabrication and testing of an electrochemical glucose sensor. Electrochemical sensors with high sensitivity and fast response time are fabricated by employing ZnO nanorods and Si nanowires, and gold (Au) nanoelectrodes ensembles (NEEs). Hydrothermal synthesis of ZnO nanorods and chemical synthesis of Si nanowires are discussed in detail. The structural and optical characterization of both ZnO nanorods and Si nanowires are performed via X-ray diffraction (XRD), and scanning electron microscopy (SEM) techniques and absorbance, and Micro-Raman spectroscopy techniques, respectively. The enzymatic electrochemical glucose sensor working electrodes are fabricated using enzyme GOx and nafion polymer-modified sensor surface. The sensor characterization is performed by means of the cyclic voltammetry (CV) and the amperometric techniques. We hypothesize that the presence of NEEs may contribute toward enhancement of sensor performance by reducing response time and improving current sensitivity.

The second part of my research aims at studying the feasibility of designing an optical HbA1c sensor to indicate glucose levels in recent past. A cost-effective device is designed by means of simple electronic components like LEDs, photodiode, and microcontroller. An optical method to measure the molar absorbance coefficients and the percentage concentration of HbA1c is described. Detailed explanation of the instrumentation objectives, and results obtained from testing chemical dyes and a commercial chemical assay with known HbA1c percentage level, is presented to verify the device measurements.

1.4 Material Characterization Equipment

1.4.1 X-Ray Diffraction

The X-Ray diffraction (XRD) characterization technique is used to study the composition, structure and physical properties of the materials. This is a laboratory based non-destructive analytical technique used for the study the position of the crystal at selected orientations and the atomic spacing. In 1912, Max von Laue discovered that crystalline material act as three-dimensional (3D) diffraction gratings for X-ray wavelengths similar to the spacing in a crystal lattice [37]. The principle of XRD technique is based on the constructive interference of monochromatic X-rays and the crystalline powder sample. A crystalline material has a definite order of 3D crystallinity. The interaction of the incident X-rays with the sample produces a diffracted ray such that the angle of incidence is equal to the angle of reflection and thereby satisfying the Bragg's Law. The Bragg's Law is given by equation (1.4.1), where d is the inter-planar spacing, θ is the Bragg's angle, n is the order of reflection, and λ is the X-ray wavelength. The schematic of Bragg's law is represented in Fig. 1.3.

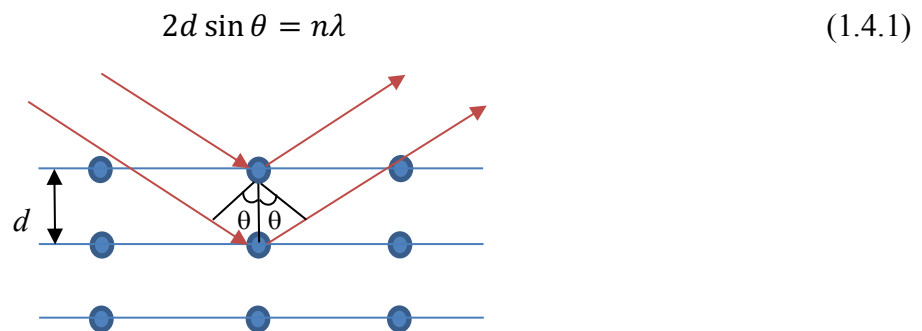


Figure 1. 3 A schematic of incident rays interacting with the sample leading to constructive interference thereby satisfying Bragg's Law.

The Philips Xpert MPD X-ray diffractometer shown in Fig. 1. 4 comprises of an X-Ray tube, a sample holder, and an X-ray detector. The X-rays are produced inside a cathode ray tube due to the heating of a filament. As a result, the electrons are produced, and accelerated towards

a target by an applied voltage, thereby bombarding the target material with electrons. The source used is a Copper Target X-Ray tube. When electrons are sufficiently energized, the inner shell electrons dislocate the target material and then the X-ray spectra are produced [38]. These X-rays are then aligned and directed onto the crystalline powder sample. The sample rotates in the path of the aligned X-ray beam at an angle of θ , and the diffractometer collects the diffracted X-rays and rotates at an angle of 2θ . The X-ray scan for the random orientation of the powdered crystalline sample varies in all directions with angles 2θ in the range from 3° to 136° .



Figure 1. 4 Philips PW-3040 XPert MRD High Resolution X-Ray Diffractometer [39]

1.4.2 Scanning Electron Microscopy

In 1948, researchers from the electrical department at Cambridge University assembled the first scanning electron microscope that produced 3D images. The scanning electron microscope consists of an electron gun that generates a highly concentrated beam of electrons

through a series of electromagnetic lenses inside a vacuum chamber. The power of the magnification depends upon the concentration of the electrons. When the sample is hit by the electron beam, it emits X-rays along with three kinds of electrons, (1) primary backscattered electrons, (2) secondary electrons, and (3) Auger electrons. The imprints of bouncing backscattered electrons is recorded and displayed in the form of 3D images. Sample preparation is a very important step to produce satisfactory images showing sample size, texture, and topography. Samples with any form of metals do not require any preparation because they respond favorably well to the electron beam. However, non-metallic samples require to be placed on a thin layer of conductive material called sputter coater. The most common sputter coater material used is Au foil that is negatively charged. Removal of water or any form of liquid is important during sample preparation. Water molecules vaporize in the vacuum creating complications for the electron beam to target the sample surface. We use the FEI XL-30 Environmental Scanning Electron Microscope shown in Fig. 1. 5 has a field emission electron gun that generates a very strong electric field capable of dissociating electrons from the atoms in the sample. The FEI XL-30 Environmental Scanning Electron Microscope operates in three modes (1) conventional high vacuum mode, (2) low vacuum mode, and (3) true environmental mode. These capabilities make it possible to scan any sample with the exception of liquids and gasses.

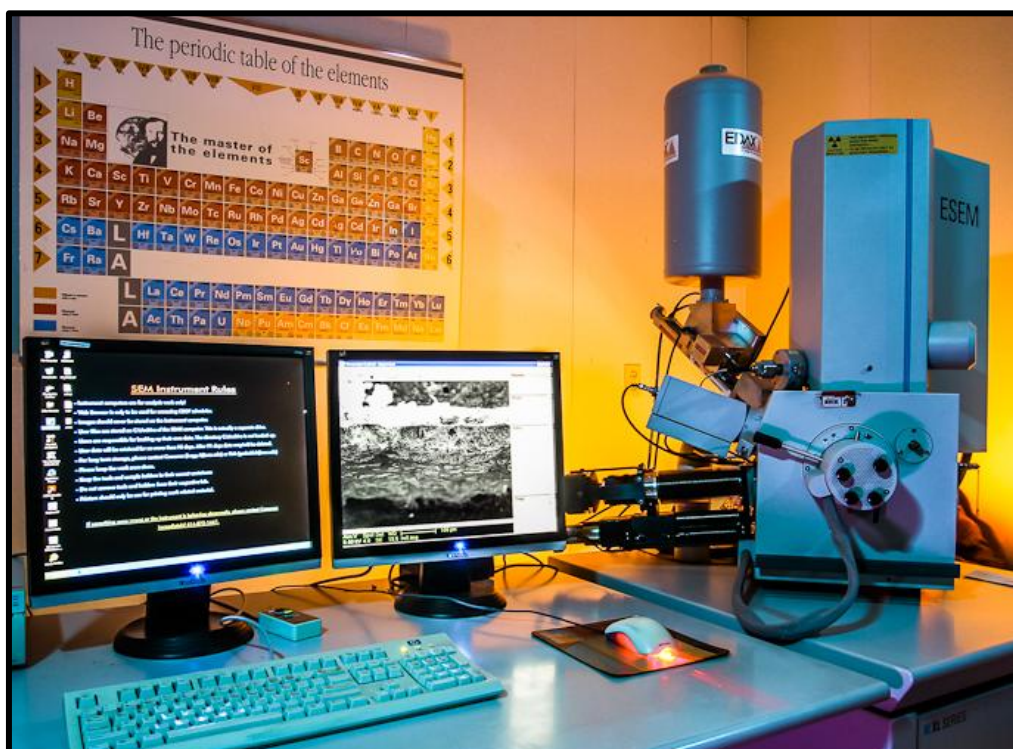


Figure 1. 5 FEI XL-30 Environmental Scanning Electron Microscope [40]

1.4.3 Absorbance Spectroscopy

The Varian Cary 500 Spectrophotometer is a UV-VIS-NIR spectrophotometer as shown in Fig. 1. 6. It is used to measure the absorbance and transmission properties of materials in the ultraviolet to near infrared wavelength range from 175 – 3300 nm. Spectrophotometers consists of (1) light sources (tungsten lamp that produces white light, ultraviolet, and near infrared light), (2) a monochromator (diffraction grating as the wavelength selector), (3) sample holder, (4) photodetector (measures the light intensity and compares to the light intensity incident on the sample), (5) signal processor, and (6) a computer readout. The absorption of photons from the light source in the ultraviolet, visible, or near infrared region of the light spectrum leads to electronic transition in the molecule of the sample. The electrons are then promoted from ground state to higher electronic states. The amount of energy absorbed from the incident light source is measured by the detector and registered as absorbance of the sample.



Figure 1. 6 Snap shot of the Varian Cary 500 UV-VIS-NIR spectrophotometer in the lab.

According to the Beer's law, the absorbance of a solution is proportional to the sample concentration and the optical path. The equation 1.4.2 represents the Beer's law equation, where ϵ is the wavelength-dependent molar absorption coefficient ($M^{-1} \text{ cm}^{-1}$), c is the concentration of the sample (M), and x is the path length of the sample holder (cm). The proportionality constant, ϵ is called the molar extinction coefficient, molar absorption coefficient, or the molar absorptivity.

$$A = \epsilon * C * x \quad (1.4.2)$$

The Beer's law relates color intensity to the sample concentration. A colored solution undergoes selective absorption when irradiated with white light. This is due to the energy associated with the electrons in the molecules of the sample. Under the effect of irradiated white light, the electrons get excited to higher energy levels. The energy depends upon the wavelength of the electromagnetic radiations. Visible light is a form of electromagnetic radiation. When light is not absorbed by the sample, it is transmitted through. Absorbance of a solution in terms of transmittance percentage is given by equation 1.4.3.

$$A = -\log \left(\frac{\%T}{100} \right) \quad (1.4.3)$$

The absorbance of light by a sample is inversely proportional to the percentage of transmittance.

The transmittance percentage is the ratio of transmitted intensity (I) and the incident light intensity (I_0) as given by equation 1.4.4.

$$\%T = \left(\frac{I}{I_0} \right) * 100 \quad (1.4.4)$$

The transmitted intensity of light (I) as a function of wavelength (λ) is given by equation 1.4.5 and Fig 1.7, where I_0 is the intensity of the light incident on the sample.

$$I(\lambda) = I_0 * \exp(-\epsilon(\lambda) * c * x) \quad (1.4.5)$$

Beer's law and its application in the assembly, design, and testing of an optical sensor is further discussed in detail in chapter 5.

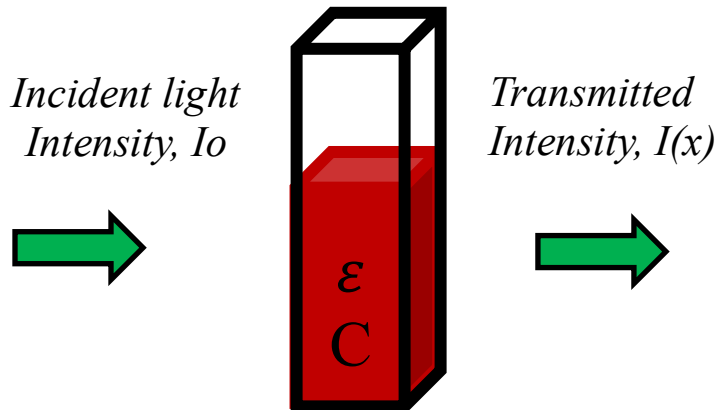


Figure 1. 7 Schematic of Beer's Law for transmitted intensity of incident light.

1.4.4 Micro-Raman Spectroscopy

The Micro-Raman spectroscopy is a non-destructive material characterization method, where a photon of light interacts with a sample to produce scattered radiation of different wavelengths. In 1928, the Indian physicist, Sir Chandrasekhara Venkata Raman first introduced the Raman spectroscopy technique that is now used to determine the molecular vibrations and rotation, effects of bonding, chemical composition, and crystal structure of the material sample.

A Raman spectroscope consists of a laser source for excitation, a sample illumination system, and spectrometer as shown in Fig 1.8. The laser source selection plays a very important role in the experimental capabilities. When the monochromatic laser radiations are incident on the sample surface, absorption, reflection, and scattering of photons take place. The analysis of wavelength of the scattered photons gives the wavelength of the incident photons (Rayleigh scattering) as well as the wavelength of the scattered photons at different wavelengths (Stokes and Anti-Stokes Raman scattering) [41]. These Raman scattered photons intensities provide the chemical, and structural information and are about 0.001% of the intensity of the laser source.

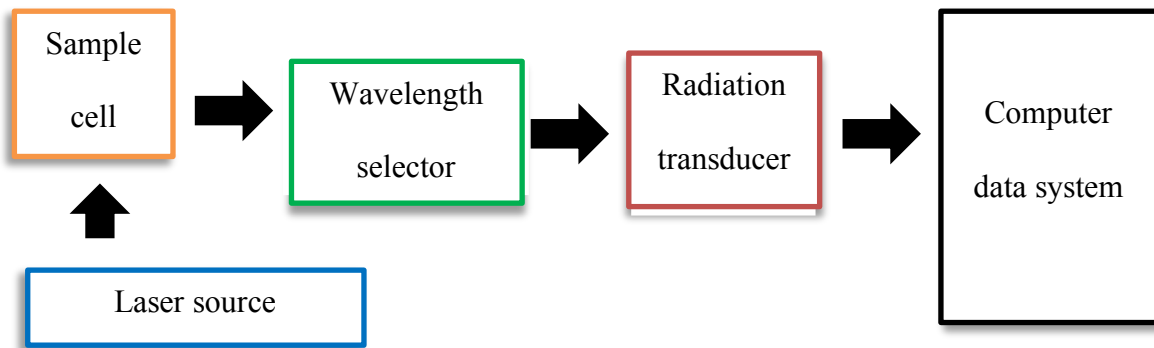


Figure 1. 8 The schematic of the Raman spectroscope instrumentation.

Figure 1. 9 shows the Horiba LabRam HR Evolution Raman-PL microscope system in our laboratory that allows both Micro-Raman and photoluminescence (PL) measurements on the same instrument. The system is designed with multi laser excitation sources (blue laser, 325 nm and red laser, 633 nm) ranging from UV to NIR wavelengths. The system is equipped with multiple detectors like the charge-coupled device (CCD) detector and InGaAs detector for a wide spectral range analysis for both Raman and PL. The Horiba Micro Raman-PL system is configured with the LabSpec 6 software platform that allows user friendly sample measurement set-up, visualization, and simple interpretation of data and final results. The Raman spectrum of a sample is displayed on the computer system that shows a number of peaks representing the

intensity and wavelength position of the Raman scattered light. The micro-Raman spectrum of ZnO nanorods presented and discussed further in chapter 2 and 4, and Si nanowires are presented in chapter 4.



Figure 1. 9 Snap shot of the LabRAM HR Evolution – Horiba Raman-PL microscope in the lab.

1.4.5 Electron Beam Evaporation

The electron beam (e-beam) evaporation technique is a physical vapor deposition technique used for thin-film deposition of high quality and high purity metals or alloys on substrates. Figure 1. 10 represents the e-beam evaporator used in our lab and is known as the Angstrom Nexdep Electron Beam Evaporator. A high voltage is applied between a tungsten filament and the vacuum chamber that accelerates a beam of electrons towards the crucible containing the metal or alloy to be deposited. The electron beam steered via electric and magnetic fields causing the source material to evaporate and deposit on the substrate. The e-beam thin-film deposition technique has advantages like (1) high deposition rates, (2) allows evaporation of high temperature elements like Au, tungsten, tantalum, or graphite, (3) dense and high purity thin-film deposition, and (4) more than one material deposition is possible via the motorized rotary pocket containing different source materials. The e-beam deposition of 50 nm

of metal Au over 10 nm of titanium used in the fabrication of electrochemical sensor working electrode is discussed further in chapter 4.



Figure 1.10 Snap shot of the Angstrom Nexdep Electron Beam Evaporator in the lab.

1.4.6 Source meter Keithley 2410

Device characterization of the electrochemical sensor (further discussed in chapter 2, 3, and 4) is performed using the Keithley 2410 source meter shown in Fig 1. 11. The model of this source meter has a maximum power rating of 20 W. The maximum current source and measuring range is up to 1 A and the maximum voltage source or measuring range is up to 1100 V. The measurement resolution is 1 pA/100 nV. We primarily use the source meter to perform the amperometric iterations at a fixed potential applied across the cathode and anode immersed in an electrochemical cell (further discussed in chapter 2, 3, and 4).



Figure 1. 11 Snap shot of the Keithley 2410 source meter used in the lab.

1.4.7 Gamry Reference 600 Potentiostat

Cyclic voltammetry (CV) is an electrochemical device characterization technique used to measure the current developing in an electrochemical cell under the effect of a range of applied potential. We derive information like the oxidation reduction potentials of the electrochemical sensor through the CV results. The CV characterization results for the fabricated electrochemical sensors based on different nanostructures are discussed further in chapter 2, 3, and 4. All the CV measurements are performed using the Gamry Reference 600 Potentiostat shown in Fig. 1. 12. The Gamry Reference 600 potentiostat is a high-performance, research grade electrochemistry testing instrument that is highly stable and produces reliable, reproducible results. The Gamry potentiostat has a USB 2.0 connection that is used to interface with the windows operating system for data analysis by means of the open source software package called Gamry Echem Analyst. The instrument has a maximum applied potential of ± 11.00 V and a maximum current rating of ± 600 A. The minimum potential step possible is $12.50 \mu\text{V}$ with a minimum rise time of less than 250 ns.



Figure 1. 12 Gamry Reference 600 potentiostat (at the High-Density Electronics Center, Engineering Research Center, University of Arkansas, Fayetteville)

1.5 References

1. World Health Organization, "Global report on diabetes," p. 88, 6 April 2016.
2. S. TA, " Diagnosis and classification of diabetes mellitus," *Diabetes care* , vol. 37, p. S51, 2014.
3. W. C. Yip, I. R. Sequeira, L. D. Plank and S. D. Poppitt, "Prevalence of Pre-Diabetes across Ethnicities: A Review of Impaired Fasting Glucose (IFG) and Impaired Glucose Tolerance (IGT) for Classification of Dysglycaemia," *Nutrients*, vol. 9, no. 1273, pp. 1-18, 2017.
4. U. Yogeswaran and S.-M. Chen, "A Review on the Electrochemical Sensors and Biosensors Composed of Nanowires as Sensing Material," *Sensors*, vol. 8, no. 1, pp. 290-313, 2008.
5. L. C. Clark and C. Lyons, "Electrode Systems For Continuous Monitoring In Cardiovascular Surgery," *Annals of the New York Academy of Sciences*, vol. 102, pp. 29-45, 1962.
6. G. Ocvirk, H. Buck, S. H. DuVall, "Electrochemical Glucose Biosensors for Diabetes Care," *Trends in Bioelectroanalysis* , vol. 6, pp. 1-101, 2016.

7. A. J. Bandodkar and J. Wang, "Non-invasive wearable electrochemical sensors: a review," *Trends in Biotechnology*, vol. 32, no. 7, pp. 363-371, 2014.
8. C. Chen *et al*, "Recent advances in electrochemical glucose biosensors:," *RCS Advances*, vol. 3, no. 14, p. 4473–4491, 2013.
9. J. C. Pickup *et al*, "Fluorescence-based glucose sensors," *Biosensors & bioelectronics*, vol. 20, no. 12, pp. 2555-65, 2005.
10. S. Sharma *et al*, "Evaluation of a minimally invasive glucose biosensor for continuous tissue monitoring," *Analytical and Bioanalytical Chemistry*, vol. 408, no. 29, pp. 8427-8435, 2016.
11. A. Kagie *et al*, "Flexible Rolled Thick-Film Miniaturized Flow-Cell for Minimally Invasive Amperometric Sensing," *Electroanalysis*, vol. 20, no. 14, pp. 1610-1614, 2008.
12. M. J. Tierney, J. A. Tamada, R. O. Potts, L. Jovanovic and S. Garg, "Clinical evaluation of the GlucoWatch® biographer: a continual, non-invasive glucose monitor for patients with diabetes," *Biosensors & Bioelectronics*, vol. 16, no. 9-12, p. 621–629, 2001.
13. J. D. Lane, D. M. Krumholz, R. A. Sack and C. Morris, "Tear Glucose Dynamics in Diabetes Mellitus," *Current Eye Research*, vol. 31, pp. 895-901, 2006.
14. J. Kim, "Wearable smart sensor systems integrated on soft contact lenses for wireless ocular diagnostics," *Nature Communications*, vol. 8, p. 14997, 2017.
15. M. S. Talary, F. Dewarrat, D. Huber and A. Caduff, "In vivo life sign application of dielectric spectroscopy and non-invasive glucose monitoring," *Journal of Non-Crystalline Solids*, vol. 353, no. 47-51, pp. 4515-4517, 2007.
16. M. A. Arnold and G. W. Small, "Noninvasive Glucose Sensing," *Analytical Chemistry*, vol. 77, pp. 5429-5439, 2005.
17. A. Seko, F. Oba, A. Kuwabara and I. Tanaka, "Pressure-induced phase transition in ZnO and ZnO-MgO pseudobinary system: A first-principles lattice dynamics study," *Physical Review B*, vol. 72, p. 024107, 2005.
18. C. Wang *et al*, "Enhanced emission intensity of vertical aligned flexible ZnO nanowire/polymer hybridized LED array by piezo-phototronic effect," *Nano Energy*, vol. 14, pp. 364-371, 2015.
19. W. Lin, R. Ma, J. Xue and B. Kang, "RF magnetron sputtered ZnO: Al thin films on glass substrates: a study of damp heat stability on their optical and electrical properties," *Solar Energy Materials and Solar Cells*, vol. 91, no. 20, pp. 1902-1905, 2007.
20. H.-J. Lim, D. Y. Lee and Y.-J. Oh, "Gas sensing properties of ZnO thin films prepared by microcontact printing," *Sensors and Actuators A: Physical*, vol. 125, no. 2, pp. 405-410, 2006.

21. A. Paliwal, A. Sharma, M. Tomar and V. Gupta , "Carbon monoxide (CO) optical gas sensor based on ZnO thin films," *Sensors and Actuators B: Chemical*, vol. 250, pp. 679-685, 2017.
22. C. Zhang, "Enhanced waveguide-type ultraviolet electroluminescence from ZnO/MgZnO core/shell nanorod array light-emitting diodes via coupling with Ag nanoparticles localized surface plasmons," *Nanoscale*, vol. 7, pp. 1073-1080, 2015.
23. K. Byrappa and M. Yoshimura, *Handbook of Hydrothermal Technology, A Technology for Crystal Growth and Material Processing*, New Jersey: Noyes, 2001.
24. J. P. Proot, C. Delerue and G. Allan, "Electronic structure and optical properties of silicon crystallites: Application to porous silicon," *Applied Physics Letters*, vol. 61, no. 16, pp. 1948-1950, 1992.
25. X. Liu, "Black silicon: fabrication methods, properties and solar energy applications," *Energy & Environmental Science*, vol. 7, pp. 3223-3263, 2014.
26. N.-M. Park, C.-J. Choi, T.-Y. Seong and S.-J. Park, "Quantum Confinement in Amorphous Silicon Quantum Dots Embedded in Silicon Nitride," *Physical Review Letters*, vol. 86, no. 7, pp. 1355-1357, 2001.
27. M. Dao , L. T. Chwee and S. Subra, "Mechanics of the human red blood cell deformed by optical tweezers," *Journal of the Mechanics and Physics of Solids*, vol. 51, no. 11, pp. 2259-2280, 2003.
28. M. Diez-Silva, M. Dao, J. Han, C. T. Lim and S. Suresh, "Shape and Biomechanical Characteristics of Human Red Blood Cells in Health and Disease," *MRS bulletin / Materials Research Society*, vol. 35, no. 5, pp. 382-388, 2010.
29. M. C. Stöppler, "eMedicineHealth," [Online]. Available: http://www.emedicinehealth.com/hemoglobin_a1c_hba1c/article_em.htm. [Accessed 1 September 2017].
30. W. P. Nakanga, A. Crampin and M. Nyirenda, "Personal View: Should haemoglobin A1C be used for diagnosis of diabetes mellitus in Malawi?," *Malawi Medical Journal*, vol. 28, no. 1, pp. 28-30, 2016.
31. R. J. Koenig and A. Cerami, "Hemoglobin A1c and diabetes mellitus," *Annual Review of Medicine*, vol. 31, pp. 29-34, 1980.
32. K. P. Peterson, J. G. Pavlovich, R. Little, J. England and C. M. Peterson, "What is hemoglobin A1c? An analysis of glycosylated hemoglobins by electrospray ionization mass spectrometry.," *Clinical Chemistry*, vol. 44, no. 9, pp. 1951-1958, 1998.
33. R. Koenig, C. Peterson, R. Jones, C. Saudek, M. Lehrman and A. Cerami, "Correlation of glucose regulation and hemoglobin A1c in diabetes mellitus," *The New England Journal of Medicine*, vol. 295, no. 8, pp. 417-420, 1976.

34. E. J. Gallagher, D. L. Roith and Z. Bloomgarden, "Review of hemoglobin A1c in the management of diabetes," *Journal of Diabetes*, vol. 1, pp. 9-17, 2009.
35. D. M. Nathan, "Translating the A1C assay into estimated average glucose values," *Diabetes Care*, vol. 31, no. 8, pp. 1473-1478, 2008.
36. National Center for Chronic Disease Prevention and Health Promotion, Division of Diabetes Translation, "The Surprising Truth About Prediabetes," 25 January 2017.
37. M. Eckert, "Max von Laue and the discovery of x-ray diffraction in 1912," *Annalytical Physics*, vol. 524, no. 5, pp. A83-A85, 2012.
38. A. D. Baczewski, L. Shulenburger, M. P. Desjarlais, S. B. Hansen and M. P. Magyar, "X-ray Thomson Scattering in Warm Dense Matter without the Chihara Decomposition," *Physical Review Letters*, vol. 116, no. 11, p. 115004, 2016.
39. T. Bor, "Philips X'Pert 1 X-ray Diffractometer," Mechanical Testing Laboratory, University of Twente, [Online]. Available: https://www.utwente.nl/en/mechlab/spectroscopy_and_diffraction/Philips%20X%27Pert%201%20X-ray%20Diffractometer.whlink/. [Accessed 15 March 2018].
40. "FEI/Philips XL-30 Field Emission ESEM," Center for Electron Microscopy and Analysis (CEMAS), The Ohio State University, [Online]. Available: <https://cemas.osu.edu/feiphilips-xl-30-field-emission-esem>. [Accessed 15 March 2018].
41. "Raman spectroscopy – Basic principle, instrumentation and selected applications for the characterization of drugs of abuse," *Egyptian Journal of Forensic Sciences*, vol. 6, no. 3, p. 209-215, 2016.

CHAPTER 2. ELECTROCHEMICAL GLUCOSE SENSOR BASED ON ZINC OXIDE NANORODS

2.1 Chapter Overview

In this chapter, we use the hydrothermal sol-gel technique to synthesis ZnO nanorods on a glass substrate coated with indium tin oxide (ITO). The as-synthesized nanostructures are then characterized using structural and optical characterization methods like XRD, SEM, absorption spectroscopy and micro-Raman spectroscopy. The ZnO nanorods are then employed to fabricate an electrochemical sensor for glucose detection that is characterized by means of the cyclic voltammetry and the amperometry device characterization techniques. The low temperature, high pressure, cost effective, rapid and simple hydrothermal sol-gel technique is optimized to get high purity, homogeneous, hexagonal shaped ZnO nanorods (as shown in Fig. 2.2 (a)). The current sensitivity, response time, and limit of detection (LOD) of the fabricated sensor under test are compared to previously reported electrochemical sensors.

Fabrication of an Electrochemical Sensor for Glucose Detection using ZnO Nanorods

Sanghamitra Mandal^{1*}, Mohammed Marie² and Omar Manasreh¹

¹ Department of Electrical Engineering, University of Arkansas, Fayetteville, AR 72701, U.S.A.

² Microelectronics Photonics Program, University of Arkansas, Fayetteville, AR 72701, U.S.A.

Abstract

An electrochemical glucose sensor based on ZnO nanorods is fabricated, characterized and tested. The ZnO nanorods are synthesized on indium titanium oxide (ITO) coated glass substrate, using the hydrothermal sol-gel technique. The working principle of the sensor under investigation is based on the electrochemical reaction taking place between cathode and anode, in the presence of an electrolyte. A platinum plate, used as the cathode and Nafion/Glucose

Oxidase/ZnO nanorods/ITO-coated glass substrate used as anode, is immersed in pH 7.40 phosphate buffered saline (PBS) as the electrolyte to test for the presence of glucose. Several amperometric tests are performed on the fabricated sensor to determine the response time, sensitivity and limit of detection (LOD) of the sensor. A fast response time less than 3 s with a high sensitivity of $1.15 \text{ mA cm}^{-2}\text{mM}^{-1}$ and low LOD of 0.089 mM is reported. The glucose sensor is characterized using the cyclic voltammetry method in the range from -0.8 – 0.8 V with a voltage scan rate of 100 mV/s.

Keywords: X-ray diffraction (XRD); sol-gel; nanostructure

2.2 Introduction

Today, health issues caused by diabetes have affected 350 million people in the world, causing high rates of illness and deaths [1]. Glucose is the most important form of sugar in the human blood that acts as the prime source of energy for the human body. Monitoring normal blood glucose level prevents the risks of suffering from the chronic disease diabetes. It is reported that ZnO nanowires are biodegradable and biocompatible in bio fluids [2]. The isoelectric point of ZnO is 9.5 that make nanostructured ZnO materials to easily absorb enzymes in buffer solutions [3]. The stability of ZnO in air is high [4]. The oxide layers naturally formed on zinc do not form a passivating film, which prevents its corrosion [5]. In the recent years, 1D ZnO nanorods are synthesized using the hydrothermal growth technique [6]. In this paper, an enzyme based amperometric electrochemical glucose sensor is reported. In such sensors, high rate of enzyme mobilization with an appropriate transducer material is desired [7]. The working of amperometric sensors are based on the detection of hydrogen peroxide (H_2O_2) during the enzymatic reaction by anodic oxidation [8]. Platinum is one of the most commonly used transducer electrodes used in amperometric sensors [8]. A sensitivity of $1151 \mu\text{A}/\text{cm}^2 \text{mM}$ is

reported for the investigated Nafion/GOx/ZnO nanorods/ITO coated glass substrate electrode. The sensitivity is derived from the linear response slope obtained for a glucose concentration ranging from 0.01 – 1.60 mM. The acquired sensitivity slope is extremely high compared to peer results reported on glucose sensors based on ZnO nanocombs [11], ZnO nanorods arrays [10, 12], ZnO nanotubes [9, 13], ZnO nanowires [14] and ZnO inverse opal [14] (See Appendix: Table 2.1). Also, the LOD varies between 0.001 – 0.070 mM [9, 10-17] as compared to 0.089 mM reported in this paper. In this paper, a response time less than 3 s is reported that is faster considering previous papers reported on enzymatic glucose sensors based on different nanomaterials like titanium sol-gel membrane [15], carbon decorated ZnO nanowires on titanium [16], and nanostructured cerium oxide film [17] (See Appendix: Table 2.1).

2.3 Experiment

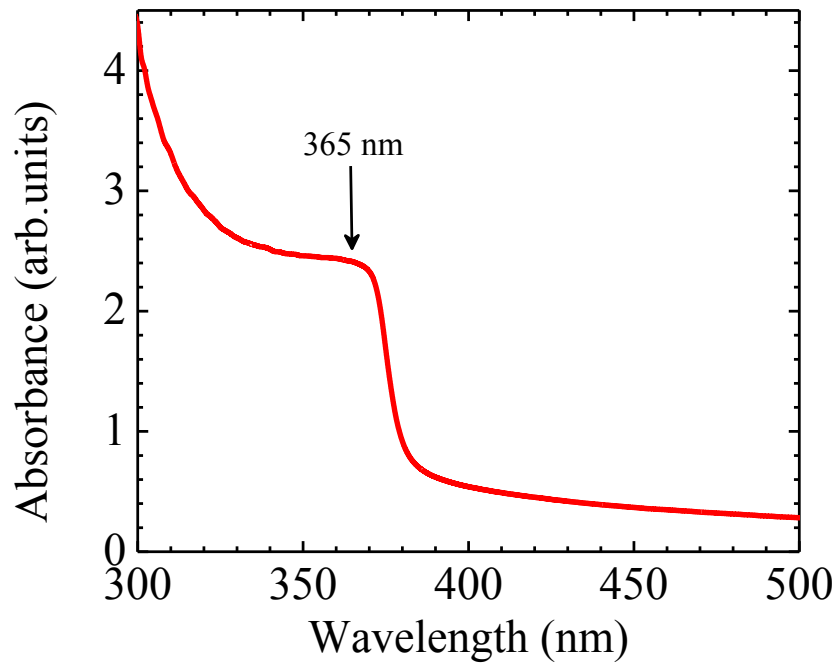
All the chemicals used during the experiment were purchased from VWR International or Sigma-Aldrich without further purification. A 0.50 M ZnO sol-gel is prepared by stirring 1.10 g of zinc acetate in 10 mL of mono-ethanolamine for 1 hour at a temperature of 70 °C. A milky dull solution is formed to which 0.30 mL of ethanolamine is added and stirred for an hour at 70 °C. The ZnO sol-gel is spin-coated on indium titanium oxide (ITO) coated glass substrate to form a thin-film over the substrate surface. A 0.05 M ZnO nanorods growth solution is prepared by stirring 0.30 g of zinc nitrate hexa-hydrate, and 0.14 g of hexamethylenetetramine, respectively in 10 mL of DI water at room temperature for an hour. The ITO substrate coated with thin film is immersed into the growth solution upside down at a temperature of 85 °C for 4 hours. The sample is then, rinsed with DI water and annealed at room temperature for 30 min at a temperature of 110 °C.

The sample with well-aligned hexagonal ZnO nanorods is characterized using absorbance, Raman and scanning electron microscopies, and Gonio mode X-ray diffraction (XRD) using Cary 500 Scan UV-Vis-NIR spectrophotometer, Horiba LabRAM HR Raman spectroscopy, scanning electron microscope, and Philips PW 1830 double system diffractometer, respectively. Sensor fabrication is performed using an enzyme that is prepared by sonicating 40 mg Bovine serum albumin and 20 mg GOx in 0.40 mL phosphate buffered saline (PBS). The polymer nafion (0.20 μ L) is dropped on the sample to stabilize the GOx and prevent enzyme leakage. The sample with Nafion/GOx/ZnO nanorods/ITO-coated glass substrate, and platinum plate are, respectively used as anode and cathode, to measure current response for a constant voltage of 0.80 V by means of the Keithley 2410 source meter. Redox state studies are performed using cyclic voltammetry for a voltage range from -0.80 V – 0.80 V with a voltage sweep rate of 100 mV/s.

2.4 Discussion

The ultraviolet - visible absorbance spectroscopy is measured at room temperature for the hydrothermal ZnO nanorods grown for a wavelength ranging from 200 nm to 1000 nm. A prominent exciton band peak is observed at 365 nm as depicted in Fig. 2. 1 (a). A blue shift is witnessed when compared to the absorbance of bulk ZnO at 374 nm [18]. The particle size of ZnO nanorods with radius 1.1 ± 0.1 nm slightly decreases when compared to the bulk ZnO exciton Bohr's radius ~ 2.34 nm [19]. The band gap expansion and blue shift in the absorbance spectrum occurs due to quantum confinement in the ZnO nanorods [19] synthesized using the sol-gel growth method. Raman spectroscopy is utilized to determine the lattice distortions in ZnO nanorods caused by oxygen vacancies and impurities. The Raman spectrum shown in Fig. 2. 1 (b) has dominant peaks at 332.0, 380.0, 439.7, and 584.0 cm^{-1} . These peaks are called the E_2

low second order Raman mode, A_1 transverse optical mode, non-polar E_2 high optical phonon mode, and the E_1 longitudinal optical mode, respectively. The location of the modes is determined by the crystal orientation, and polarization of the incident and Raman scattered lights [20].



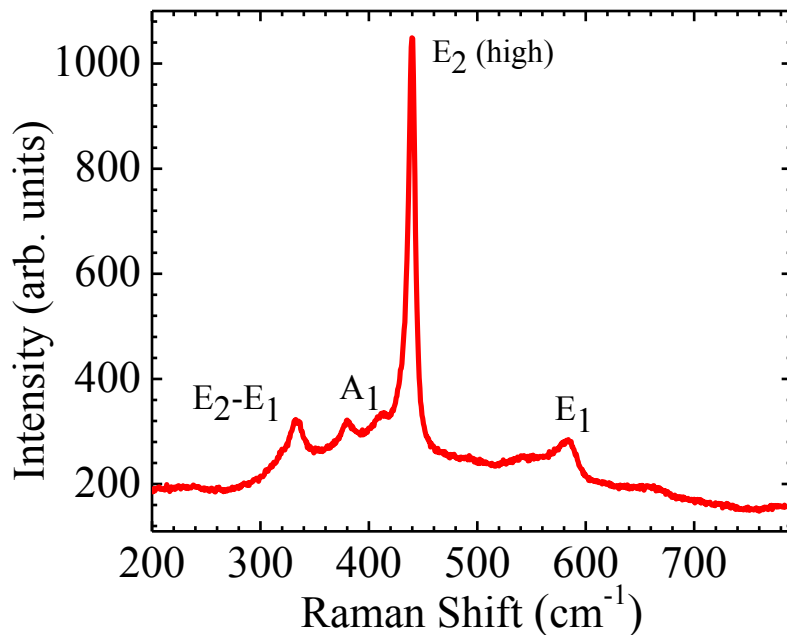


Figure 2. 1 (a) Absorbance spectrum of hydrothermally grown ZnO nanorods measured at room temperature. **(b)** Micro-Raman spectrum for ZnO nanorods grown on ITO coated glass substrate after hot plate annealing at 120°C.

The top view scanning electron microscopy (SEM) image of the sample substrate with ZnO nanorods is represented in Fig. 2. 2 (a). The nanorods are hexagonal in shape, well-aligned and evenly distributed throughout the surface of the ITO-coated glass substrate. The length and diameter of the ZnO nanorods is $\sim 1.5 \mu\text{m}$ and $\sim 70.0 \text{ nm}$, respectively. The aspect ratio is calculated as 21. Aspect ratio is referred to as the ratio of the average length to the average width of the nanorods. The crystal structure and orientation of the ZnO nanorods are studied using the Gonio-mode XRD pattern as shown in Fig. 2. 2 (b). The most dominant peak appears at 34.36° representing the (002) orientation of the ZnO 2Theta scan XRD pattern. Other peaks at 36.21° , 47.47° , 62.76° , and 72.43° , denote the (101), (102), (103), and (004) orientation XRD peaks of ZnO. The lattice constants calculated using the (002) orientation is $a = 3.011 \text{ \AA}$ and $c =$

5.22 Å, which are in good agreement with the bulk ZnO [21]. The Scherrer's equation given below [22] is used to determine the average crystal size (~ 7.64 Å) for (002) orientation ZnO.

$$\tau = \frac{K \cdot \lambda}{\beta \cdot \cos\theta} \quad (2.4.1)$$

In equation 2.4.1, K, λ , β , and θ are shape factor (0.9), the X-ray wavelength (1.54 Å), FWHM (0.19°), and Bragg's diffraction angle (17.18°), respectively.

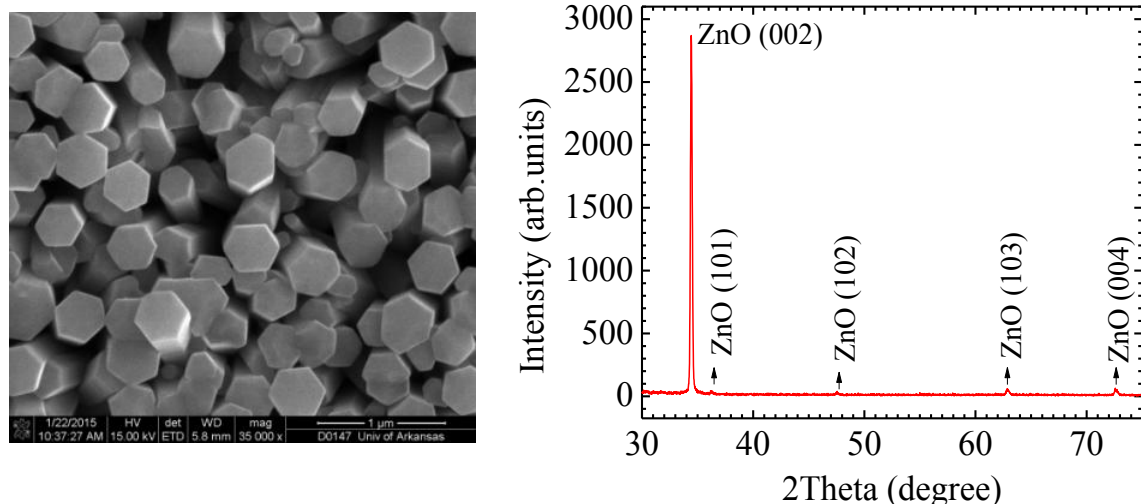


Figure 2. 2 (a) SEM image of ZnO nanorods grown using the sol-gel hydrothermal method on ITO and measured at room temperature. **(b)** Gonio-XRD pattern of ZnO nanorods at room temperature.

The sketch of the working electrode Nafion/GOx/ZnO nanorods/ITO-coated glass substrate is shown in Fig. 2. 3 (a). The substrate with ZnO nanorods are rinsed with PBS to create a hydrophilic surface. 1.0 μL of GOx is dropped onto ZnO nanorods at room temperature and allowed to dry for a couple of hours. 2.0 μL Nafion polymer is dropped onto the substrate with GOx adsorbed ZnO nanorods and dried in air for a couple of hours. Nafion is highly permeable in water and is capable of resisting chemical attack. The ion exchanging properties of nafion creates a biocompatible layer for the enzymes and stabilizes GOx. Figure 2. 3 (b) illustrates the schematic for the glucose sensing electrochemical experiment setup. The working

electrode Nafion/GOx/ZnO nanorods/ITO acts as the anode, and a platinum plate as the cathode that are immersed into the pH 7.40 electrolyte PBS. A potential of 0.80 V is applied across the two electrodes to record the current responses of the sensor.

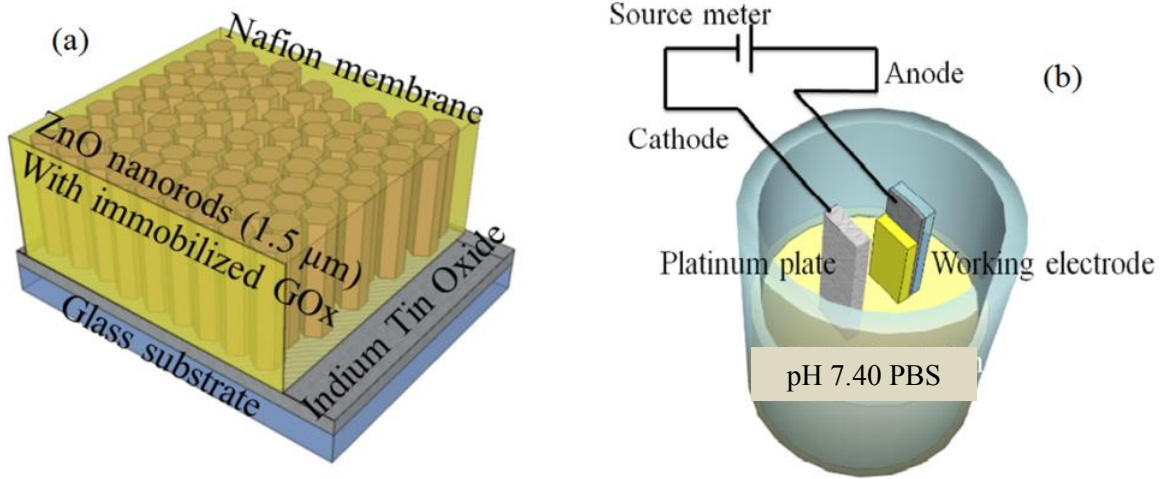
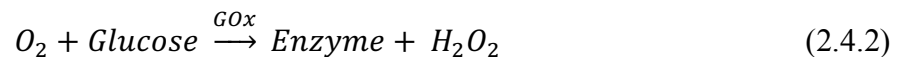


Figure 2. 3 (a) Nafion/GOx/ZnO nanorods/ITO electrode. **(b)** Schematic illustration of the electrochemical test cell with anode and cathode immersed in PBS.

The current response for different concentrations of glucose in PBS is recorded to obtain the calibration curve shown in Fig. 2. 4 (a). The calibration curve is achieved utilizing the steady-state amperometric response for increasing glucose concentrations, added to the pH 7.40 PBS inside the test cell. Steady-state amperometric response refers to the current versus time response. The error bars represent 4% data variability or the standard error for 10 consecutive amperometric responses. During the phenomenon of electrolysis inside the test cell at 0.80 V, glucose gets oxidized by GOx to produce an enzyme that is given by the equation 2.4.2.



Reaction of this enzyme with oxygen produces H₂O₂. Reduction of H₂O₂ chemically occurs according to equation 2.4.3.



The electrons given out into the electrolyte during the electrochemical reaction gives the sensor sensitivity. Based on the amperometric measurements, response time of the sensor is calculated to be ≤ 3.0 s, which is faster than the sensors reported earlier with an aspect ratio of 30 [10]. The slope and the intercept of the curve in Fig. 2. 4 (a) exhibits a sensitivity of 1.15 mA/cm² mM, for a linear range of increasing glucose concentration ranging from 0.01 – 1.60 mM, measured at a fixed potential of 0.80 V. The sensitivity achieved is high compared to peer reviewed results reported on glucose sensors based on ZnO nanorods arrays [10, 12]. Limit of detection (LOD) is given by equation 2.4.3 and is defined as the minimum amount of glucose analyte concentration in PBS that is distinguished from zero [23].

$$LOD = \frac{3 \times \text{Standard Error}}{\text{Slope}} \quad (2.4.4)$$

In equation 2.4.3, the y-intercept of the linear fit is considered as the standard error. The LOD for the sensor is calculated as 0.089 mM. The normal glucose level in humans, fall in between the range from 3.5 – 6.1 mM, whereas in case of a diabetic person it could be as high as 18.00 mM [14]. This clinical glucose range justifies the detection range and achieved LOD reported in this paper. The cyclic voltammogram presented in Fig. 2. 4 (b) has a reduction peak at -0.45 V indicating reduction of H₂O₂, and an oxidation peak at 0.45 V demonstrating the oxidation of glucose. It can be inferred that with the increase in the glucose concentration successively added to PBS leads to an increase in the rate of glucose oxidation by enzyme GOx that are seen as the redox peaks in the voltammogram (Fig. 2. 4 (b)).

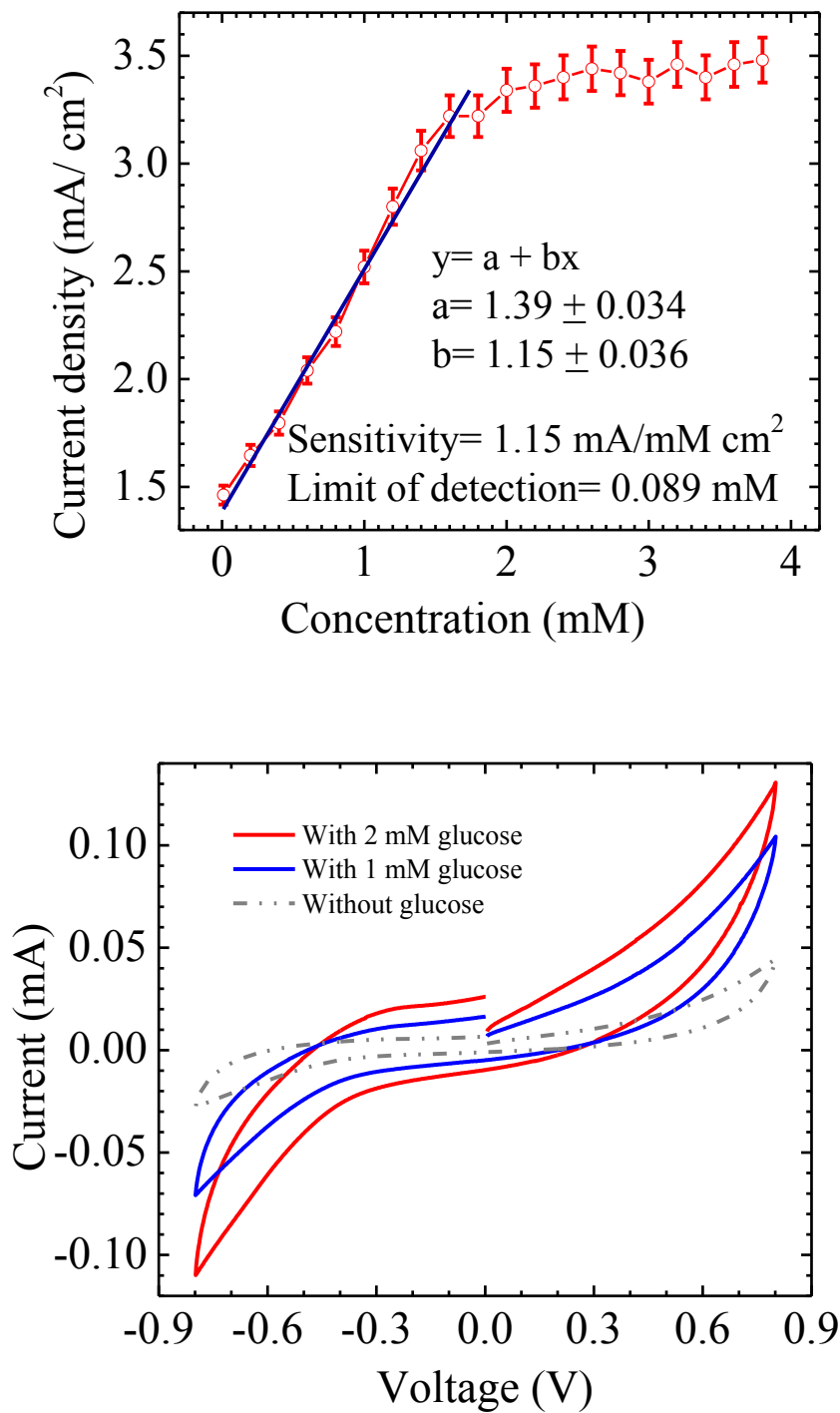


Figure 2. 4 (a) Calibration curve plotted using the amperometric response measured at a potential of 0.80 V, for glucose concentration ranging from 0.01 – 20.0 mM, **(b)** Cyclic-voltammogram of electrochemical glucose sensor for a potential ranging from -0.80 V – 0.80 V with a sweep rate of 100 mV/sec.

2.5 Conclusion

An enzymatic electrochemical glucose sensor based on the phenomenon of GOx adsorption by hydrothermally grown ZnO nanorods is reported. The high isoelectric point of ZnO aids in easy absorption of enzymes, whereas its stability in air, and biocompatibility creates an atmosphere for retaining enzyme activity. A simple and low-temperature method known as the hydrothermal sol-gel technique is used to synthesize ZnO nanorods with high aspect ratio. The immobilization efficiency of GOx being absorbed by the ZnO nanorods depends upon the aspect ratio of the nanorods. The hydrothermal synthesis growth conditions control the surface morphology and distribution of the ZnO nanorods, grown on the desired substrate. High aspect ratio ZnO nanorods are utilized to improve the electrical contact for the redox reaction taking place between GOx and platinum electrode along with the use of biocompatible nafion membrane. Well aligned ZnO nanorods with high aspect ratio contribute to the best performance in terms of sensitivity for glucose detection. The low-cost fabrication method, with the achieved high sensor sensitivity, encourages further investment and research towards commercialization of such electrochemical glucose sensors.

Table 2. 1 Performance parameters of peer reported electrochemical glucose sensors.

Working electrode material	Sensitivity ($\mu\text{A}/\text{cm}^2\text{mM}$)	Response time (s)	LOD (mM)	Linear range (mM)	Reference
ZnO nanotubes/Au	21.7	3	0.001	0.05 – 12	9
ZnO nanorods/Si/Ag	106.6	< 2	0.001	0.01 – 17.00	10
ZnO nanocomb/Au	15.33	< 10	0.02	0.02 – 4.5	11
ZnO nanorods/Au	23.1	< 5	0.01	0.01 – 3.45	12
ZnO nanotubes	30.85	< 6	0.01	0.01 – 4.2	13
ZnO inverse opal	22.5	–	–	0.01 – 18	14
ZnO nanowires	24.56	–	–	0.01 – 7	14
TiO ₂ sol-gel film	7.2	< 6	0.07	0.07 – 15	15
C-ZnO nanowires/Ti	35.3	~ 5	0.001	0.01 – 1.6	16
CeO ₂ /Au	0.0029	< 5	0.012	2.8 – 22.2	17
ZnO nanorods/ITO	1151	< 3.0	0.089	0.01 – 1.6	This work

Appendix

The comparison of the performance parameters of other peer reported glucose sensors based on other nanomaterials grown on different substrates has been presented in Table 2.1.

2.6 Chapter Summary

The employment of high aspect ratio, well aligned ZnO nanorods in the sensor working electrode plays an important role in increasing the active sensing area. This allows the ZnO nanorods to adsorb higher amounts of enzyme GOx that enhances the oxidation-reduction reaction inside the electrochemical cell. In other words, higher the amount of enzyme GOx adsorbed by the ZnO nanorods, longer will the electrochemical redox reaction last. The rate of oxidation of glucose is be higher and longer, leading to higher amount of H₂O₂ formed inside the electrochemical cell. As a result, more amount of H₂O₂ gets reduced, leading to the generation of higher number of electrons. This then leads to high current sensitivity detection of the sensor. The enzyme GOx primarily catalyzes the oxidation of glucose and causes the formation of H₂O₂. In Table 2.1, we compare the current sensitivity, response time and LOD of our electrochemical sensor with other published works. In this work, the main reason towards superior sensor performance parameters is the high quality ZnO nanorods fabricated using our optimized hydrothermal sol-gel synthesis technique.

2.7 References

1. World Health Organization, www.who.int/diabetes/wdd_2015/en/ (last seen on 11/16/2015).
2. Zhou, J., Xu, N. S. and Wang, Z. L, Dissolving Behavior and Stability of ZnO Wires in Biofluids: A Study on Biodegradability and Biocompatibility of ZnO Nanostructures, *Adv. Mater.* 18 (2006) 2432-2435.
3. Zhao, Z., Lei, W., Zhang, X., Wang, B., & Jiang, H. ZnO-Based Amperometric Enzyme Biosensors. *Sensors* (Basel, Switzerland), 10(2), (2010) 1216-1231.

4. Mein Jin Tan, Shu Zhong, Jun Li, Zhikuan Chen, and Wei Chen, Air-Stable Efficient Inverted Polymer Solar Cells Using Solution-Processed Nanocrystalline ZnO Interfacial Layer, *ACS Applied Materials & Interfaces*, 5 (11), (2013) 4696-4701.
5. Juan Zuow and Andreas Erbe, Optical and electronic properties of native zinc oxide films on polycrystalline Zn, *Phys. Chem. Chem. Phys.* 12 (2010), 11467-11476.
6. Ibupoto, Z.H.; Khun, K.; Eriksson, M.; AlSalhi, M.; Atif, M.; Ansari, A.; Willander, M. Hydrothermal Growth of Vertically Aligned ZnO Nanorods Using a Biocomposite Seed layer of ZnO Nanoparticles. *Materials*, 6, (2013) 3584-3597.
7. W. Putzbach and N. J. Ronkainen, Immobilization Techniques in the Fabrication of Nanomaterial-Based Electrochemical Biosensors: A Review, *Sensors* 13, (2013) 4811-4840.
8. D. Wilke, H. Müller and N. Kolytsheva, Activated platinum electrodes as transducer for a glucose sensor using glucose oxidase in a photopolymer membrane, *Fresenius J Anal Chem*, 357, (1997), 534–538.
9. Tao Kong, Yang Chen, Yiping Ye, Kun Zhang, Zhenxing Wang, and Xiaoping Wang, An amperometric glucose biosensor based on the immobilization of glucose oxidase on the ZnO nanotubes, *Sensors and Actuators B*, 138, (2009) 344-350.
10. R. Ahmad, N. Tripathy, J. H. Kim and Y. Hahn, Highly selective wide linear-range detecting glucose biosensors based on aspect-ratio controlled ZnO nanorods directly grown on electrodes, *Sensors & Actuators B. Chemical*, 174, (2012) 195-201.
11. J. X. Wang, X.W. Sun, A. Wei, Y. Lei, X. P. Cai, C. M. Li and Z. L. Dong, Zinc oxide nanocomb biosensor for glucose detection, *Applied Physics Letters*, 88, (2006) 233106.
12. A. Wei, X. W. Sun, J. X. Wang, Y. Lei, X. P. Cai, C. M. Li, Z. L. Dong and W. Huang, Enzymatic glucose biosensor based on ZnO nanorod array grown by hydrothermal decomposition, *Applied Physics Letters*, 89, (2006) 123902.
13. Kun Yang, Guang-Wei She, Hui Wang, Xue-Mei Ou, Xiao-Hong Zhang, Chun-Sing Lee and Shuit-Tong Lee, ZnO Nanotube Arrays as Biosensors for Glucose, *The Journal of Physical Chemistry C*, 113, (2009) 20169-20172.
14. Xueqiu You, James H. Pikul, William P. King and James J. Pak., Zinc oxide inverse opal enzymatic biosensor, *Appl. Phys. Lett.*, 102, (2013) 253103.
15. Jiahong Yu, Songqin Liu and Huangxian Ju, Glucose sensor for flow injection analysis of serum glucose based on immobilization of glucose oxidase in titania sol-gel membrane, *Biosensors and Bioelectronics*, 19, (2003) 401-409.
16. J. Liu, C. Guo, C. M. Li, Y. Li, Q. Chi, X. Huang, L. Liao, and T. Yu, Carbon-decorated ZnO nanowire array: A novel platform for direct electrochemistry of enzymes and biosensing applications, *Electrochemistry Communications*, 11, (2009) 202-205.

17. A. A. Ansari, P. R. Solanki and B. D. Malhotra, Sol-gel derived nanostructured cerium oxide film for glucose sensor, *Applied Physics Letters*, 92, (2008) 263901.
18. L. Guo, S. Yang, C. Yang, P. Yu, J. Wang, W. Ge and G. K. L. Wong, Highly monodisperse polymer-capped ZnO nanoparticles, Preparation and optical properties, *Appl. Phys. Lett.*, 76, (2000) 2901-2903.
19. Gu, Y. and Kuskovsky, Igor L. and Yin, M. and O'Brien, S. and Neumark, G. F., Quantum confinement in ZnO nanorods, *Applied Physics Letters*, 85, (2004) 3833-3835.
20. An-Jen Cheng, Yonhua Tzeng, Hui Xu, Siddharth Alur, Yaqi Wang, Minseo Park, Tsung-hsueh Wu, Curtis Shannon, Dong-Joo Kim and Dake Wang, Raman analysis of longitudinal optical phonon-plasmon coupled modes of aligned ZnO nanorods, *Journal of applied physics* 105 (2009) 073104.
21. Julia W. P. Hsu, Zhengrong R. Tian, Neil C. Simmons, Carolyn M. Matzke, James A. Voigt, and, Jun Liu, Directed Spatial Organization of Zinc Oxide Nanorods, *Nano Letters*, 5 (1), (2005) 83-86.
22. A. Monshi, M. F. Foroughi, and M. R. Monshi, Modified Scherrer Equation to Estimate More Accurately Nano-Crystallite Size Using XRD, *World Journal of Nanoscience and Engineering* 2 (2012) 154-160.
23. Armbruster, David A, and Terry Pry, Limit of Blank, Limit of Detection and Limit of Quantitation, *The Clinical Biochemist Reviews* 29. Suppl 1, (2008) S49-S52.
24. Shrivastava A and Gupta VB, Methods for the determination of limit of detection and limit of quantitation of the analytical methods, *Chron Young Sci.* 2 (2011) 21-25.

CHAPTER 3. ELECTROCHEMICAL GLUCOSE SENSOR BASED ON SILICON NANOWIRES

3.1 Chapter Overview

In this chapter, we fabricate and characterize an electrochemical sensor for glucose detection using silicon (Si) nanowires. The Si nanowires are fabricated from p-type Si wafer by means of the metal assisted chemical etching (MACE) technique as described in this chapter. The MACE is a simple, cost-effective chemical wet etching method that allows control over the morphology of the nanostructures fabrication. In this etching process, silver ions deposit on the surface of the Si wafer when immersed in an etching solution low ratio of HF/AgNO₃. Under optimized etching time and temperature, the silver metal ions slowly sink into the Si wafer forming porous structures. The Si nanowires are then characterized using SEM, absorption spectroscopy and micro-Raman spectroscopy. The Si wafer sample with the optimized nanowires are then utilized in the fabrication of the working electrode for the electrochemical glucose sensor. The concept of gold nanoelectrode ensembles were used to enhance the sensor sensitivity.

Fabrication of Nanoelectrode Ensembles using Silicon Nanowires in an Electrochemical Glucose Sensor

Sanghamitra Mandal^{1*}, Mohammed Marie² and Omar Manasreh¹

¹ Department of Electrical Engineering, University of Arkansas, Fayetteville, AR 72701, U.S.A.

² Microelectronics Photonics Program, University of Arkansas, Fayetteville, AR 72701, U.S.A.

Abstract

Gold (Au) nanoelectrode ensembles (NEEs) were investigated after the synthesis of silicon nanowires using the metal assisted chemical etching technique. Structural and non-

destructive optical characterization of silicon nanowires are carried out to determine its morphology and crystallinity. The cyclic voltammetry technique is used to determine the oxidation-reduction potentials of the sensor at different voltage scan rates of 100, 200, and 300 mV/s. Amperometric measurement at a fixed oxidation potential of 0.60 V is performed to measure the sensitivity, response time, and LOD of the sensor. The presence of Au NEEs improve the signal to noise ratio of the sensor. Therefore, the sensor exhibits a high sensitivity of 0.40 mA/mM cm² with a response time of 1.0 s, and a limit of detection 0.077 mM.

Keywords: Electrochemical sensor; silicon nanowires; nanotechnology; metal assisted chemical etching; nanoelectrode

3.2 Introduction

Silicon (Si) is the most commonly used semiconducting material in the nanotechnology industry. Semiconductor Si has replaced other semiconductors like germanium due its abundance on earth's crust, wide energy band-gap, chemical stability, thermal stability, and easy fabrication of passivation layer. Likewise, Si nanowires demonstrate unique morphological, electrical, optical, and thermal characteristics that have led to research advancements and commercialization of Si nanowires-based devices [1]. The properties of the Si nanowires depend on its fabrication technique [2]. The performance of a sensor depends upon the physical and chemical properties of the material used in its fabrication [3]. Electrochemical sensors for glucose detection has emerged as a major research interest area in the past decade due to the rising number of people affected by the metabolic disorder known as Diabetes.

In this paper, we report the fabrication and characterization of an electrochemical glucose sensor based on Si nanowires. Metal assisted chemical etching (MACE) technique is used to synthesize Si nanowires. Optical and structural characterization of the as-synthesized Si

nanowires is performed using the absorbance spectroscopy, micro-Raman spectroscopy, and scanning electron microscopy (SEM). The characterization of the glucose sensor is carried out using the cyclic voltammetry technique and the amperometric tests. It is inferred that the existence of Au NEEs reduce the signal to noise ratio thereby enhancing the current response of the sensor under investigation.

3.3 Sensor Design and Fabrication

3.3.1 Silicon Nanowires Synthesis

The Si nanowires are synthesized using the MACE technique that is a directional wet etching technique, where silver is deposited on the surface of the Si wafer. This etching procedure is used because there is no definite requirement on the morphology of the resultant etched nanostructures. The Si wafer with (1 0 0) orientation allow etching along the $\langle 1\ 0\ 0 \rangle$ direction using a low HF/AgNO₃ ratio [4]. In this technique, silver as the cathode catalyzes the Si atoms to form a silicon di-oxide layer on the sample surface. This is possible because the electronegativity of silver (9.3) is higher than Si (9.0). Thereafter, the HF molecules vertically etch the silicon di-oxide film to form Si nanowires. The depth of the etched nanostructures depends on the concentration of the etching solution and the etch time.

Samples with a dimension of 1 cm x 1 cm are cut from a 4" p-type Si wafer, single side polished, with (1 0 0) orientation, 0.5 mm thick, and doped with dopant boron. The 1 cm² Si substrate samples are cleaned ultrasonically with trichloroethane, acetone, ethanol, and DI water, respectively for 10 mins in each solution. The passive oxide layer of silicon di-oxide formed on the Si is removed by immersing the samples into a 1:10 ratio solution of hydrofluoric acid (HF) and DI water for 60 s. Each sample is then immersed in an etching solution of 30.0 mM silver nitrate (AgNO₃) and 4.60 M solution of HF, for 1200 s at a temperature of 40°C. The sample is

then immersed into nitric acid (HNO₃) for another 1200 s to remove silver atoms from the surface of Si substrate. The sample with Si nanowires is then cleaned using DI water and dried using nitrogen gas.

3.3.2 Sensor Fabrication and Characterization

The Angstrom Nexdep Electron Beam Evaporator is used to deposit 50 nm of highly pure Au film over the chemically etched Si nanowires. During the process, Au NEEs are naturally formed in between Si nanowires in the substrate surface as shown in Fig. 3. 1 (b). The NEEs are made of many small ultra-microelectrodes confined in a small space. These NEEs are useful tools for testing electrochemical sensors that demonstrate LOD values two or three orders lower than the regular electrodes [5] [6].

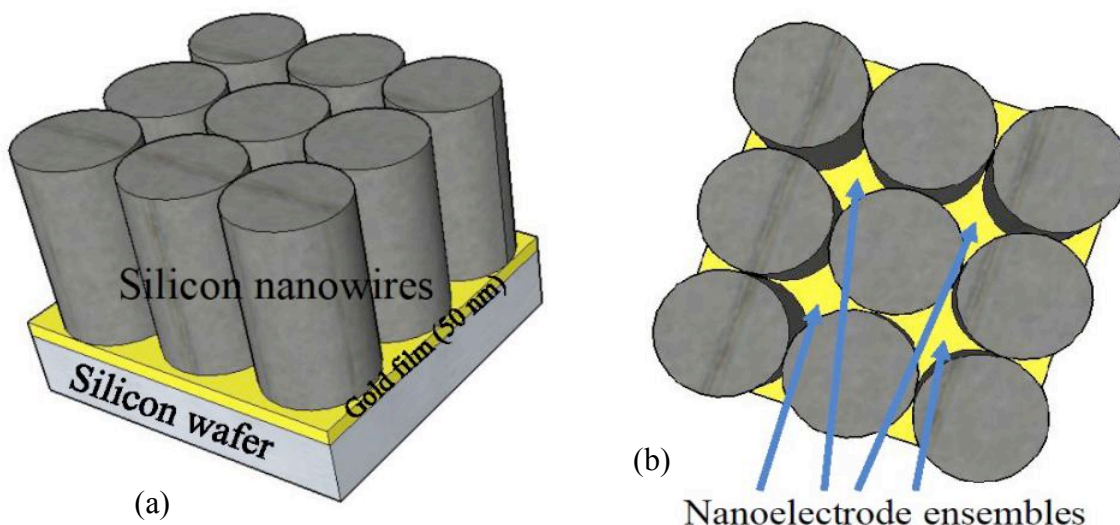


Figure 3. 1 Schematic showing (a) Si nanowires on Si wafer with 50 nm coating of Au (b) Au NEEs in between Si nanowires.

The most common enzyme used for the detection of glucose in enzymatic sensors is GOx. The Si/Au/Si nanowires sample is modified by drop casting 1.0 μ L of enzyme GOx on the substrate surface. The sample is allowed to dry in atmosphere for 3 hrs. Enzyme GOx is prepared by sonicating 40.0 mg bovine serum albumin and 20.0 mg GOx, in 0.40 mL of PBS for

60 mins. Bovine serum albumin is a protein substitute used to stabilize GOx and prevent the adhesion of GOx on the Au/glass substrate surface. Around 2.0 μL of Nafion is drop casted over the substrate once the GOx dries. The sample is allowed to dry in atmosphere for 120 mins.

3.4 Results and Discussion

3.4.1 Structural and Optical Characterization of Si nanowires

The structural characterization of Si nanowires at room temperature is performed using the FEI XL-30 Environmental Scanning Electron Microscope. The general morphology of the Si nanowires synthesized using the MACE technique is depicted by the scanning electron microscopy (SEM) image (top view) in Fig. 3. 2 inset. The Si nanowires with an approximate length of 1.0 μm and diameter of 50 nm are witnessed. The properties of the nanowires are dependent on its diameter [7]. Fig. 3. 2 exhibits the absorbance spectrum of bare Si and Si nanowires at room temperature. Cary 500 Scan UV-Vis-NIR spectrophotometer is used to measure the absorbance of the sample for a wavelength ranging from 500 – 1500 nm. According to literature [2], bare crystalline Si has a band gap of 1.1 eV. This is exhibited by a wavelength of 1126 nm. Also, the absorbance shoulder of Si nanowires is observed at a wavelength of 1094 nm, demonstrating a blue shift in the optical absorption of Si. The shift of 32 nm justifies the phenomenon of quantum confinement demonstrating bandgap expansion and an increase in bandgap energy.

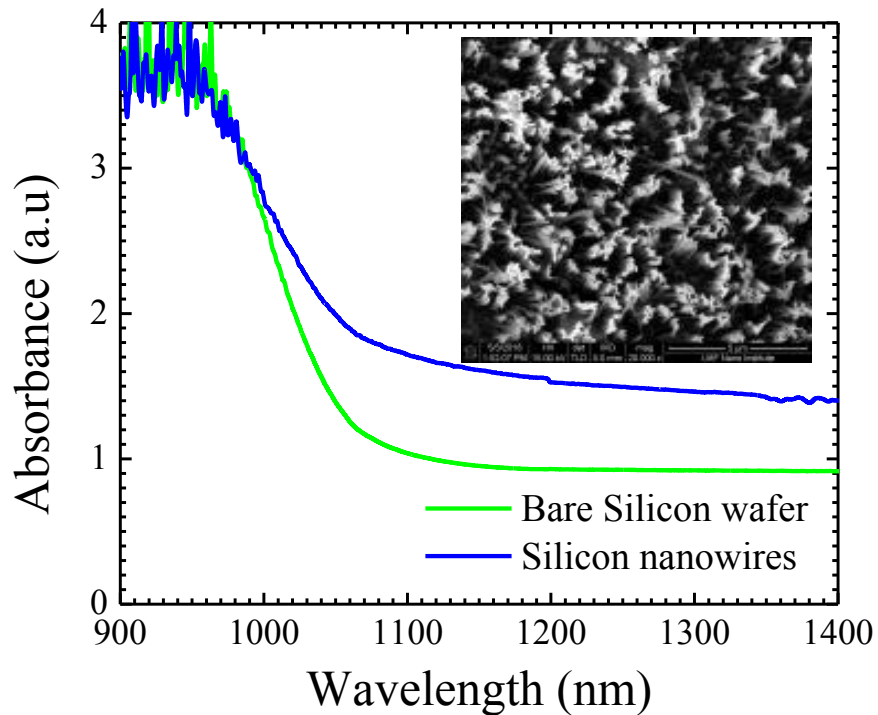


Figure 3. 2 Absorbance spectrum of bare Si and Si nanowires. **Inset:** SEM image illustrating the top view of Si nanowires synthesized using MACE.

The micro-Raman spectrum for bare Si wafer (1 0 0) and Si nanowires is presented in Fig. 3. 3. Horiba LabRAM HR Raman spectroscopy is used to investigate micro-Raman spectrum of the sample in the range from 300 – 1000 cm^{-1} . The Raman peak of bare Si wafer (black) observed at 538.0 cm^{-1} is in agreement with the already published work [8]. The first order optical phonon modes for the Si nanowires with a diameter of 50 nm (red) is observed at 523.00 cm^{-1} . The narrow spectral width and high intensity of the Si nanowires micro-Raman peak indicate high crystal quality of the nanowires.

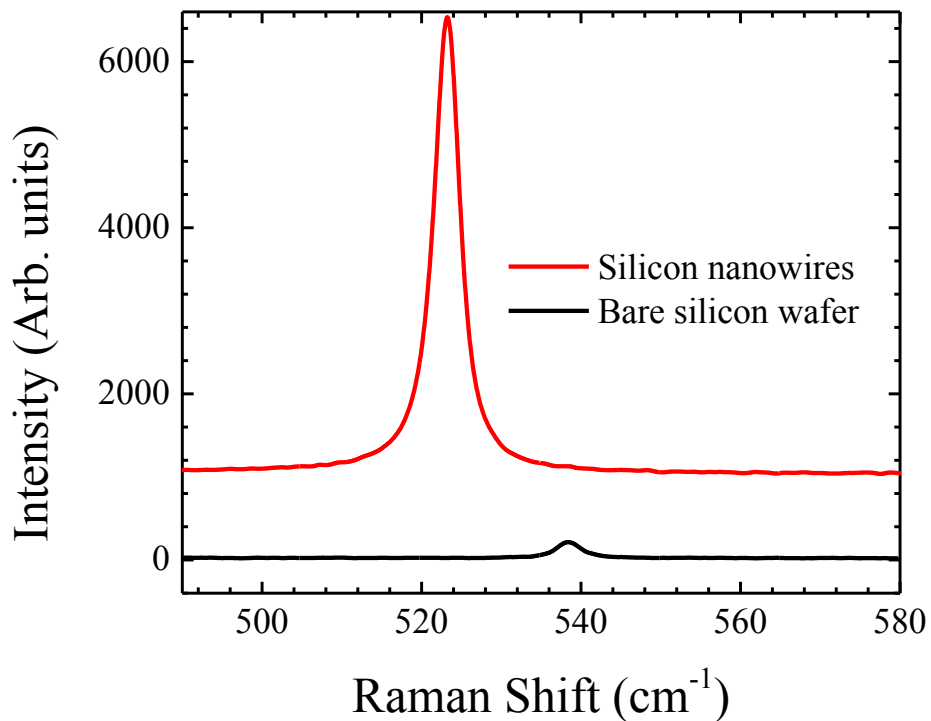


Figure 3. 3 Micro-Raman spectrum of bare Si wafer and Si nanowires measured at room temperature.

3.3.2 Electrochemical Characterization and Testing of the Sensor

The occurrence of NEEs due to Au deposition in between the Si nanowires plays a very important role in reducing the signal to noise ratio when compared to microelectrodes. The 1.0 μm tall Si nanowires increase the electrode surface area, and reduce the electrode resistance, thereby demonstrating higher current sensitivity. Gamry Reference 600 potentiostat is utilized to execute cyclic voltammetric tests on the sensor under investigation at different voltage scan rates of 100, 200, and 300 mV/s as displayed in Fig. 3. 4. The hysteresis characteristic of the cyclic voltammograms describes the electron transfer mechanism between the anode and the cathode inside the electrochemical cell. A shoulder at +0.60 V due to the anodic oxidation current and at -0.35 V due to the cathodic reduction current is observed. These shoulders represent the redox

(oxidation-reduction) reaction taking place inside the test cell during the electrochemical reaction. The anodic oxidation potential of 0.60 V is henceforth used as the applied potential during the amperometric tests. Oxidation and reduction shoulders are observed at all voltage scan rates in the presence of 2.0 mM glucose. These shoulders do not appear when samples are tested in the absence of glucose thereby justifying the sensor glucose sensitivity. A linear relationship between current and voltage scan rates is noticed. Faster scan rate (300 mV/s) show higher current and more prominent shoulder, while slower scan rate (100 mV/s) provide sufficient time for glucose to reduce in the presence of catalyst GOx, which generate H_2O_2 .

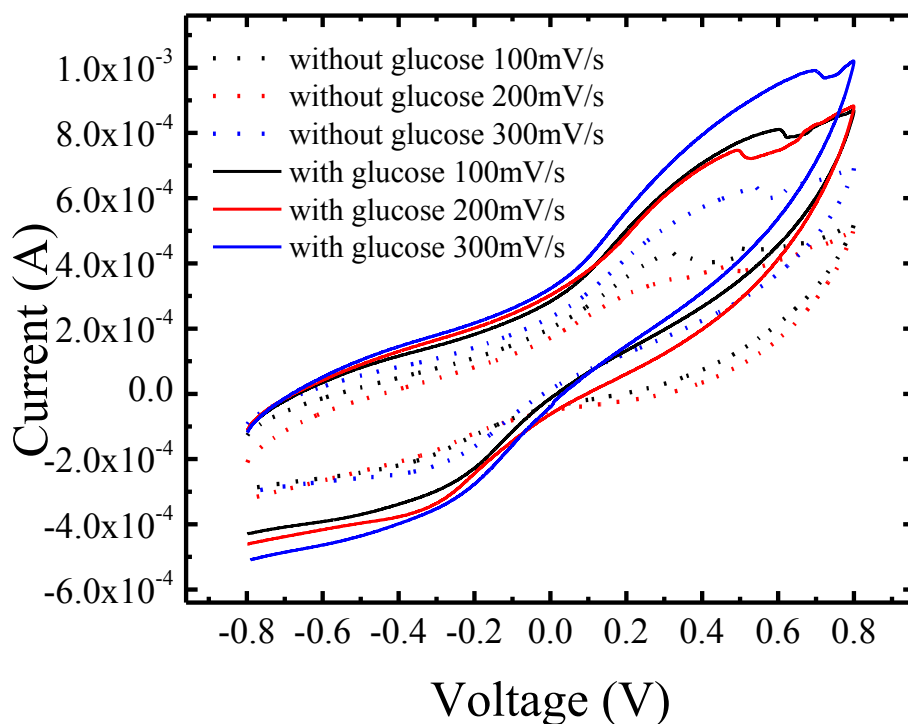


Figure 3. 4 Cyclic voltammograms obtained in the presence and absence (dotted line) of glucose at a sweep rate of 100, 200, and 300 mV/s.

The sensor under investigation is tested using the two-electrode system, where platinum (cathode) is the counter electrode, and Si/Au/Si nanowires/GOx/nafion (anode) is the working

electrode. Keithley 2410 source meter is used to test the sensor under a constant applied voltage of 0.80 V. The current response of the sensor is examined to determine its sensitivity and response time. The sensor is tested inside a closed beaker containing 7.40 pH PBS. The glucose concentration is increased step wise (0.50 mM) with time (10 s) and the corresponding current is noted. This current response versus time is called the amperometric response of the sensor. The amperometric measurements presented in inset of Fig. 3. 5 are current versus time response of the sensor. A response time of 1 s is observed from stepped curve (blue) in inset. The linear calibration curve (red) shown in Fig. 3. 5 is used to calculate sensor sensitivity and LOD using values of slope and intercept obtained. The LOD is calculated to be 0.77 mM, using the equation 3.4.1 [9].

$$\text{LOD} = \frac{3 \cdot \text{Standard Error}}{\text{Slope}} \quad (3.4.1)$$

In equation 3.4.1, the value 3 is the signal to noise ratio [10], and the standard error is the error of the y-intercept in the linear fit.

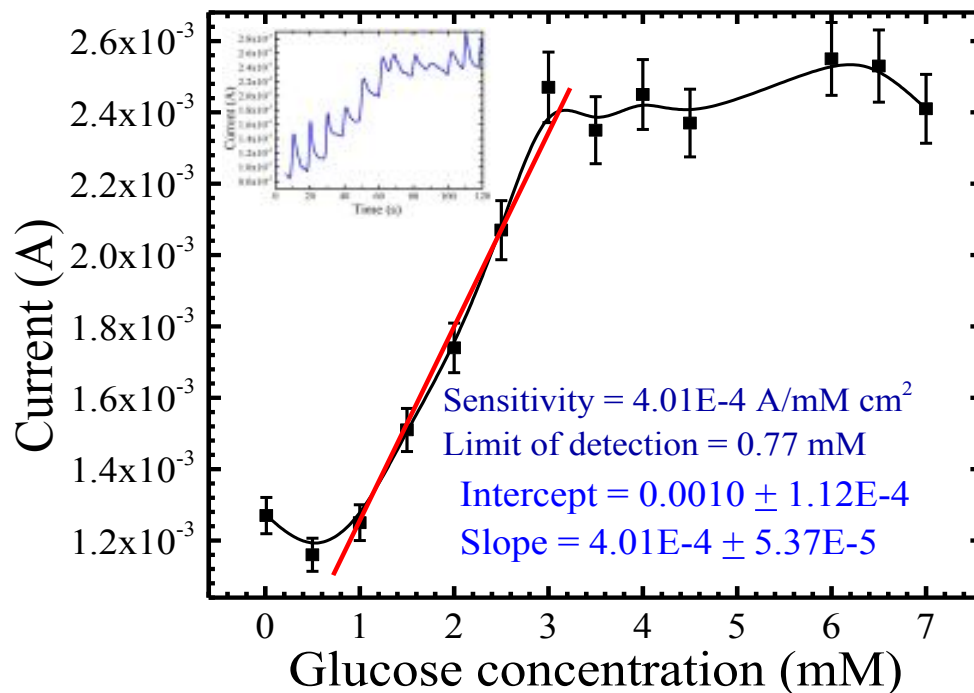


Figure 3. 5 Calibration curve derived from the amperometric measurements performed for a glucose concentration ranging from 0.01 – 7.0 mM. Inset: Steady state amperometric measurements at a constant potential of 0.60 V, for successive addition of 0.50 mM glucose.

3.5 Conclusion

An electrochemical glucose sensor is fabricated and characterized by synthesizing Si nanowires using MACE technique. The as-grown Si nanowires show a blue shift in the absorbance spectrum indicating a bandgap expansion due to the phenomenon of quantum confinement. The deposition of Au on the nanowires leads to the formation of Au NEEs. The NEEs reduce signal to noise ratio and increase current sensitivity of the sensor. Such NEE arrays act as individual sensors by increasing the overall sensor active surface area. The electrochemical sensor under investigation demonstrates high current response, faster response time and low LOD. Considering the increasing demands of nanoscale technology in biomedical engineering, the concept of NEE arrays is promising and demands further research.

3.6 Chapter Summary

The working electrode of the electrochemical glucose sensor fabricated using MACE synthesized Si nanowires, are further modified by depositing Au on the substrate. The e-beam evaporator is used to deposit 10 nm of titanium followed by 50 nm of Au on the Si substrate with as-synthesized Si nanowires. This leads to the formation of Au NEEs that act as individual islands of metal Au. Thereby, there is an increase in the transfer of electrons inside the electrochemical cell during the electrochemical redox reactions. It is observed that the concept of employing Au NEEs lead to an enhanced sensor sensitivity and faster response time of the sensor. However, the sensor sensitivity is an order lower than that observed in the electrochemical glucose sensor based on ZnO nanorods discussed in the previous chapter no. 2. Therefore, we employ the concept of Au NEEs to fabricate ZnO nanorods based electrochemical glucose sensor in the following chapter.

3.7 References

1. Kui-Qing Peng, Xin Wang, Li Li, Ya Hu, Shuit-Tong Lee, "Silicon nanowires for advanced energy conversion and storage", *Nano Today*, Vol. 8, Issue 1, Feb. 2013, pp. 75-97.
2. Schmidt, V., Wittemann, J. V., Senz, S. and Gösele, U., "Silicon Nanowires: A Review on Aspects of their Growth and their Electrical Properties", *Adv. Mater.*, Vol. 21, Jul. 2009, pp. 2681–2702.
3. W. Qu, "Effect of electrode materials on the sensitive properties of the thick-film ceramic humidity sensor," *Solid State Ionics*, vol. 83, no. 3–4, Feb. 1996, pp. 257-262.
4. Li L, Liu Y, Zhao X, Lin Z, and Wong CP, "Uniform vertical trench etching on silicon with high aspect ratio by metal-assisted chemical etching using nanoporous catalysts", *ACS applied materials & interfaces*, Vol. 6, Nov. 2013, pp. 575–584.
5. S. Pozzi Mucelli, M. Zamuner, M. Tormen, G. Stanta, P. Ugo, "Nanoelectrode ensembles as recognition platform for electrochemical immunosensors", *Biosensors and Bioelectronics*, Vol. 23, Issue 12, Jul. 2008, pp. 1900-1903.
6. B. Brunetti, P. Ugo, L.M. Moretto, C.R. Martin, "Electrochemistry of phenothiazine and methylviologen biosensor electron-transfer mediators at nanoelectrode ensembles", *J. Electroanal. Chem.*, Vol. 491, Apr. 2000, pp. 166–174.

7. Holmes JD, Johnston KP, Doty RC, Korgel BA, "Control of thickness and orientation of solution-grown silicon nanowires", *Science*, Vol. 25, Feb. 2000, pp. 1471-1473.
8. Chun Li, Guojia Fang, Su Sheng, Zhiqiang Chen, Jianbo Wang, Shuang Ma, Xingzhong Zhao, "Raman spectroscopy and field electron emission properties of aligned silicon nanowire arrays", *Physical E: Low-dimensional Systems and Nanostructures*, Vol. 30, Dec. 2005, pp. 169-173.
9. Shrivastava A and Gupta VB, "Methods for the determination of limit of detection and limit of quantitation of the analytical methods," *Chron Young Sci.*, vol. 2, no. 1, Apr. 2011, pp. 21-25.
10. Armbruster, D.A. and Pry, T., "Limit of blank, limit of detection and limit of quantitation," *Clin Biochem Rev*, vol. 29, no. Suppl 1, Aug. 2008, pp. S49-52.

CHAPTER 4. ELECTROCHEMICAL GLUCOSE SENSOR BASED ON ZINC OXIDE NANORODS AND GOLD NANO-ELECTRODE ENSEMBLES

4.1 Chapter Overview

In this chapter, we employ the concept of Au NEEs on the working electrode with as-synthesized ZnO nanorods, in the fabrication and characterization of an electrochemical sensor for glucose detection. The ZnO nanorods synthesis recipe is similar to the one described in chapter 2 and the perception of employing Au NEEs in the working electrode is derived from the work explained chapter 3. Here, we study the degree of enhancement in the sensor sensitivity, after the modifying the ZnO nanorods based working electrode, as reported in chapter 2, by employing Au NEEs.

Sensitivity enhancement in an in-vitro glucose sensor using gold nanoelectrode ensembles

Sanghamitra Mandal,^{a*} Mohammed Marie,^b Andrian Kuchuk,^c M.O. Manasreh,^a and Mourad Benamara^c

a University of Arkansas, Department of Electrical Engineering, Fayetteville, AR 72701

b University of Arkansas, Microelectronics Photonics Program, Fayetteville, AR 72701

c University of Arkansas, Institute for Nanoscience and Engineering, Fayetteville, AR 72701

Abstract

Enzymatic electrochemical sensor for glucose detection is fabricated based on hydrothermally grown zinc oxide (ZnO) nanorods. The conception of gold (Au) nanoelectrode ensembles (NEEs) is applied to enhance the sensitivity of the electrochemical sensor under investigation. The characterization of as-synthesized ZnO nanorods on Au and indium tin oxide substrates is performed using X-ray diffraction, scanning electron microscopy, and micro-Raman spectroscopy. The current sensitivity of sensors with and without Au NEEs are computed using

the cyclic voltammetry and amperometric tests executed for the glucose level ranging from 0.01 – 11.00 mM/L. Current sensitivity of 7.50 $\mu\text{A}/\text{mM}$ for a linear range of glucose concentration from 0.01 – 6.50 mM is testified. Response time of 1 s and a low limit of detection of 0.065 mM is reported for the sensor based on Au NEEs. The need of ZnO nanorods in the sensor working electrode, to immobilize enzyme GOx is justified. The presence of Au NEEs boost the sensor current sensitivity by enhancing the rate of electron transfer during the electrochemical reaction.

Keywords: Cyclic voltammetry; electrochemical sensor; gold nanoelectrode; sol-gel process; ZnO nanorods

4.2 Introduction

Electrochemical glucose sensors have emerged as a major research interest in the past few decades due to the rising number of people affected by the metabolic disorder called Diabetes. The concept of electrochemical glucose sensor was first proposed in 1962 [1]. Since then different approaches have been used to develop cost-effective and extremely sensitive electrochemical sensors to control Diabetes [2-9]. The performance parameters for glucose sensors based on different nanomaterial growth approaches are presented in Table 4.1. The two-electrode measurement technique creates a concentration gradient during an electrochemical reaction, which facilitates determination of pH change, diffusion coefficients, electron transfer kinetics and detection of final analyte [4]. The growing number of patient morbidity and mortality due to imprecise blood glucose analyzers lead to the need of accurate glycemic control measurement. The factual challenge concerning glucose sensors is to be able to measure glucose concentrations in the normal and the diabetic blood sugar range. Diabetic people are classified into two levels of glucose concentrations: impaired fasting glucose level, ranging from 3.90 mM/L to 7.80 mM/L and impaired glucose tolerance level, ranging from 7.80 mM/L to 11.0

mM/L [10]. Therefore, electrochemical glucose sensors should be designed to be able to detect up to 11.0 mM/L of glucose concentrations. There are very few papers that report on glucose sensors with high stability and sensitivity in the glucose range above the impaired glucose tolerance level [7, 8, 9] (Table 4.1).

Glucose oxidase (GOx) is the most common enzyme used in enzymatic glucose sensor due to its high stability [3]. Enzyme GOx is a homodimer that catalyzes the oxidation of glucose into H_2O_2 and gluconolactone at high potential [3, 6, 11]. Zinc oxide (ZnO) is a low cost, non-toxic, environmental-friendly, biocompatible, and a biodegradable II-VI semiconducting material with a direct band gap of 3.37 eV [9, 12, 13]. The ZnO nanorods in 100 nm range dimensions provide large surface area to volume ratio, cations with valence states, anions with deficiencies and carrier depletion [12]. Isoelectric point of ZnO is 9.5 and GOx is 4.2 [14, 15]. Consequently, electrostatic interaction between positively charged ZnO nanostructures and negatively charged GOx takes place that leads to easy immobilization of GOx by ZnO nanostructures. Also, the absorption of enzymes in presence of buffer solution becomes easier. Advanced application of Au nanostructures in nanotechnology has emerged in the recent decades due to its unique optical, electronic, and mechanical properties, different from the bulk Au [16]. Recently, Au NEEs are widely used in electrochemical sensing applications since they provide high current densities, high signal to noise ratio, low double layer capacitance, and a larger surface area [16].

The bottom-top approach of cultivating nanostructures is commonly used in nanofabrication processes due to lesser defects, low internal stress, and more homogeneous chemical composition [13]. The simple and cost effective, hydrothermal sol-gel growth technique used to synthesis ZnO nanorods is advantageous over metal-organic chemical vapor deposition, vapor phase epitaxy, vapor phase transport, and vapor-liquid-solid method. The

aqueous hydrothermal sol-gel synthesis method is capable of large scale production of anisotropic ZnO nanorods at a low temperature [13].

In this paper, we report the comparison in sensor sensitivity with and without the presence of Au NEEs. The electrochemical glucose sensors are fabricated using the hydrothermal growth synthesis of ZnO nanorods. The current sensitivity with and without Au NEEs are calculated and discussed. Structural and optical characterization of the as-grown ZnO nanorods on ITO and Au coated glass substrates are studied briefly. The electrochemical characterization of the glucose sensor with and without Au NEEs is performed. The cyclic voltammograms for the sensor with and without ZnO nanorods in the presence and absence of glucose is compared and analyzed. The sensor current sensitivity, response time, and LOD measured using the amperometry technique is in discussed details. It is concluded that the presence of Au NEEs in an electrochemical sensor enhances the sensor current sensitivity under constant experimental conditions. Also, the presence of ZnO nanorods for the immobilization of GOx is essential to enable precise working of the sensor.

4.3 Experimental

4.3.1 Hydrothermal synthesis of ZnO nanorods

The hydrothermal synthesis is a crystal growth technique performed at low temperature and high-pressure conditions. In this technique, properties of superficial water allow the control of particle size and morphology of metal oxides that are insoluble in water under room temperature and normal pressure [17]. Glass samples of dimension 0.70 x 0.70 cm² are coated with 10 nm titanium film and 50 nm of Au film using the e-beam metallization technique. The metal Ti improves Au adhesion on the glass substrate. The glass/Ti/Au substrate and indium tin oxide (ITO) substrates of dimension 0.70 x 0.70 cm² are cleaned with acetone and isopropyl

alcohol inside the ultra-sonication bath for 10 mins each, respectively. The resistance of the Au and ITO coated glass substrates are measured using a multi-meter is 1.5 Ω and 76.0 Ω , respectively.

A 0.50 M ZnO sol-gel is prepared using 1.10 g of zinc acetate dissolved in 10 mL of 2-methoxyethanol. A magnetic stirrer is used to mix the solute and the solvent at a temperature of 70°C for 60 mins, and then sonicated for 30 mins to dissolve the solute particles completely. A milky white solution is obtained that is stirred with 0.30 mL of hexamethylene-amine at a temperature of 70°C for 60 mins. The ZnO sol-gel is aged at room temperature for 24 hrs before use. The glass/Ti/Au and ITO samples are coated with the sol-gel by means of the spin coating technique at an RPM of 4000 rps. The samples are annealed on a hot plate at 120°C for 5 mins to remove solvents from the surface of the ZnO thin film. The process is repeated two more times and finally annealed at 120°C for 30 mins. The ZnO growth solution with a molarity of 0.05 M is prepared with 0.29 g zinc nitrate hexahydrate and 0.14 g hexamethylene-amine, each dissolved in 10 mL of DI water and mixed by means of a magnetic stirrer bar at room temperature for 60 mins. The hexamethylene-amine solution is added dropwise to zinc nitrate solution with continued stirring for another 60 mins. The final solution is filtered from particles using a 0.20 μm syringe filter. The ITO and glass/Ti/Au samples coated with ZnO sol-gel are immersed upside down inside the ZnO growth solution at 85°C for 3 hrs. The process is repeated for another 3 hrs to increase the ZnO nanorods length. The ITO/ZnO nanorods sample surface appears matte white while the Au/ZnO nanorods sample surface appears unchanged. The samples are rinsed thoroughly with DI water to remove unwanted solid particles, dried with nitrogen gas, and annealed on a hot plate at 110°C for 60 mins.

4.2.2 Electrochemical Glucose Sensor Design

The ITO and glass/Ti/Au samples with ZnO nanorods are rinsed with PBS and allowed to dry in atmosphere. This makes the sample surface hydrophilic in nature. Enzyme GOx is prepared by sonicating 40 mg of bovine serum albumin and 20 mg of GOx in 0.40 mL of PBS at room temperature for 60 mins. Bovine serum albumin is a protein substitute used to stabilize GOx and prevent the adhesion of GOx on the Au/glass substrate surface. A droplet of enzyme GOx is drop casted on the ITO/ZnO nanorods and glass/Ti/Au/ZnO nanorods sample surface and allowed to dry at 4°C for 12 hrs. The enzyme GOx easily gets adsorbed physically by the as-synthesized ZnO nanorods on the hydrophilic sample surface. Nafion is drop casted on the sample surface to produce an ion exchanging membrane and dried at 4°C for 4 hrs. Nafion membrane prevents GOx enzyme leakage during the electrochemical reaction because the size of glucose molecules is larger than oxygen and H₂O₂. Nafion membrane stabilizes GOx enzyme and provides a biocompatible atmosphere for the sensor [18]. The samples are stored at 4°C when not in use to avoid reactivity of GOx with atmospheric humidity and moisture.

4.4 Results and Discussion

4.4.1 Structural and optical characterization of ZnO nanorods

The X-ray diffraction (XRD) patterns of the as-synthesized ZnO nanorods on ITO and Au are shown in Fig. 4. 1 (a) and (b), respectively. Crystalline structure and crystallographic orientations of the nanorods were examined ex-situ using the Philips X'Pert-MRD diffractometer with Cu $K\alpha$ -radiation, $\lambda=0.15$ nm, in Bragg–Brentano geometry. The well-defined peaks in the spectra indicate toward the hexagonal (wurtzite) structure of ZnO phase [19]. It should be emphasized that no extra impurity phases are observed by XRD analysis and the formation of pure wurtzite-type ZnO is realized. However, a few Bragg peaks from planes with different

Miller indexes are observed for the ZnO nanorods on ITO sample, whereas only one peak appears for the ZnO nanorods on Au sample. The peak at $\sim 34.45^\circ$ in both ITO and Au samples correspond to the (002) plane of ZnO. The occurrence of just one XRD peak from ZnO nanorods on Au sample, indicate the growth of ZnO only along the c-axis direction, which is the direction normal to the surface of the substrate. The occurrence of several XRD peaks from ZnO nanorods on ITO sample, indicate random orientation of ZnO nanorods. The relative degree of preferred orientation (texture) along c-axis for ZnO nanorods grown on ITO is given by equation 4.2.1 for texture coefficient.

$$T_{(002)} = \frac{\frac{I_{(002)}}{I_{o(002)}}}{\frac{1}{N} \sum \frac{I_{(hkl)}}{I_{o(hkl)}}} \quad (4.2.1)$$

In equation 4.2.1, $I_{(hkl)}$ and $I_{o(hkl)}$ are the measured intensity and standard integrated intensity for (hkl) reflection, respectively, and N is the number of reflections [19]. The $T_{(002)}$ is calculated to be ~ 2.05 for ZnO nanorods on ITO substrate. This indicates that for ZnO nanorods on ITO the c-axis is the preferred growth direction. By considering that the broadening of Bragg peaks results from pure size effects, the lateral coherence length or diameter (d) of ZnO nanorods is directly deduced from the full width at half maximum ($\beta_{(hkl)}$) of the (0 0 2) peak. The mean diameter of ZnO nanorods calculated using the classical Scherrer equation given by equation 4.2.2.

$$d_{(002)} = \frac{0.9 \lambda}{\beta_{(002)} \cos(\theta)} \quad (4.2.2)$$

The mean diameter of the ZnO nanorods is measured as 40 nm for the ITO sample and 54 nm for the Au sample.

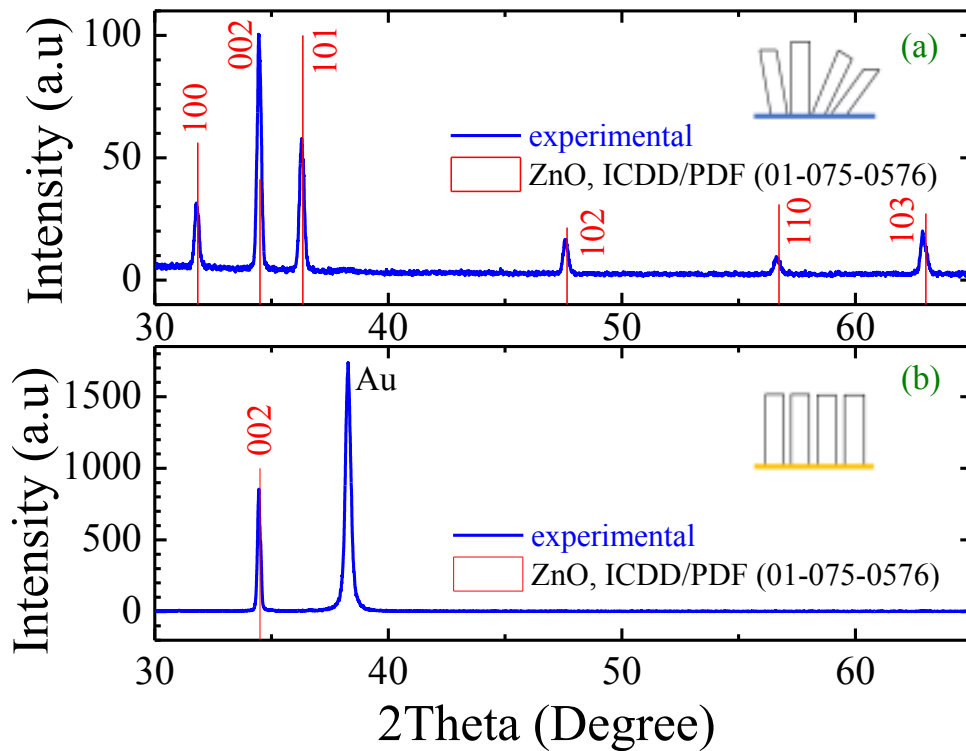


Figure 4. 1 X-ray diffraction spectra measured at room temperature for as-grown ZnO nanorods on **(a)** ITO substrate **(b)** Au/glass substrate.

Figure 4. 2. (a) and (b) display the alignment, shape, and distribution of the as-synthesized ZnO nanorods on ITO and Au substrate, respectively. The top view image of the general morphology is obtained by the field emission - scanning electron microscope (SEM). The majority of the nanorods are evenly distributed with similar lengths and diameters. However, the SEM image for ZnO nanorods on Au in Fig. 4. 2. (b) show better alignment than Fig. 4. 2. (a), and correlate well with the XRD data (Fig. 4. 1).

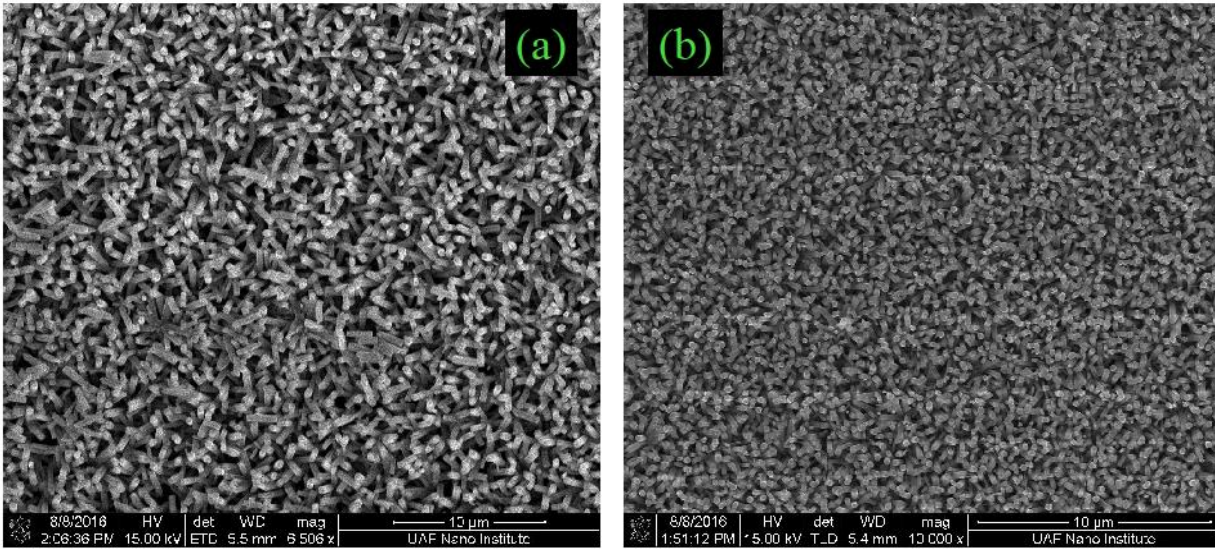


Figure 4. 2 SEM images of ZnO nanorods grown using the hydrothermal sol-gel technique on (a) ITO and (b) Au.

Raman spectroscopy is a non-destructive optical characterization method used to analyze the vibrational properties of ZnO nanorods. The Raman spectrum of ZnO nanorods is slightly different from the spectrum of bulk ZnO due to larger surface to volume ratio [20]. The Horiba LabRAM HR Raman spectroscope is used to investigate the crystallization, structural disorder, and defects in ZnO nanorods [20]. The optical phonon modes in single crystalline ZnO is classified as $\Gamma = A_1+2B_1+E_1+2E_2$. The modes observed in a Raman spectrum depend on the orientation of the crystal, and the polarization of incident and Raman scattered light. Fig. 4. 3 represents the micro-Raman spectra for ZnO nanorods on ITO and Au measured at room temperature in the range from 200 – 800 cm^{-1} . The highly intense, narrow and strong peak known as the non-polar optical phonon E_2 high mode, occurs at 441.2 cm^{-1} and 439.9 cm^{-1} for ITO and Au samples, respectively. This signifies the presence of highly crystalline ZnO nanorods in wurtzite hexagonal crystal phase [20]. The peak at 335.8 cm^{-1} corresponds to the

second order Raman mode due to the E_2 (high) - E_2 (low) multiple-phonon scattering process of ZnO. The intensity of the second order E_2 mode is low due to the strong intensity of the E_2 high mode, thus indicating toward lower levels of oxygen (O_2) defects. The A_1 transverse optical mode is confirmed by a peak around 382.9 cm^{-1} that signify structural disorders in the ZnO lattice [20]. In Fig. 4. 3. the absence of a strong A_1 mode direct toward good lattice structure of ZnO. The peak around 580.6 cm^{-1} denotes the presence of structural defects and impurities. Comparing the two Raman spectra (dotted and straight lines) and the A_1 and E_2 peak intensities, it is noticed that the ZnO nanorods on Au have reduced levels of defects compared to the ITO.

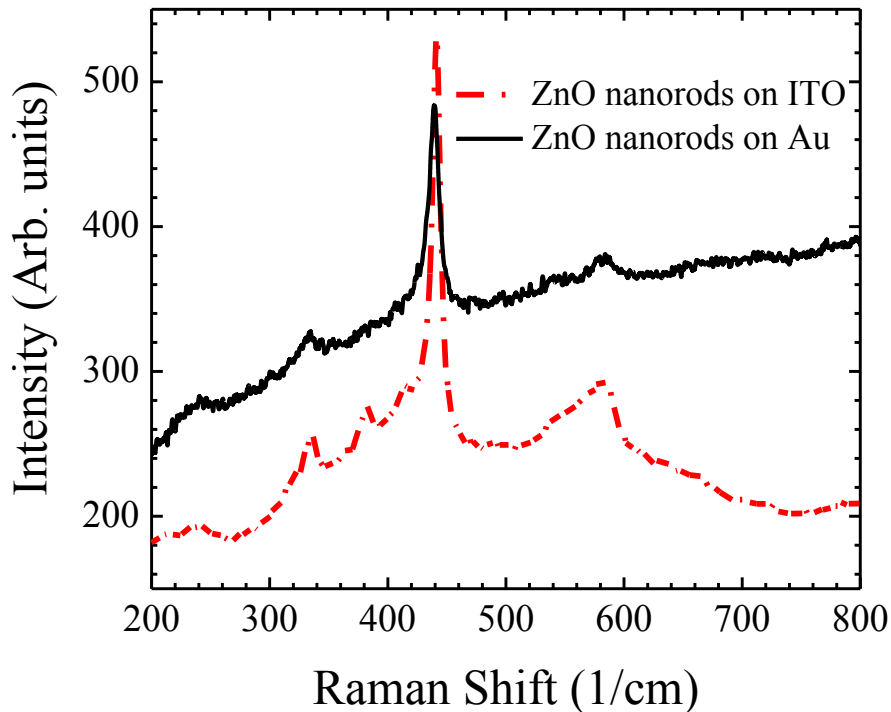
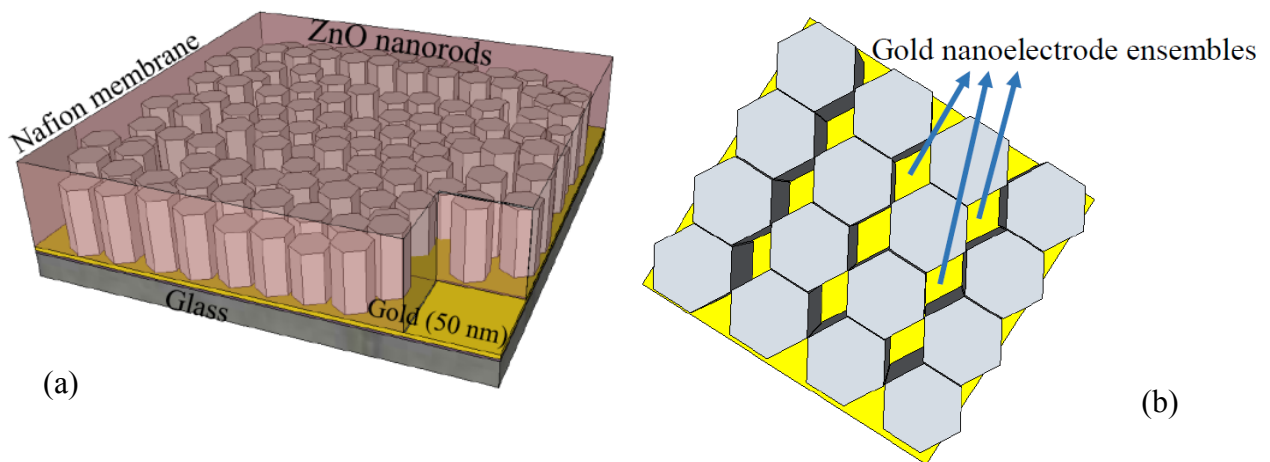


Figure 4. 3 Micro-Raman spectra of as-grown ZnO nanorods on ITO (dotted line) and Au (straight line) measured at room temperature.

4.4.2 Electrochemical characterization of glucose sensor

A four-probe instrument called the Gamry Reference 600 potentiostat is used to perform cyclic voltammetry (potentio-dynamic) measurements utilizing the two-electrode setup. The

electrochemical cell consists of a working electrode, electrolyte, and counter electrode while the voltage drop is measured across the whole cell. The glass/Au/ZnO nanorods/GOx/nafion (Fig. 4. 4. (a)) and ITO/ ZnO nanorods/GOx/nafion samples are used as the working electrode (anode), platinum plate as the counter electrode (cathode), and PBS as the electrolyte that are depicted in Fig. 4. 4. (c). The electrochemical cell made of glass is closed by means of a plastic lid having holes for source meter probes connected to alligator clips at the end to hold the sample and the platinum plate, unlike as shown in Fig. 4. 4. (c). Keithley 2410 source meter is used to produce a potential difference between the anode and the cathode. This potential drop is sufficient enough to initiate the redox reactions at the surface of the working electrode. The small size of Au nanoelectrodes in between ZnO nanorods as displayed in Fig. 4. 4. (b) enable high speed electron transfer within the electrochemical cell and direct low volume analysis [16]. The electron transfer takes place between the anode and cathode via the electrolyte PBS at a constant applied potential under different glucose concentrations. These are the major driving factors behind high current sensitivities of the sensor using ZnO nanorods on Au NEEs (this work) when compared to ITO [9].



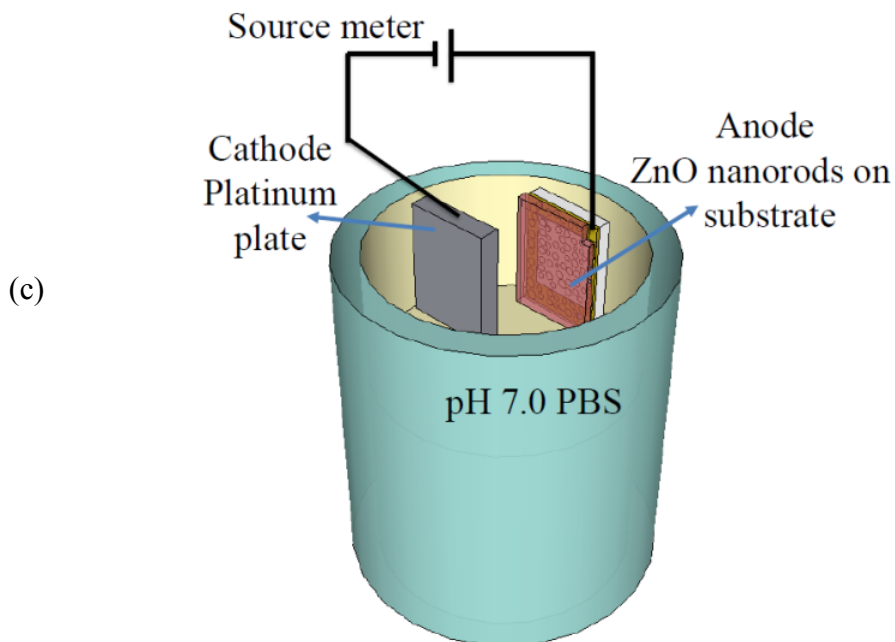


Figure 4. 4 Schematic illustration of (a) the working electrode with ZnO nanorods on Au/Ti/glass substrate, immobilized with GOx and covered with nafion membrane (b) the Au nanoelectrodes ensembles in between nanorods (c) experimental set up for the amperometric test carried at room temperature.

4.4.2.1 Cyclic Voltammetry

The electron transfer mechanism between the sensor anode and cathode inside the electrochemical cell is described by the hysteresis characteristic obtained from cyclic voltammetry measurements. The electrochemical characterization of the glucose sensor using Au NEEs and ITO is compared employing the cyclic voltammograms shown in Fig. 4. 5. (a) - (f) measured for a potential ranging from -0.80 V to 0.80 V.

Figure 4. 5. (a) represent the oxidation reduction mechanism for Au NEEs based sensor at a voltage scan rate of 50 mV/s in the absence and presence of 2.0 mM glucose in 30 mL of PBS. Similarly, Fig. 4. 5. (b) illustrates the electrochemical redox reaction for the sensor based on ZnO nanorods on ITO at a voltage scan rate of 50 mV/s in the absence and presence of 2.0 mM glucose in 30 mL of PBS. A noticeable oxidation potential shoulder at ~0.150 V is observed in

Fig. 4. 5. (a) and (b). The relationship between sensor current and oxidation-reduction reaction rate is explained by the Butler-Volmer equation [21] shown below.

$$i = n * F * A * (k_f[ox] - k_b[red]) \quad (4.4.1)$$

In equation 4.4.1, i is the net current at the electrode equal to either anodic or cathodic current, n is the number of electrons transferred, F is Faraday constant (96485 C/mol), A is the electrode surface area, $[ox]$ is the oxidant concentration, $[red]$ is the reductor concentration, k_f is the forward (oxidation) reaction rate and k_b is the backward (reduction) reaction rate. It can be inferred that sensor current is negative when the rate of reduction of glucose by GOx in the presence of O_2 is more than the oxidation of H_2O_2 . Whereas the sensor current is positive when the rate of reduction of glucose by GOx in the presence of O_2 is lesser than the oxidation of H_2O_2 . Figure 4. 5. (c) indicate a linear relationship between sensor current and voltage scan rates. Faster and higher scan rate (100 mV/s) show higher current and more prominent shoulder. Slower scan rate (20 mV/s) provides sufficient time for glucose to reduce in the presence of catalyst GOx, which generates non-electroactive products one of which is H_2O_2 . Figure 4. 5. (d) compares the voltammograms for both the sensors using Au NEEs and ITO in the presence of 2.0 mM glucose. It is seen that the oxidation potential in both sensors occurs at around 0.15 V. Figure 4. 5. (e) and (f) illustrates the importance of ZnO nanorods in both the sensors. In Fig. 4. 5. (e), cyclic voltammetry tests for glass/Au/ZnO nanorods/GOx/nafion sample is performed in the presence (straight line) and absence (dashed line) of 2.0 mM glucose. Another sample glass/Au/GOx/nafion without ZnO nanorods, is tested in the presence of 2.0 mM glucose (dotted line). It is seen that there is not much difference in the current obtained for the samples with (dashed line) and without (dotted line) ZnO nanorods. Therefore, it is concluded that the presence of ZnO nanorods allow the adsorption of catalyst GOx to increase the reduction of

glucose to H_2O_2 . The role of ZnO nanorods in the working electrode is to increase the active reaction area from a 2D to a 3D area. This further allows more amount of GOx being adsorbed in the 3D nanostructured active area of the working electrode. Figure 4. 5. (f) show consistent voltammetry results for the sensor without Au NEEs indicating the functional importance of 3D ZnO nanorods in the working electrode.

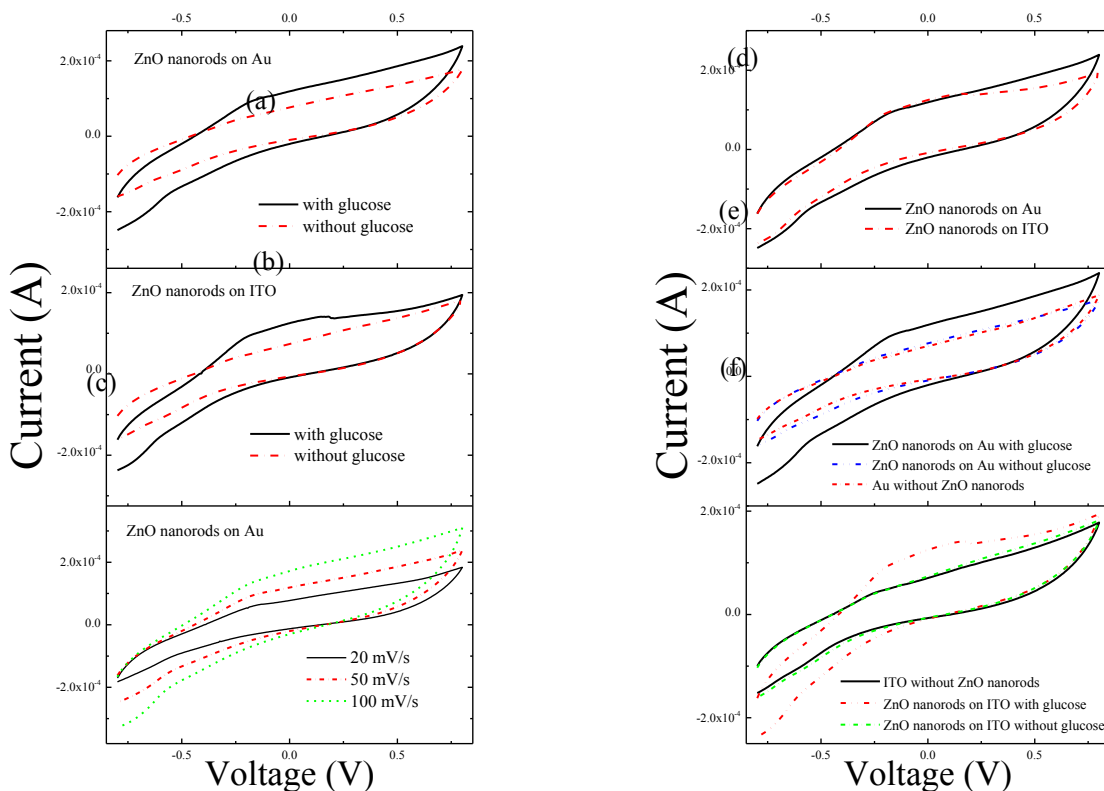
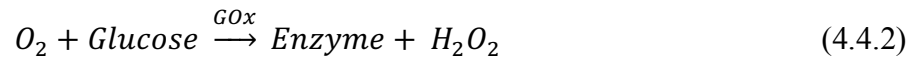


Figure 4. 5 Cyclic voltammograms measured at room temperature for **(a)** ZnO nanorods on Au in the presence and absence of glucose **(b)** ZnO nanorods on ITO in the presence and absence of glucose **(c)** ZnO nanorods on Au in the presence of glucose at different scan rates of 20 mV/s, 50 mV/s, and 100 mV/s **(d)** ZnO nanorods on Au and ITO in the presence of glucose **(e)** ZnO nanorods on Au in the presence (straight line) and absence (dashed line) of glucose compared to sample without ZnO nanorods (dotted line) **(f)** ZnO nanorods on ITO in the presence (dotted line) and absence (green) of glucose compared to sample without ZnO nanorods (straight line).

4.4.2.2 Amperometric response to glucose

The current – time response for the sensor, also known as the steady state amperometric response is illustrated in the inset of Fig. 4. 6. The amperometric test is performed separately on

the sensors using Au NEEs (dotted line) and ITO (straight line) with successive addition of glucose ranging from 0.01 mM – 11.0 mM to 20.0 mL of PBS after every 10 s. The tests are executed at a constant applied potential of 0.15 V selected from the cyclic voltammogram oxidation potential (Fig. 4. 5. (d)). The response time observed from the inset figure, is 1 s and 2 s, for the sensor based on Au NEEs and ITO, respectively. During the amperometric test, reduction of glucose into H₂O₂ in the presence of GOx takes place according to equation 4.4.2 [3].



The rate of reduction is proportional to the amount of glucose concentrations added to the PBS [3]. The current response increases with higher generation of H₂O₂. Oxidation of H₂O₂ takes place according to the equation 4.4.3 [3]



Diffusion of H₂O₂ towards the platinum electrode (cathode) takes place followed by oxidation of H₂O₂ where platinum acts as the transducer. Higher concentration of glucose in PBS leads to higher generation of H₂O₂, thus displaying higher sensor current (Fig. 4. 6 inset). The calibration curve derived from the amperometric response data for the sensors using Au NEEs (round buttons) and ITO (square buttons) are shown in Fig. 4. 6. The current sensitivity for sensor with Au NEEs is calculated to be 7.50 μA/mM for a linear range from 0.01 – 6.5 mM of glucose. The current sensitivity for sensor based on ITO is measured as 6.8 μA/mM for a linear range from 3.0 – 8.0 mM of glucose. The current saturates at 0.13 mA due to saturation of enzyme GOx with higher glucose concentrations. The LOD for the sensor using Au NEEs is calculated to be 0.065 mM by means of equation 4.4.4 [22].

$$LOD = \frac{3 \times Standard\ Error}{Slope} \quad (4.4.4)$$

In equation 4.4.4, the value 3 is the signal to noise ratio, and the standard error is the error of the y-intercept of the linear fit. Limit of detection is the minimum amount of glucose analyte concentration in PBS that is distinguished from zero.

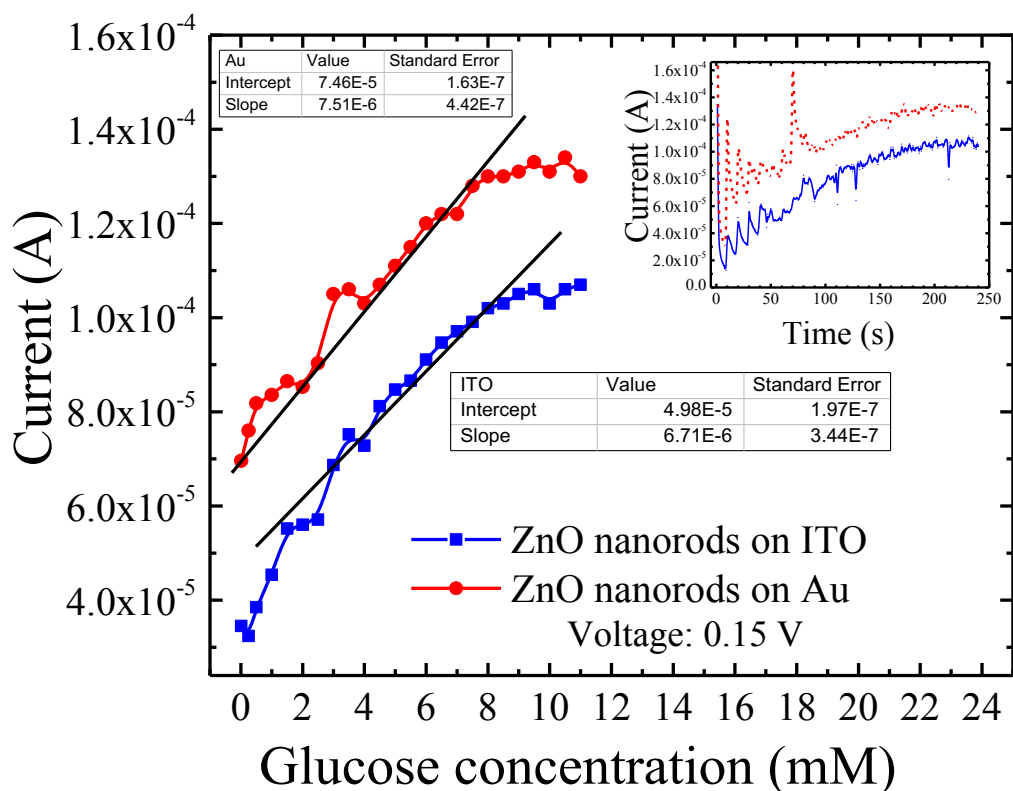


Figure 4. 6 Calibration curve of sensors at different glucose concentrations for an applied oxidation potential of 0.15 V. Inset: Amperometric response of sensors to successive additions of glucose with increasing molarity from 0.01 mM – 11.0 mM after every 10 s time at an applied potential of 0.15 V.

Table 4.1 shows a list of previously reported work on amperometric glucose sensors derived from the synthesis of different nanomaterials and nanostructures. The sensor sensitivity, response time, LOD, range of glucose concentration under test, and the range of glucose concentration exhibiting linear dependence in current response of each sensor are extracted for comparison. It is observed that the sensitivity of [5] and [9] are extremely high for a very small range of linear detection. This range does not fall within the desired glucose detection level in

diabetic patients as mentioned earlier (in section 1). The Au NEEs based glucose sensor presented in our work depicts the desired linear detection range of 3.0 – 8.0 mM. The fabrication process in [8] uses a 1.0 mm thick poly-methyl-siloxane film with 0.02 cm² drilled holes as a template to form Au electrodes. This fabrication method is time consuming and challenging considering the precision of the drilled holes. The sensor reported in our work uses the simple metallization procedure to fabricate Au NEEs between ZnO nanorods. The sensor response time of 1 s is the fastest compared to the other peer reported sensors.

Table 4. 1 The Performance Parameters for Glucose Sensors based on different nanomaterial growth Approachs.

Working electrode material	Sensitivity (mA/mM.cm ²)	Response time (s)	LOD (μM)	Test range (mM)	Linear range (mM)	Reference
3D Graphene-Cobalt Oxide	3.39	3.70	2.50x10 ⁻²	0.01 – 2.75	0.01 – 0.08	[5]
Graphene nanosheets wrapped Copper Oxide nanocubes	2.85x10 ⁻¹	9.00	3.30	0.30 – 7.8	0.30 – 3.3	[6]
ZnO nanowires on Au coated polyester	1.95x10 ⁻²	5.00	50.0	0.20 – 5.4	0.20 – 2.0	[7]
ZnO inverse oval	2.30x10 ⁻²	-	-	0.01 – 35.0	0.01 -18.0	[8]
ZnO nanorods on ITO	10.9	3.00	0.220	0.01 – 2.0	0.60 – 1.4	[9]
ZnO nanorods on ITO	1.39x10 ⁻²	1.00	88.0	0.01 – 11.0	3.00 – 8.00	This work
Au NEEs in between ZnO nanorods	1.53x10 ⁻²	1.00	65.0	0.01 – 11.0	0.01 – 6.5	This work

4.5 Conclusion

Amperometric glucose sensors based on enzyme GOx are the ideal models for screening diabetes. However, challenges like enhancing sensitivity, speed, and stability are being considered for extensive research and investigation. An electrochemical glucose sensor is fabricated by means of the hydrothermal sol-gel technique to synthesize ZnO nanorods. The concept of Au NEEs is employed to enhance the sensitivity of electrochemical glucose sensor.

The ZnO nanorods increase the active reaction area from 2D to 3D area. The as-grown ZnO nanorods are characterized using the XRD, SEM, and micro-Raman spectroscopy. The glucose sensor is characterized by means of the cyclic voltammetry and amperometric test under different glucose concentrations. The simple and cost-effective ZnO nanorods synthesis technique along with the bio-compatibility of GOx and nafion polymer contributes to the best performance of sensors in terms of current sensitivity for glucose detection. The achieved results indicate that Au NEEs based working electrode demonstrate higher current response and faster response time compared to previously reported enzymatic electrochemical sensors. An intensive comparison between sensors based on Au NEEs and ITO is performed. It is verified that the presence of ZnO nanorods in the sensor is essential for the immobilization of enzyme GOx, which aids in the transfer of electrons from the anode to cathode in the presence of the electrolyte.

4.6 Chapter Summary

In this chapter, the glass substrate coated with thin film of ITO and the as-synthesized ZnO nanorods and 50 nm of metallized gold is characterized for structural and optical effectiveness via XRD, SEM, absorbance spectroscopy and micro-Raman spectroscopy. The enzyme GOx is drop casted on the high aspect ratio ZnO nanorods for the fabrication of the working electrode. Nafion polymer membrane is then spin coated on the modified electrode to prevent enzyme leakage during the electrochemical redox reactions taking place inside the electrochemical cell. Device characterization through CV and amperometric iterations is carried out to determine the sensor current sensitivity, response time and the LOD. One of the challenges in the working of electrochemical sensors is insufficient amount of enzyme in the working electrode that leads to inefficient and slow electron transfer during the redox reactions

inside the electrochemical cell. In this study, we observed that the use of Au NEEs along with the ZnO nanorods in the fabrication of electrochemical glucose sensor yield high sensor sensitivity when compared to Si nanowires with Au NEEs.

The work reported in chapters 2, 3, and 4 represent invasive electrochemical sensor fabrication techniques for glucose detection. Non-invasive blood glucose testing involves extraction of blood via needles and is associated with disadvantages like (1) excessive pain, (2) damage to the figure tissues, and (3) blood infections like tetanus. In the following chapter, we study the possibility of designing and testing an optical sensor that could non-invasively and optically detect blood glucose levels.

4.7 References

1. L. C. Clark and C. Lyons, "electrode systems for continuous monitoring in cardiovascular surgery," *Annals of the New York Academy of Sciences*, vol. 102, no. 1, pp. 29-45, 1962.
2. M. Zhang, C. Liao, C. H. Mak, P. You, C. L. Mak and F. Yan, "Highly sensitive glucose sensors based on enzyme-modified whole-graphene solution-gated transistors," *Scientific Reports* 5, 2015.
3. J. Wang, "Electrochemical Glucose Biosensors," *American Chemical Society*, vol. 108, no. 2, pp. 814-825, 2008.
4. B. D. Sherman, M. V. Sheridan, C. J. Dares and T. J. Meyer, "A Two Electrode Collector-Generator Method for the Detection of Electrochemically or Photoelectrochemically Produced O₂," *Analytical Chemistry*, vol. 88, pp. 7076-7082, 2016.
5. X.-C. Dong et al, "3D graphene–cobalt oxide electrode for high-performance supercapacitor and enzymeless glucose detection," *ACS nano*, vol. 6, no. 4, pp. 3206-3213, 2012.
6. M. Liu, R. Liu and W. Chen, "Graphene wrapped Cu₂O nanocubes: non-enzymatic electrochemical sensors for the detection of glucose and hydrogen peroxide with enhanced stability," *Biosensors and Bioelectronics*, vol. 45, pp. 206-212, 2013.
7. D. Pradhan, F. Niroui, and K. T. Leung, "High-performance, flexible enzymatic glucose biosensor based on ZnO nanowires supported on a gold-coated polyester substrate", *ACS applied materials and interfaces*, vol. 2, no. 8, 2409 – 2412, 2010.
8. Y. Xueqiu, J. P. Pikul, W. P. King and J. J. Pak, "Zinc oxide inverse opal enzymatic biosensor," *Applied Physics Letters*, vol. 102, no. 25, p. 253103, 2013.

9. M. Marie, S. Mandal and O. Manasreh, "An Electrochemical Glucose Sensor Based on Zinc Oxide Nanorods," *Sensors*, vol. 15, no. 8, pp. 18714-18723, 2015.
10. S. TA, "Diagnosis and classification of diabetes mellitus," *Diabetes care*, vol. 37, p. S81, 2014.
11. S. Ferri, K. Kojima and K. Sode, "Review of Glucose Oxidases and Glucose Dehydrogenases: A Bird's Eye View of Glucose Sensing Enzymes," *Journal of Diabetes Science and Technology*, vol. 5, no. 5, pp. 1068-76, 2011.
12. J. Gangwar, B. K. Gupta and A. K. Srivastava, "Prospects of Emerging Engineered oxide nanomaterials and their Applications," *Defence Science Journal*, vol. 66, no. 4, pp. 323-340, 2016.
13. K. L. Foo, U. Hashim, K. Muhammad and C. H. Voon, "Sol-gel synthesized zinc oxide nanorods and their structural and optical investigation for optoelectronic application," *Nanoscale Research Letters*, vol. 9, no. 1, p. 429, 2014.
14. Y. Liu, M. Yuan, L. Qiao and R. Guo, "An efficient colorimetric biosensor for glucose based on peroxidase-like protein-Fe₃O₄ and glucose oxidase nanocomposites," *Biosensors and Bioelectronics*, vol. 52, pp. 391-396, 2014.
15. L. Fang, B. Liu, L. Liu, Y. Li, K. Huang and Q. Zhang, "Direct electrochemistry of glucose oxidase immobilized on Au nanoparticles-functionalized 3D hierarchically ZnO nanostructures and its application to bioelectrochemical glucose sensor," *Sensors and Actuators B: Chemical*, vol. 222, pp. 1096-1102, 2016.
16. Y. Zhang, W. Chu, A. D. Foroushani, H. wang, D. Li, J. Liu, C. J. Barrow, X. Wang and W. Yang, "New Gold Nanostructures for Sensor Applications: A Review," *Materials*, vol. 7, pp. 5169-5201, 2014.
17. H. Hayashi and Y. Hakuta, "Hydrothermal Synthesis of Metal Oxide Nanoparticles in Supercritical Water," *Materials*, vol. 3, pp. 3794-3817, 2010.
18. D. e. a. Sodzel, "Continuous sensing of hydrogen peroxide and glucose via quenching of the UV and visible luminescence of ZnO nanoparticles," *Microchim Acta*, vol. 182, pp. 1819-1826, 2015.
19. Powder Diffraction Files, Card No. 01-075-0576, Database Edition, International Centre for Diffraction Data (ICDD), Newtown Square, PA 19073-3273, USA, 2005.
20. A. Umar, K. Byoung-Kye and Y. B. Hahn, "Optical and electrical properties of ZnO nanowires grown on aluminium foil by non-catalytic thermal evaporation," *Nanotechnology*, vol. 18, no. 17, p. 175606, 2007.
21. M. Rudolph, D. P. Reddy and S. W. Feldberg, "A simulator for cyclic voltammetric responses," *Analytical chemistry*, vol. 66, no. 10, pp. 589A-600A, 1994.

22. A. Shrivastava and V. B. Gupta, "Methods for the determination of limit of detection and limit of quantitation of the analytical methods," *Chronicles of Young Scientists*, vol. 2, no. 1, pp. 21-25, 2011.

CHAPTER 5. OPTICAL GLUCOSE SENSOR PROTOTYPE DESIGN

5.1 Chapter Overview

In this chapter, we report the design of an optical sensor for determining the percentage of HbA1c in hemoglobin. The working principle of the proposed sensor is based on the Beer's law of optical absorption. The final prototype is like a black box of dimension 6.0 x 6.0 cm² that comprises of two LEDs, a silicon photodiode and a microcontroller. The sensor is programmed through an algorithm that is capable of (1) determining the molar absorption coefficient of HbA1c and (2) the percentage of HbA1c in hemoglobin. In this work, we are using a chemical assay of HbA1c called Control FD Glycohemoglobin A1c to test the proposed optical sensor prototype.

In-Vitro Optical Sensor designed to estimate Glycated Hemoglobin Levels

Sanghamitra Mandal,^{a*} and M.O. Manasreh,^a

^a University of Arkansas, Department of Electrical Engineering, Fayetteville, AR 72701

Received: 15 March 2018 / Revised: 29 March 2018 / Accepted: 3 April 2018 / Published: 4 April 2018

Abstract

The purpose of this research is to design an optical sensor for evaluating glycated hemoglobin (HbA1c) percentage in hemoglobin. The A1c sensors available in the market use invasive methods while our device explores the possibility of non-invasive monitoring of HbA1c levels in diabetic patients. A prototype is assembled using two light emitting diodes with peak emission wavelength of 535 nm and 593 nm, a photodiode, and a microcontroller. The proposed sensor measures the transmitted intensity in the form of an output voltage. We devise an approach to estimate the percentage of HbA1c in hemoglobin for a given solution. This estimation is based

on the relative change in absorbance due to change in path length and molar absorption coefficients of hemoglobin and HbA1c, at the two wavelengths. We calculate the molar absorption coefficient of HbA1c at 535 nm and 593 nm wavelengths using the sensor, which is performed by a multiple variable regression analysis algorithm fed through the microcontroller. Specifically, the sensor output voltage with respect to the sample concentration is fitted to an exponentially decaying equation model. We use a commercial chemical assay called Control FD Glycohemoglobin A1c with known percentage HbA1c levels to verify our device measurements.

Keywords: Optical sensor; glycated hemoglobin (HbA1c); absorbance spectroscopy; Beer's law; diabetes

5.2 Introduction

Diabetes Mellitus is a serious metabolic disease that has severely affected 422 million people around the world [1]. Diabetic patients are twice as likely to be affected by heart diseases, kidney failure, stroke, eye cataracts, feet amputation, or sudden mortality. Therefore, frequent glucose monitoring is vital for adjusting treatment and retaining normal blood glucose levels. Over the past four decades, enzymatic and non-enzymatic electrochemical glucose sensors have emerged as the most investigated device technologies [2-7]. The glucose monitoring sensors available in the market are mostly electrochemical sensors that are economical and highly accurate [3] [8] but require pricking of finger tissues several times a day to extract capillary blood. The long-term disadvantages of using such invasive needle-based glucose sensors are damaged finger tissues, excessive pain experience, and high risks of infections like tetanus. Other disadvantages of invasive sensors include inaccurate sensor measurements due to noise and patients' movements, and skin irritations caused by direct sensor contact with dermal tissue.

In the past, several types of sensors for glucose sensing have been investigated and developed. However, non-invasive glucose sensor technology is the most recent technique that is pain free and is attributed to direct measurement of glucose level through body tissues from the skin, eyes, or the tongue saliva [9]. The review by Bruen et al [10] focusses on various non-invasive glucose monitoring approaches through biological fluids like interstitial blood, sweat, breath, saliva, and ocular fluid. Lately, various alternative approaches are being explored, like reverse iontophoresis [11], tear glucose dynamics [12-13], and dielectric spectroscopy [14], to develop cost effective and highly sensitive glucose sensors for precise glycemic control. However, optical sensors are the least invasive form of biological instruments. Yet, testing glucose non-invasively using optical methods have not yielded consistent results so far in literature [15]. Since the 1980s, HbA1c concentration started to be accepted as a clinical standard to assess the blood glucose levels in diabetic, pre-diabetic, and pregnant diabetic patients. The challenges involved in using HbA1c as a reliable tool in the routine testing and management of glycemic state is very well described by Weykamp [16].

The estimation of long-term glycemic level in blood is performed using a compound called glycated hemoglobin (HbA1c) found in red blood cells. Hemoglobin (Hb) A1c is a minor red cell constituent that comprises 5 % of the total Hb in normal individuals but up to 15 % in patients with poorly controlled diabetes mellitus [17]. The HbA1c level is tested to indicate the average blood glucose level over the past 12-16 weeks [18] since the average functional lifespan of red blood cells in human body is about 120 days. In 1976, HbA1c was first used to monitor the degree of control of glucose metabolism in diabetic patients [19]. Since then several studies have been conducted to standardize HbA1c level in correlation to the average glucose measurements [20]. The American Diabetes Association has established equations (5.2.1) and

(5.2.2) to calculate the estimated Average Glucose (eAG) level from the percentage of HbA1c in blood hemoglobin [20-21]:

$$\text{eAG (mmol/L)} = 1.59 \times \text{HbA1c (\%)} - 2.59 \quad (5.2.1)$$

$$\text{eAG (mg/dL)} = 28.7 \times \text{HbA1c (\%)} - 46.7 \quad (5.2.2)$$

In this paper, we report the possibility of designing an optical HbA1c sensor. We begin with the description of the experimental setup and then define the chemical assays used to conduct the experiments. Next, we discuss the molar absorbance spectrum, and the calculation of molar absorbance coefficient of the samples using the setup. Calculations are executed by means of multiple variable regression analysis. Finally, we describe the steps to estimate the percentage of HbA1c in the glycohemoglobin A1c samples.

5.3 Methodology

A portable in-vitro sensor is designed for the estimation of HbA1c percentage level. The major device components include two commercially purchased LEDs, a cuvette holder, a photodiode, and an ATmega328 microcontroller. The two LEDs used in the setup are: (1) green LED (HLMP-CM1A-560DD, Broadcom Limited, San Jose, CA, USA) with a peak spectral emission of 535 nm and a bandwidth of 33 nm and (2) yellow LED (TLCY5800, Vishay Semiconductor, Hicksville, NY, USA) with a peak spectral emission of 593 nm and a bandwidth of 11 nm. Disposable polystyrene cuvettes with path length of 1.0 cm are used to hold the chemical assays during the test. A silicon photodiode (FD11A, Thorlabs, Newton, NJ, USA) is used as the light detector that detects the photons emitted by the LED and transmitted through the chemical assays. The photodiode detection ranges from a wavelength of 320–1100 nm of the visible spectrum. The Arduino Uno R3 is an 8-bit microcontroller build onto a single printed circuit board based on the ATmega328P (AVR microcontroller Atmel, San Jose, CA, USA) with

a 32KB of flash memory and 2KB of random access memory. Appendix B presents the code written in C programming language. This code is used for the measurement of photodiode voltage response, and the calculation of molar absorption coefficient via multiple variable regression.

Figure 5. 1 represents the schematic of the experimental setup. The room temperature electroluminescence of the commercial green and yellow LEDs is measured using the Horiba LabRAM HR Evolution spectroscopy (Horiba, Irvine, CA, USA) while biased through the Keithley 2410 source meter (Keithley, Cleveland, OH, USA). The Varian Cary 500 Scan UV-Vis-NIR spectrophotometer (Varian, Palo Alto, CA, USA) is used to measure the absorbance of the reagents used in the experiment. The current prototype is tested by means of a commercially purchased chemical marker called Control FD Glycohemoglobin A1c Level-2 (Audit MicroControls-Product No. K061M-6, Lot No. 06621, Audit MicroControls, Eatonton, GA, USA) [22]. It is a reference control consisting of human blood-based solutions intended to simulate human blood samples containing HbA1c. Various laboratories utilizing FDA approved instruments and reagents have estimated the percentage of HbA1c in the chemical marker Control FD Glycohemoglobin A1c, and reported it to be in the range from 8-13 percentage with a mean around 10 % [22]. The pH for glycohemoglobin A1c is measured using a digital pH meter (Omega-PHH-7011, Omega, Stamford, CT, USA) and is observed to be equal to 6.85 at 19.50°C. We use crystal violet dye (Sigma Aldrich-32675) diluted in DI water, and rhodamine 6g dye (Sigma Aldrich-R4127) dissolved in ethyl alcohol, to validate the molar absorption coefficients estimated using our device against the previously reported results.

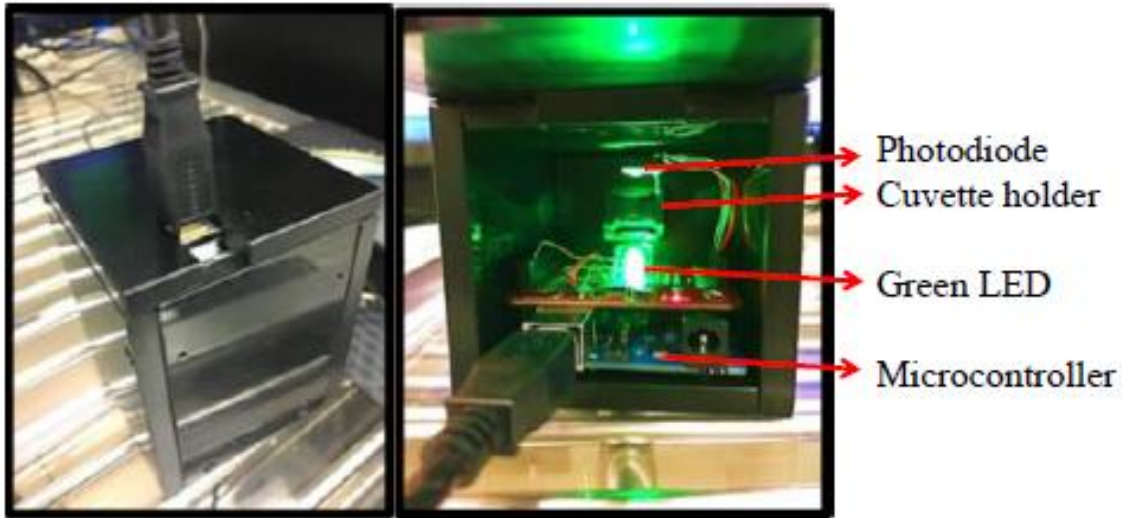
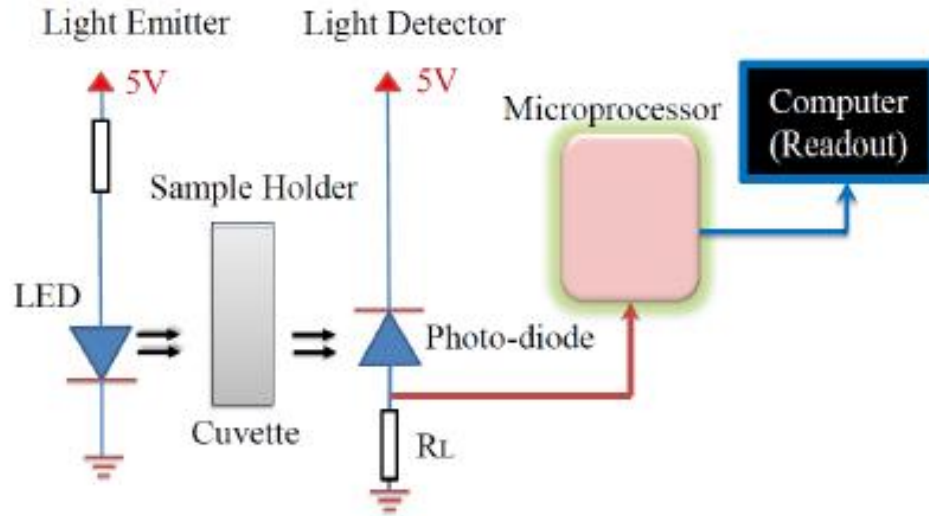


Figure 5. 1 (a) The schematic of the experimental setup used to calibrate and test glycated hemoglobin concentration. (b) Snapshots of the designed prototype.

5.4 Results and Discussion

Here we study the feasibility of designing an optical HbA1c sensor to be able to indicate average glucose level in the last 100-120 days. The working principle of the proposed optical sensor is based on the Beer's law of optical absorption. According to Beer's law, the absorbance (A) of the light wave of wavelength, λ (nm) with an intensity (I_0) passing through a solution of concentration, x (mol L^{-1}) over the path length, l (cm) is given by equation (3) [24-25]. In other words, absorbance (A) is defined as log of ratio of transmitted intensity (I) to incident intensity

(I0) of the light wave [equation (5.2.3)]. The proportionality constant, ϵ (L mol⁻¹cm⁻¹) is called the molar absorptivity or the molar absorption coefficient for a given sample that depends upon the specified wavelength (λ). The transmitted intensity of light (I) as a function of wavelength (λ) is given by equation (5.2.4).

$$A(\lambda) = -\ln\left(\frac{I}{I_0}\right) = \epsilon(\lambda) * l * x \quad (5.2.3)$$

$$I(\lambda) = I_0 * \exp(-\epsilon(\lambda) * l * x) \quad (5.2.4)$$

The properties of the Beer's law are valid even if more than one material absorbs light in the medium. Each absorber contributes to the total absorbance and resulting total absorbance A_{total} is a superposition of the individual absorbing processes. The total absorbance of hemoglobin due to glycosylated and non-glycosylated hemoglobin is given by equation (5.2.5).

$$A_{total} = A_{Hb,A1c} + A_{Hb,NonA1c} = \epsilon_{Hb,A1c} * l * x_{Hb,A1c} + \epsilon_{Hb,NonA1c} * l * x_{Hb,NonA1c} \quad (5.2.5)$$

Here we consider that all the parameters are averaged over oxyhemoglobin and deoxyhemoglobin. The arterial blood in normal humans comprises of roughly 98 % oxyhemoglobin and 2 % deoxyhemoglobin [26]. The percentage of HbA1c (% HbA1c) in total hemoglobin in terms of molar concentrations of HbA1c ($x_{Hb,A1c}$), non-glycosylated hemoglobin ($x_{Hb,NonA1c}$) and total hemoglobin (x_{Hb}) is given by equation 5.2.6.

$$\% \text{ HbA1c} = \frac{x_{Hb,A1c}}{x_{Hb,A1c} + x_{Hb,NonA1c}} * 100 = \frac{x_{Hb,A1c}}{x_{Hb}} * 100 \quad (5.2.6)$$

We calculated the % HbA1c in total hemoglobin using parameter R and the molar absorption coefficient for glycosylated hemoglobin ($\epsilon_{Hb,A1c}$) and non-glycosylated hemoglobin ($\epsilon_{Hb,NonA1c}$) using equation 5.2.7. The parameter R is defined as the ratio of change in absorbance as the path length changes (l_1 to l_2) at two different wavelengths λ_1 and λ_2 [equation 5.2.8]. The detailed derivation of equations 5.2.7 and 5.2.8 are stated in Appendix B.

$$\% \text{HbA1c} = \frac{\epsilon_{\text{Hb,NonA1c}}(\lambda_1) - R * \epsilon_{\text{Hb,NonA1c}}(\lambda_2)}{R * (\epsilon_{\text{Hb,NonA1c}}(\lambda_2) - \epsilon_{\text{HbA1c}}(\lambda_2)) - (\epsilon_{\text{HbNonA1}}(\lambda_1) - \epsilon_{\text{HbA1c}}(\lambda_1))} * 100 \quad (5.2.7)$$

$$R = \frac{\delta A_{\lambda_1}}{\delta A_{\lambda_2}} = \frac{\ln \frac{I(l_1)}{I(l_2)_{\lambda_1}}}{\ln \frac{I(l_1)}{I(l_2)_{\lambda_2}}} \quad (5.2.8)$$

The two wavelengths selected for the above calculations are based on the selective absorbance of HbA1c in the wavelength ranging from 520-610 nm [discussed in section 3]. Similar principle is employed in pulse oximetry or photoplethysmography to recognize oxygen saturation only for the arterial compartment of blood [25].

The molar absorbance coefficients used in equation 5.2.7 for $\epsilon_{\text{HbNonA1c}}$ is derived from [27] and ϵ_{HbA1c} is estimated using our device. More specifically we use multi-variable regression analysis method described as follows. The transmitted intensity of the LED after it passes through the sample for a fixed path length (l), varies with respect to the sample concentration (x) [equation 5.2.4]. The proposed sensor measures the transmitted intensity in the form of photodiode output voltage. The output voltage is then plotted as a function of concentration that is then fitted along an exponentially decaying expression [equation 5.2.9].

$$y = A + B * \exp(-C * x) \quad (5.2.9)$$

In equation 5.2.9 A , B , and C are three unknown variables, x is the concentration, and y is the output voltage. Equation 5.2.9 is modelled against the transmitted intensity equation 5.2.4. By comparing equations 5.2.4 and 5.2.9, we get molar absorption coefficient $\epsilon=C/l$, where l is the path length of the cuvette, equal to 10 mm.

The first objective of our analysis is to determine the wavelengths at which we observe selective absorbance due to glycated hemoglobin (HbA1c) in blood hemoglobin. Figure 5. 2 represents the absorption spectra of Control FD Glycohemoglobin A1c. It is observed that

glycohemoglobin A1c demonstrates strong absorption around 412 nm (Soret Band), and 541 nm and 577 nm (Q Bands). The wavelength around 412 nm corresponds to the blue light region of the visible spectrum, while 541 nm and 577 nm corresponds to the green and yellow light range of the visible spectrum. Since, glycohemoglobin A1c shows a strong absorbance in the wavelength range of 520-610 nm, we use green and yellow LEDs as the light emitter in the proposed setup. We did not use a blue LED as the light emitter in our prototype because color blue is complementary to color red [23]. As shown in Fig. 5.2, on passing a blue light through a red colored material, all the light photons are absorbed by the material and there are no transmitted photons. The photo-detector used in our prototype was not be able to detect any photons transmitted through the material which in our case is Control FD glycohemoglobin A1c.

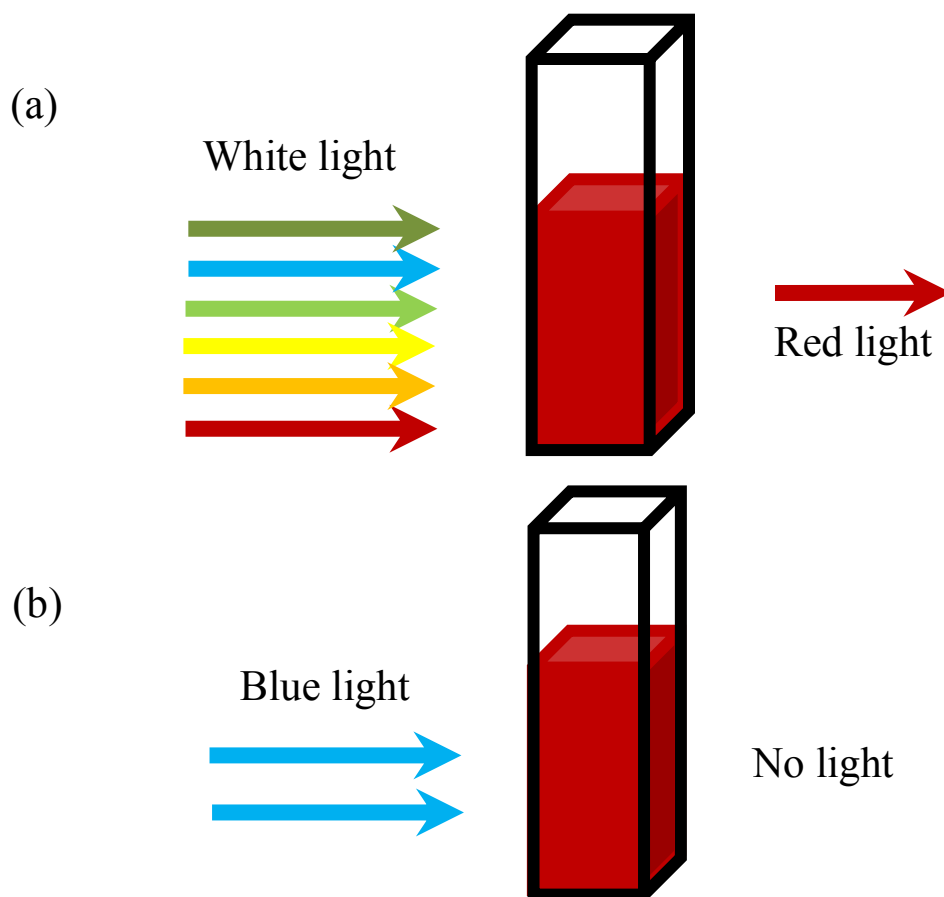


Figure 5. 2 Schematic showing a cuvette containing a red sample under the influence of (a)

white light, we see the red color of the sample and **(b)** blue light, all photons are absorbed, and no photons are transmitted.

In Figure 5. 3, we also show the electroluminescence (EL) intensities of the green and yellow LEDs. It is seen that the peak emission wavelength for green LED is at 535 nm and the full width at half maximum spectral bandwidth is about 33 nm. The yellow LED has a peak emission spectrum at 593 nm and the full width at half maximum spectral bandwidth is about 11 nm. The overlapping of the EL emission spectra of the green and yellow LEDs, and the absorbance spectrum of HbA1c show that the green LED used in the setup can very well be used to detect HbA1c. We also measure the absorbance of two dyes to verify our method of estimating molar absorption coefficient. It is understood from Figure 5. 2 that the absorbance spectra of rhodamine 6g, and crystal violet overlaps the EL spectra of the green, and yellow LED, respectively.

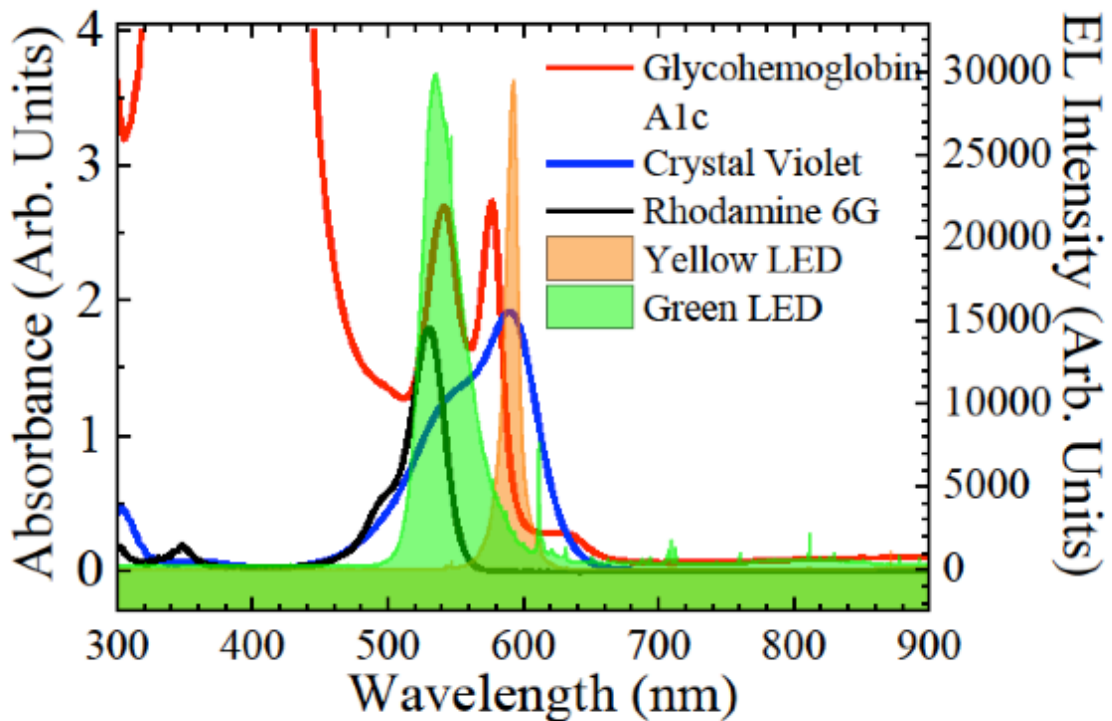
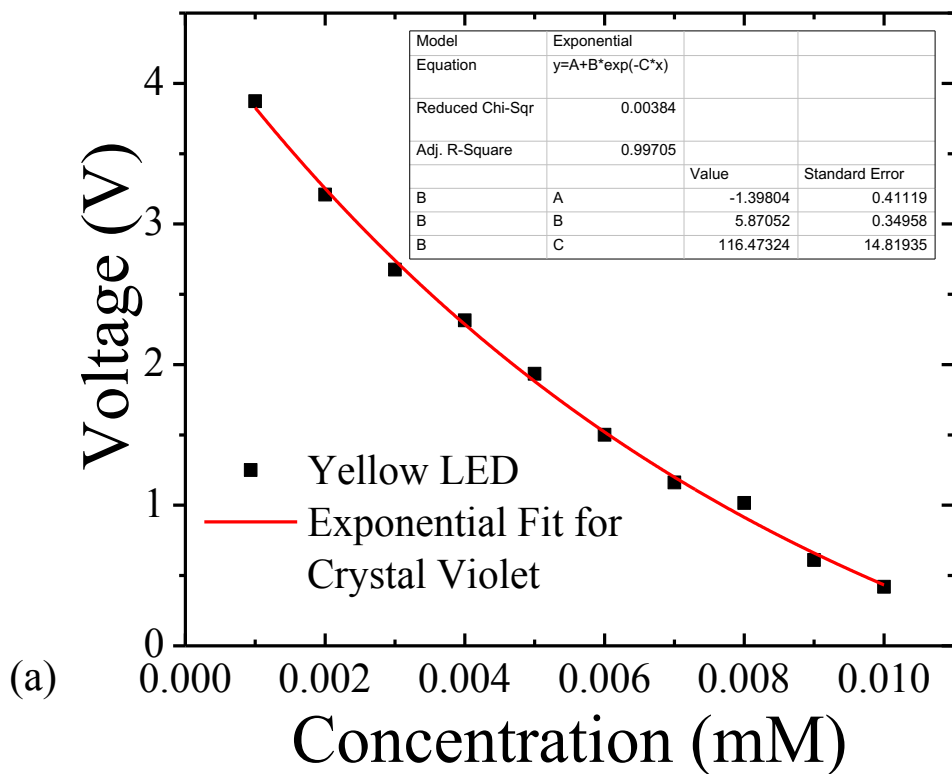


Figure 5. 3 Electroluminescence of green and yellow LED measured at room temperature compared to the absorbance of Glycohemoglobin A1c, crystal violet, and rhodamine 6g solutions.

5.4.1 Molar Absorption Coefficient Calculation

We show the photodiode voltage response with respect to the concentrations of crystal violet dye using the yellow LED in Figure 5. 3 (a) and rhodamine 6g dye using green LED in Figure 5. 4 (b). In Figure 5. 3 (a) and (b) each of the voltage data points corresponding to the sample concentrations are averaged over 500 voltage readings. The regression statistics of Figure 5. 4 (a) shows an adjusted R-square value of 99.71 %, which indicates how well the data points fit the exponential model. In Figure 5. 4 (b), the adjusted R-square value is 96.36 % that indicates the goodness-of-fit for our regression model. The voltage data points then are fitted (red line) to the exponentially decaying function model given by equation 5.2.9. From the value of *variable C*,

the molar absorption coefficient for crystal violet at yellow light wavelength is $116.48 \pm 14.82 \text{ mM}^{-1}\text{cm}^{-1}$ and for rhodamine 6g at green light wavelength is $115.96 \pm 23.42 \text{ mM}^{-1}\text{cm}^{-1}$. These calculated molar absorption coefficients for crystal violet and rhodamine 6g are in good agreement with the published values of crystal violet, $112 \text{ cm}^{-1} \text{ mM}^{-1}$ [28] and rhodamine 6g, $116 \text{ cm}^{-1} \text{ mM}^{-1}$ [29]. Thus, the proposed method reliably estimates the molar absorption coefficient for a given solution.



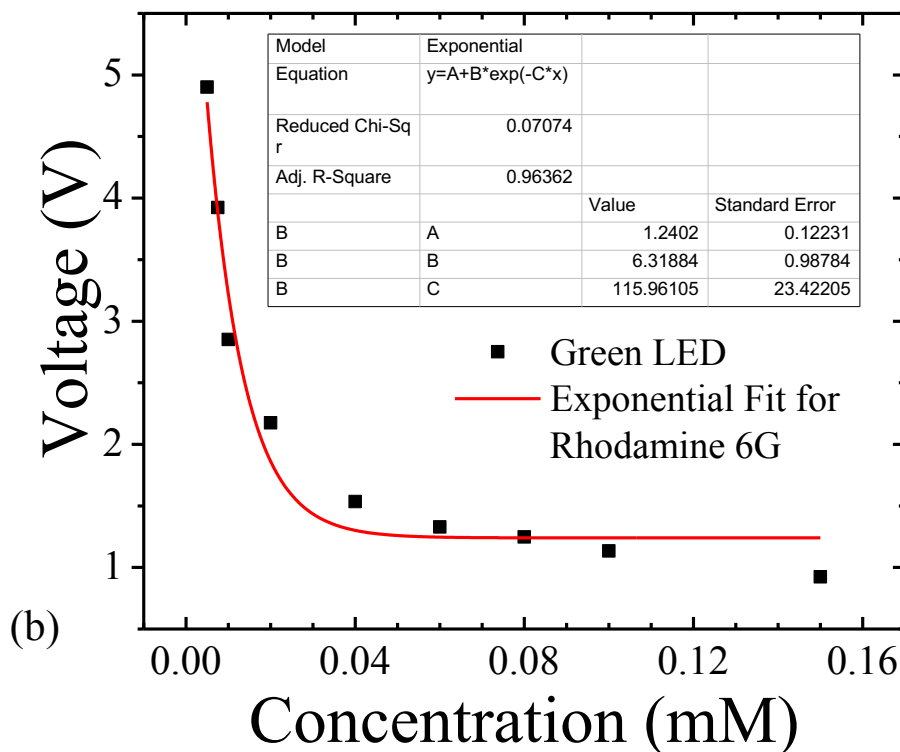


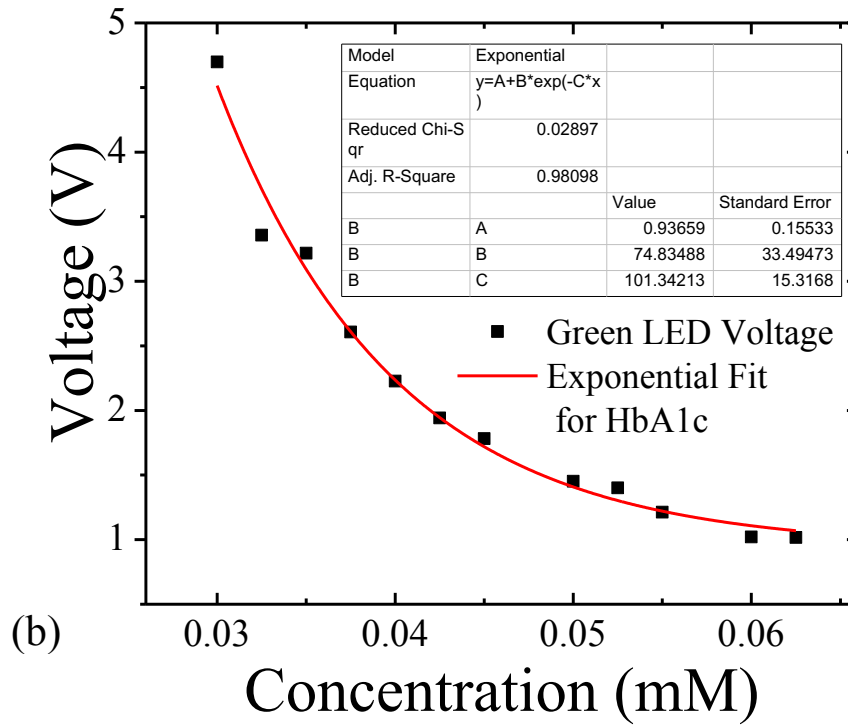
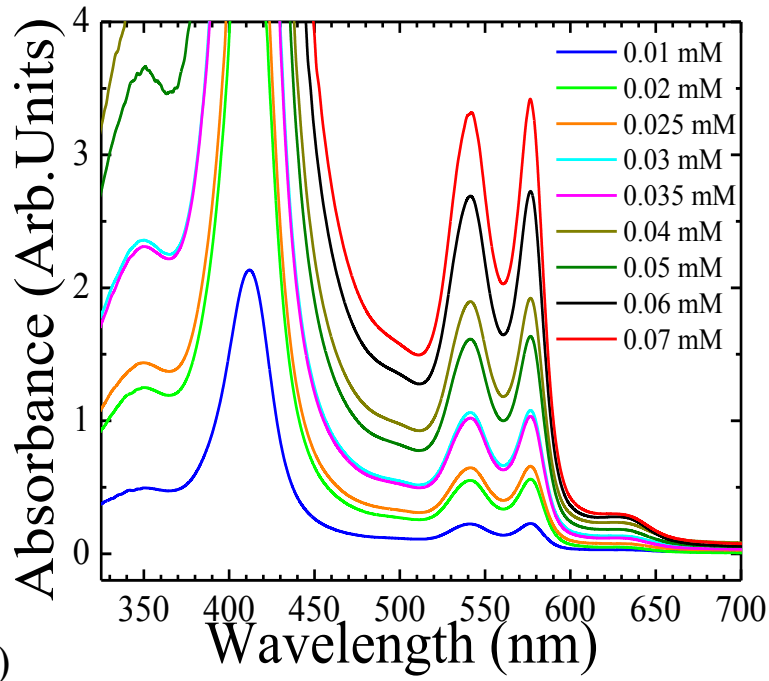
Figure 5. 4 Photodiode output voltage (averaged over 500 voltage readings) as a function of concentration of (a) Crystal Violet synthetic dye using the yellow LED and (b) Rhodamine 6g fluorescent dye using the green LED. The data points are fitted to an exponentially decaying equation model via a three-variable regression analysis to find molar absorption coefficient.

Figure 5. 5 (a) represents the room temperature absorbance spectra of glycohemoglobin A1c solutions for concentrations ranging from 0.01-0.07 mM. It is observed that an increase in the concentration leads to an increase in the absorbance, specifically around 541 nm and 577 nm. This implies that as the concentrations increase, the transmitted light intensity of the green and yellow LEDs should decrease. The photodiode voltage response corresponding to different glycohemoglobin A1c concentration is shown in Figure 5. 5 (b) using green LED, and Figure 5. 5 (c) using yellow LED. Each of the voltage data points are averaged over 500 readings measured at the corresponding concentrations. The exponential fit *variable C* gives the molar absorption coefficient of glycohemoglobin A1c solution under green light to be, 101.34 ± 15.32

mM⁻¹cm⁻¹. Similarly, the molar absorptivity of glycohemoglobin A1c solution under yellow LED is calculated as 34.12 ± 10.41 mM⁻¹cm⁻¹. The marker Control FD glycohemoglobin A1c, comprises of glycated hemoglobin and non-glycated hemoglobin. Therefore, to calculate the molar absorption coefficient for 100 % glycated hemoglobin, we factor out the absorbance due to non-glycated hemoglobin according to equation 5.4.1. The detailed derivation of equation 5.4.1 is specified in Appendix C.

$$\epsilon_{Hb,A1c} = \frac{100 * \epsilon_{Hb} - \epsilon_{Hb,Non\ A1c} * (100 - \%Hb, A1c)}{\%HbA1c} \quad (5.4.1)$$

The molar absorption coefficient of non-glycated hemoglobin $\epsilon_{Hb,Non\ A1c}$ is 48.34 mM⁻¹cm⁻¹ at 535 nm wavelength (green LED) and 9.07 mM⁻¹cm⁻¹ at 593 nm wavelength (yellow LED) [27]. The estimated molar absorption coefficient of the marker glycohemoglobin A1c solution is represented by ϵ_{Hb} . Since the percentage of HbA1c level of marker lies between 8-13 percentage [22], we estimate the molar absorption coefficient of HbA1c, $\epsilon_{Hb,A1c}$ value for both the upper and lower limits. Using equation 5.4.1, $\epsilon_{Hb,A1c}$ is calculated to be 456.06 ± 117.82 mM⁻¹cm⁻¹ (for, % HbA1c = 13 %) and 710.88 ± 191.46 mM⁻¹cm⁻¹ (for, % HbA1c = 8 %), at 535 nm wavelength (green LED). Similarly, $\epsilon_{Hb,A1c}$ is calculated to be 201.77 ± 80.04 mM⁻¹cm⁻¹ (for, % HbA1c = 13 %) and 322.20 ± 130.06 mM⁻¹cm⁻¹ (for, % HbA1c = 8 %) at 593 nm wavelength (yellow LED).



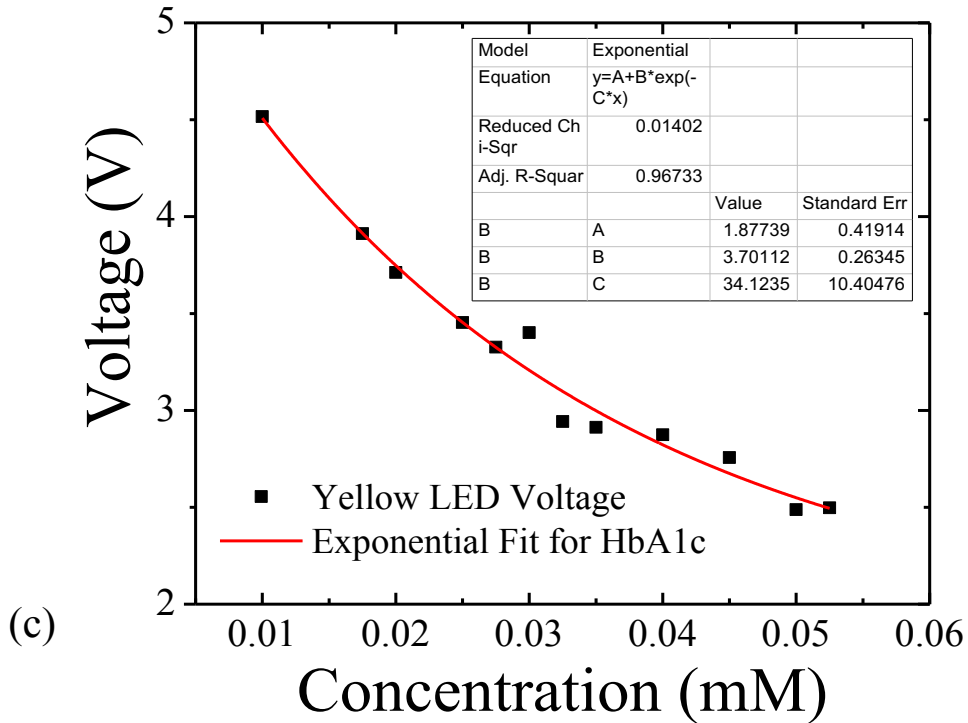


Figure 5.5 (a) The absorption spectra of diluted concentrations of glycohemoglobin A1c solutions measured at room-temperature. (b) Photodiode output voltage (averaged over 500 voltage readings) as a function of concentration for diluted concentrations of glycated hemoglobin using green LED and (c) yellow LED. The data points are fitted to an exponentially decaying equation using a three-variable regression analysis.

5.4.2 Estimation of HbA1c percentage in a solution

Here, we estimate the molar absorption coefficient of glycohemoglobin A1c solutions by employing our device. However, one can estimate the molar absorption coefficients of the samples under test via other methods [30-32]. In that case the proposed sensor will only measure the value of R parameter using equation 5.2.8. Next the percentage of HbA1c level is estimated through equation 5.2.7 by substituting the pre-determined molar absorption coefficient values and the calculated R values. The calculation of R parameter is performed by measuring transmitted intensity for the samples at λ_1 and λ_2 equal to 535 nm (green LED) and 593 nm (yellow LED), respectively for the path lengths of 10 mm and 5 mm.

$$R = \frac{\ln \frac{I(10 \text{ mm})}{I(5 \text{ mm})}_{\text{Green}}}{\ln \frac{I(10 \text{ mm})}{I(5 \text{ mm})}_{\text{Yellow}}} \quad (5.4.2)$$

Table 5.1 represents the observed R values for different samples of marker glycohemoglobin A1c calculated using the proposed sensor. Here, the molar absorption coefficients values of $\epsilon_{Hb, Non A1c}$ and ϵ_{Hb} , declared in section 3.1. are used for the percentage of HbA1c estimation [Equation 5.4.1]. Table 5.1 lists the final percentage values of HbA1c calculated in the marker glycohemoglobin A1c solutions and are found to be in close agreement with the measurements from other laboratories [22].

Table 5. 1 Estimated percentage of glycated hemoglobin

Sample No.	Molar Concentration of Control FD HbA1c (mmol/L)	R	HbA1c (8%)	HbA1c (13%)
1	0.030	2.82	10.31 %	16.75 %
2	0.035	2.97	7.99 %	12.98 %
3	0.040	2.86	9.54 %	15.50 %
4	0.050	2.96	8.16 %	13.27 %
5	0.053	2.97	8.02 %	13.03 %

5.5 Conclusions

The use of glycated hemoglobin (HbA1c) sensors for tracking long term glycemic state in diabetic patients is more convenient as compared to the temporal information gained from blood glucose sensors. The currently available electrochemical HbA1c sensors are based on liquid chromatography, immunoassay, electrophoresis, or spectrophotometry techniques that require invasive blood extraction. There is a pressing need for the development of advanced non-invasive optical HbA1c sensors with better selectivity, stability, and accuracy. This research proposes the design of an inexpensive optical sensor prototype to calculate (1) the molar absorption coefficients of a solution using multiple variable regression analysis, and (2) the

percentage of HbA1c in a solution. The working principle of the proposed sensor is based on the Beer's Law of optical absorption. The molar absorption coefficients measured for two known dyes using our prototype is in good agreement with the previously established results. Also, the calculated percentage of HbA1c in the solution falls within the standard range of values established by other laboratories. However, it is important to mention that not all instruments measure values in good agreement with each other. Few of the possible sources of errors include gravimetric and volumetric error, path length error, beam alignment error, reflection error, and error due to stray radiations [33]. We use a range of molar concentrations of the chemical assay at which our current setup is the most sensitive. This is one of our device limitations. However, the concentration of whole blood is much higher and requires a setup enhancement by using a high sensitivity photodiode sensor and brighter LEDs. Further research and enhancement of our current prototype by testing pure glycated blood samples and actual human blood samples is required, which could eventually lead to a commercialized portable HbA1c sensor.

Acknowledgments: The authors wish to acknowledge and thank Dr. Timothy J. Muldoon for his guidance and insightful suggestions throughout this work. This research is partially supported by the University of Arkansas, Fayetteville and National Aeronautics and Space Administration – EPSCoR Program (242026-1/NNX11AQ36A).

Author Contributions: Authors contributed equally to the manuscript in its final form.

Conflicts of Interest: Sanghamitra Mandal performed the measurements, processed the experimental data, implemented the analysis, drafted the manuscript and designed the figures. M. O. Manasreh was involved in the interpretation of the results and he supervised the work. All the authors discussed the results and commented on the manuscript.

Appendix A

```
#include <EEPROM.h>
#include <Math.h>

// Sensor input variables
int sensorPin = A0; // select the input pin for the photodiode
int ledPin2 = 7; // select the pin for the LED
int sensorValue = 0; // variable to store the value coming from the sensor
int eeAddress = 0; // Location we want the data to be put in EPROM.
//sequentially stores 10 readings from your analog sensor into an array, one by one.
//With each new value, the sum of all the numbers is generated and divided
//producing an average value
const int numReadings = 500; // Number of sensor readings you want to take at one
concentration
int total = 0; // sensor reading:
double volts = 0;
double current = 0;
double totalV = 0; // the running total Voltage
double totalI = 0; // the running total Current
double averageV = 0; // the average Voltage
double averageI = 0; // the average Current
double concentration = 0; // sample concentration
int maxcount = 11; // No. of sample concentrations
//variables for exponential regression
double x[11]; // always set the size of array equal to maxcount
double y[11]; // always set the size of array equal to maxcount
double dx[10]; // always set the size of array equal to (maxcount-1)
double dy[10]; // always set the size of array equal to (maxcount-1)
double cx[10]; // always set the size of array equal to (maxcount-1)
double dq[10]; // always set the size of array equal to (maxcount-1)
double b_initial[9]; // always set the size of array equal to (maxcount-2)
double a_initial[10]; // always set the size of array equal to (maxcount-1)
double b_int_avg=0;
double a_avg=0;
double c_initial[11]; // always set the size of array equal to maxcount
double lnyc[11]; // always set the size of array equal to maxcount
double xbar=0;
double ybar=0;
double xybar=0;
double xsqbar=0;
double slope=0;
double intercept=0;
double syx = 0;
double std_err = 0;
double stderr_Slope = 0;
double stderr_Intercept = 0;
```

```

double a=0;
double b=0;
double c=0;
double a_err=0;
double b_err=0;
double c_err=0;
int abor(double y[11],double cc) // always set the size of array equal to maxcount
{
    int returnpara=0;
    double e=0;
    for (int i=0; i<maxcount-1; i++)
    {
        e = (y[i+1]-cc)/(y[i]-cc);
        if(e<=0)
        {
            returnpara=1;
            break;
        }
    }
    return returnpara;
}
// always set the size of array y and x equal to maxcount, dx equal to
maxcount-1
double Devi(double cc, double y[11], double x[11],double dx[10])
{
    double avG=0;
    double pre_ee=0;
    double ee=0;
    double growthfactor[maxcount-1];
    double Deviation = 0;
    for (int i=0; i<maxcount-1; i++)
    {
        pre_ee = (y[i+1]-cc)/(y[i]-cc);
        ee = log(pre_ee);//denominator
        avG = avG + ee;
        growthfactor[i] = exp(ee/dx[i]); //save
    }
    avG = exp(avG/(x[maxcount-1]-x[0])); //exp added
    ee = 0;
    for (int i=0; i<maxcount-1; i++)
    {
        Deviation = Deviation + abs(avG-growthfactor[i]);
    }
    return Deviation;
}
void setup()

```

```

    {
        Serial.begin(9600);
        pinMode(ledPin2, OUTPUT);
    }
void loop()
{
    digitalWrite(ledPin2, HIGH);
    delay (3000);
    stabilizing delay
    for (int j=0; j<maxcount; j++)
    {
        totalV = 0;
        total = 0;
        totalI = 0;
        for (int i = 0; i<numReadings; i++)
        {
            sensorValue = analogRead(sensorPin);
            volts = double (sensorValue) * (5.0 / 1023.0);
            out:
                Serial.print("\t Sensor = ");
            monitor:
                Serial.println(sensorValue);
                Serial.print(" Volts = ");
                Serial.println(volts,4);
                delay(10);
                total = total+ sensorValue;
                totalV = totalV+volts ;
            }
            averageV = totalV / numReadings;
            if (j==1)
                concentration=concentration + 4;
            else if (j>1)
                concentration = concentration + 2;
            Serial.print(" \t Average Voltage(Volts) = ");
            Serial.println(averageV,4);
            Serial.print(" Concentration (mM) = ");
            Serial.println(concentration,3);
            x[j] = concentration;
            y[j] = averageV;
            delay(14000);
        }
    }
}
// initialize serial communication with computer:
// Set data rate to 9600 bps
// delay to start recording values or LED
// read the value from the sensor:
// map it to the range of the analog
// print the results to the serial
// wait 10 milisecond before the next loop
// for the analog-to-digital converter to settle
// after the last reading:
// calculate the average Voltage:
// print the result to the serial monitor
// send it to the computer as ASCII digits
// print the result to the serial monitor
// send it to the computer as ASCII digits
// delay to change sample concentration
// Exponential curve fitting t equation y =
A+B*exp(C*x)

```



```

// Estimation of c using a and b.
// initial variables

for (int j=0; j<maxcount-1; j++)
{
dx[j] = x[j+1]-x[j];
dy[j] = y[j+1]-y[j];
cx[j] = (x[j]+x[j+1])/2;
dq[j] = dy[j]/dx[j];
}

// pre-estimation of b

b_int_avg =0;
for (int jj=0; jj<maxcount-2; jj++)
{
b_initial[jj] = (log(dq[jj+1]/dq[jj]))/(cx[jj+1]-cx[jj]);
}
for (int jj=0; jj<maxcount-2; jj++)
{
b_int_avg = b_int_avg + b_initial[jj];
}
b_int_avg = b_int_avg/(maxcount-2);
Serial.print(" b-initial = ");
Serial.println(b_int_avg,4);

// pre-estimation of a

for (int j=0; j<maxcount-1; j++)
{
a_initial[j]= dy[j]/(exp(b_int_avg*x[j+1])-exp(b_int_avg*x[j]));
}
a_avg =0;
for (int j=0; j<maxcount-1; j++)
{
a_avg += a_initial[j];
}
a_avg = a_avg/(maxcount-1);
Serial.print(" a-initial = ");
Serial.println(a_avg,4);

// estimation of c and standard error in c;

for (int j=0; j<maxcount; j++)
{
c_initial[j] = y[j] - a_avg*exp(b_int_avg*x[j]);
}
for (int j=0; j<maxcount; j++)
{
c += c_initial[j];
}
c=c/maxcount;
double scaledY = 0.001;

```

```

c=y[maxcount-1]-scaledY;
double deltaC =0;
if (a_avg>0)
    deltaC = -scaledY;
else
    deltaC = scaledY;
double abortt=0;
abortt = abor(y,c);
while (abortt>0)
    {
    c=c+deltaC;
    abortt = abor(y,c);
    }
Serial.print(" c-initial = ");
Serial.println(c,4);
double Bvar1=0;
double Bvar2=0;
Bvar1=Devi(c,y,x,dx);
deltaC=-deltaC;
Serial.print(" delta C = ");
Serial.println(deltaC,4);

double w = 0;
while(abs(deltaC)>0.00001 && w<100)
    { w=w+1;
    Serial.print(" w = ");
    Serial.print(w);
    Serial.print(" deltaC = ");
    Serial.println(deltaC,6);
    Serial.print(" c = ");
    Serial.println(c,6);
    Serial.print(" Bvar1 = ");
    Serial.println(Bvar1,4);
    abortt = abor(y,c+deltaC);
    Serial.print(" abort = ");
    Serial.println(abortt,4);
    if (abortt>0)
        {
        deltaC=deltaC/2;
        }
    else
        {
        c=c+deltaC;
        Bvar2 = Devi(c,y,x,dx);
        Serial.print(" Bvar2 = ");
        Serial.println(Bvar2,4);

```

```

    if (Bvar2<Bvar1)
    {
        Bvar1=Bvar2;
    }
else
    {
        deltaC=-deltaC/2;
    }
}
}

// linear regression on  $\ln(y-c) = \ln(a) + b*x$  using estimated c value
// consider a linear plot for  $\ln(y-c)$  vs. x; slope=b and intercept =  $\ln(a) \Rightarrow a =$ 
exp (intercept)
for (int j=0; j<maxcount; j++)
{
    lnyc[j] = log(y[j]-c);
}
for (int j=0; j<maxcount; j++)
{
    xbar+=x[j];
    ybar+=lnyc[j];
    xybar+=x[j]*lnyc[j];
    xsqbar+=x[j]*x[j];
}
xbar=xbar/maxcount;
ybar=ybar/maxcount;
xybar=xybar/maxcount;
xsqbar=xsqbar/maxcount;
slope=(xybar-(xbar*ybar))/(xsqbar-(xbar*xbar));
intercept=ybar-(slope*xbar);
double x_dev =0;
for (int j=0; j<maxcount; j++)
{
    x_dev += sq(x[j] - xbar);
}
double y_cap[maxcount];
for (int j=0; j<maxcount; j++)
{
    y_cap[j] = slope*x[j] + intercept;
    syx += sq(y[j] - y_cap[j]);
}
std_err = sqrt(syx/(maxcount-2) );
stderr_Slope = std_err / sqrt(x_dev) ;
stderr_Intercept = stderr_Slope * sqrt(xsqbar);
b = slope;
b_err = stderr_Slope;

```

```

a = exp(intercept);
a_err = exp(stderr_Intercept);
Serial.print(" Exponential fit to the equation: Y = B*exp(C*X)+ A. \n B = ");
Serial.println(a,4);
Serial.print(" C = ");
Serial.println(b,4);
Serial.print(" A = ");
Serial.println(c,6);

//save the slope and intercept data in EEPROM

EEPROM.put(eeAddress, a);
eeAddress += sizeof(a);
EEPROM.put(eeAddress, a_err);
eeAddress += sizeof(a_err);
EEPROM.put(eeAddress, b);
eeAddress += sizeof(b);
EEPROM.put(eeAddress, b_err);
eeAddress += sizeof(b_err);
EEPROM.put(eeAddress, c);
eeAddress += sizeof(c);
EEPROM.put(eeAddress, c_err);
eeAddress += sizeof(c_err);
delay (1000);
exit(0);
}

```

Appendix B

From equation 5.2.5, the total absorbance of light at wavelength λ_1 is,

$$A(\lambda_1) = \epsilon_{\text{Hb,A1c}}(\lambda_1) * l * X_{\text{Hb,A1c}} + \epsilon_{\text{Hb,Non A1c}}(\lambda_1) * l * X_{\text{Hb,Non A1c}} \quad (\text{a})$$

Similarly, at wavelength λ_2 ,

$$A(\lambda_2) = \epsilon_{\text{Hb,A1c}}(\lambda_2) * l * X_{\text{Hb,A1c}} + \epsilon_{\text{Hb,Non A1c}}(\lambda_2) * l * X_{\text{Hb,Non A1c}} \quad (\text{b})$$

The molar absorption coefficients are depended on the wavelength, but the path length and concentrations are independent of the wavelength (λ). At a fixed concentration (x) and wavelength (λ), the change in absorbance with change in path length (l) is given as follows:

$$\delta A(\lambda) = \delta(\epsilon_{\text{Hb,A1c}}(\lambda) * l * X_{\text{Hb,A1c}} + \epsilon_{\text{Hb,Non A1c}}(\lambda) * l * X_{\text{Hb,Non A1c}}) \quad (\text{c})$$

In humans the pulse pressure leads to the change in the diameter of the arterioles in tissues [34]. Therefore, there is a change in path length leading to a change in the absorbance [35]. The path length change is same for both glycosylated and non-glycosylated hemoglobin,

$$\delta A(\lambda) = (\epsilon_{\text{Hb,A1c}}(\lambda) * x_{\text{Hb,A1c}} + \epsilon_{\text{Hb,Non A1c}}(\lambda)x_{\text{Hb,Non A1c}}) * \delta l \quad (\text{d})$$

The R parameter is given by the ratio of change in absorbance as the path length changes at wavelengths λ_1 and λ_2 . From the equations, it is given by:

$$R = \frac{\delta A_{\lambda_1}}{\delta A_{\lambda_2}} = \frac{(\epsilon_{\text{Hb,A1c}}(\lambda_1) * x_{\text{Hb,A1c}} + \epsilon_{\text{Hb,Non A1c}}(\lambda_1) * x_{\text{Hb,Non A1c}}) * \delta l}{(\epsilon_{\text{Hb,A1c}}(\lambda_2) * x_{\text{Hb,A1c}} + \epsilon_{\text{Hb,Non A1c}}(\lambda_2) * x_{\text{Hb,Non A1c}}) * \delta l} \quad (\text{e})$$

$$R = \frac{\epsilon_{\text{Hb,A1c}}(\lambda_1) * x_{\text{Hb,A1c}} + \epsilon_{\text{Hb,Non A1c}}(\lambda_1) * x_{\text{Hb,Non A1c}}}{\epsilon_{\text{Hb,A1c}}(\lambda_2) * x_{\text{Hb,A1c}} + \epsilon_{\text{Hb,Non A1c}}(\lambda_2) * x_{\text{Hb,Non A1c}}} \quad (\text{f})$$

R parameter estimated from the measurements of transmitted light intensity (I) and incident light intensity (I_0) is given by:

$$R = \frac{\delta A_{\lambda_1}}{\delta A_{\lambda_2}} = \frac{\delta \left[\ln \frac{I}{I_0} \right]_{\lambda_1}}{\delta \left[\ln \frac{I}{I_0} \right]_{\lambda_2}} = \frac{\left[\ln \frac{I(l_1)}{I_0(l_1)} - \ln \frac{I(l_2)}{I_0(l_2)} \right]_{\lambda_1}}{\left[\ln \frac{I(l_1)}{I_0(l_1)} - \ln \frac{I(l_2)}{I_0(l_2)} \right]_{\lambda_2}} = \frac{\ln \frac{I(l_1)}{I(l_2)}_{\lambda_1}}{\ln \frac{I(l_1)}{I(l_2)}_{\lambda_2}} \quad (\text{g})$$

Here, l_1 and l_2 are the two path lengths for which the change in absorbance is calculated. In our device, $I_0(l_1) = I_0(l_2)$ at both wavelengths λ_1 and λ_2 .

Therefore the % HbA1c is given by:

$$\% \text{HbA1c} = \frac{x_{\text{Hb,A1c}}}{x_{\text{Hb,A1c}} + x_{\text{Hb,Non A1c}}} * 100 \quad (\text{h})$$

The molar concentration of glycosylated hemoglobin ($x_{\text{Hb,A1c}}$) and non-glycosylated hemoglobin

($x_{\text{Hb,NonA1c}}$) in terms of % HbA1c are given by:

$$x_{Hb,A1c} = \frac{\%Hb,A1c}{100} * x_{Hb} \quad (i)$$

$$x_{Hb,Non A1c} = \left(1 - \frac{\%Hb,A1c}{100}\right) * x_{Hb} \quad (j)$$

By substituting the molar concentration from equation (i) and (j) in equation (f), we get:

$$R = \frac{\epsilon_{Hb,A1c}(\lambda1) * \frac{\%Hb,A1c}{100} * x_{Hb} + \epsilon_{Hb,Non A1c}(\lambda1) * \left(1 - \frac{\%Hb,A1c}{100}\right) * x_{Hb}}{\epsilon_{Hb,A1c}(\lambda2) * \frac{\%Hb,A1c}{100} * x_{Hb} + \epsilon_{Hb,Non A1c}(\lambda2) * \left(1 - \frac{\%Hb,A1c}{100}\right) * x_{Hb}}$$

x_{Hb} cancels out in numerator and denominator and rearrange the expression,

$$R = \frac{\epsilon_{Hb,Non A1c}(\lambda1) + (\epsilon_{Hb,A1c}(\lambda1) - \epsilon_{Hb,Non A1c}(\lambda1)) * \frac{\%Hb,A1c}{100}}{\epsilon_{Hb,Non A1c}(\lambda2) + (\epsilon_{Hb,A1c}(\lambda2) - \epsilon_{Hb,Non A1c}(\lambda2)) * \frac{\%Hb,A1c}{100}}$$

Thus, the percentage of glycosylated hemoglobin is given by,

$$\% HbA1c = \frac{\epsilon_{Hb,NonA1c}(\lambda1) - R * \epsilon_{Hb,NonA1c}(\lambda2)}{R * (\epsilon_{Hb,NonA1c}(\lambda2) - \epsilon_{HbA1c}(\lambda2)) - (\epsilon_{Hb,NonA1c}(\lambda1) - \epsilon_{HbA1c}(\lambda1))} * 100$$

Appendix C

The total absorbance of glycohemoglobin A1c is due to both glycosylated and non-glycosylated hemoglobin as follows:

$$A = A_{Hb,A1c} + A_{Hb,Non A1c}$$

$$\epsilon_{Hb} * l * x_{Hb} = \epsilon_{Hb,A1c} * l * x_{Hb,A1c} + \epsilon_{Hb,Non A1c} * l * x_{Hb,Non A1c}$$

$$\epsilon_{Hb} * x_{Hb} = \epsilon_{Hb,A1c} * x_{Hb,A1c} + \epsilon_{Hb,Non A1c} * x_{Hb,Non A1c} \quad (k)$$

Substituting equations (i) and (j) from Appendix A, in equation (k), and cancelling x_{Hb} on both sides we get:

$$\epsilon_{Hb} = \epsilon_{Hb,A1c} * \frac{\%Hb,A1c}{100} + \epsilon_{Hb,Non A1c} * \left(1 - \frac{\%Hb,A1c}{100}\right)$$

$$\epsilon_{\text{Hb,A1c}} = \frac{100 * \epsilon_{\text{Hb}} - \epsilon_{\text{Hb,Non A1c}} * (100 - \% \text{Hb,A1c})}{\% \text{HbA1c}}$$

5.6 Chapter Summary

We designed and assembled an optical sensor for estimating the percentage of HbA1c in hemoglobin. A multivariable regression model is used to predict the value of molar absorption coefficient of HbA1c at the wavelengths of 535 nm and 593 nm. The working of our prototype is tested by using a chemical assay of HbA1c called Control FD Glycohemoglobin A1c Level-2 that is commercially purchased from Audit MicroControls (Product No. K061M-6, Lot No. 06621). It is a reference control consisting of human blood-based solutions intended to simulate human blood samples containing HbA1c. Various FDA approved laboratories with different instruments and reagents have estimated the percentage of HbA1c in this chemical marker and reported it to be in the range from 8-13 percentage with a mean around 10 %. It is observed that the final percentage values of HbA1c in this marker calculated using our proposed prototype is in close agreement with the measurements reported by other laboratories. Our method and the optical sensor under consideration, proves to be a promising step toward non-invasively estimating the long-term glycemic state in diabetic patients.

5.7 References

1. World Health Organization, "Global report on diabetes," p. 88, 2016. ISBN: 9789241565257
2. C. Chen, Q. Xie, D. Yang, H. Xiao, Y. Fu, Y. Tan and S. Yao, "Recent advances in electrochemical glucose biosensors: a review," *RCS Advances*, vol. 3, no. 14, p. 4473–4491, 2013. <http://dx.doi.org/10.1039/C2RA22351A>
3. Bhandodkar and J. Wang, "Non-invasive wearable electrochemical sensors: a review," *Trends in Biotechnology*, vol. 32, no. 7, pp. 363-371, 2014. <https://doi.org/10.1016/j.tibtech.2014.04.005>
4. S. Sharma, Z. Huang, M. Rogers, M. Boutelle and A. E. Cass, "Evaluation of a minimally invasive glucose biosensor for continuous tissue monitoring," *Analytical and Bioanalytical Chemistry*, vol. 408, no. 29, pp. 8427-8435, 2016. <https://doi.org/10.1007/s00216-016-9961-6>

5. Kagie, D. K. Bishop, J. Burdick, J. T. La Belle, R. Dymond, R. Felder and J. Wang, "Flexible Rolled Thick-Film Miniaturized Flow-Cell for Minimally Invasive Amperometric Sensing," *Electroanalysis*, vol. 20, no. 14, pp. 1610-1614, 2008.
<https://doi.org/10.1002/elan.200804253>
6. M. Li, X. Bo, Z. Mu, Y. Zhang and L. Guo, "Electrodeposition of nickel oxide and platinum nanoparticles on electrochemically reduced graphene oxide film as a nonenzymatic glucose sensor," *Sensors and Actuators B: Chemical*, vol. 192, pp. 261-268, 2014.
<https://doi.org/10.1016/j.snb.2013.10.140>
7. S. Mandal, M. Marie, A. Kuchuk, M. O. Manasreh, and M. Benamara, "Sensitivity enhancement in an in-vitro glucose sensor using gold nanoelectrode ensembles", *Journal of Materials Science: Materials in Electronics*, vol. 28, no. 7, pp. 5452-5459, 2017.
<https://doi.org/10.1007/s10854-016-6207-5>
8. E. C. Rama, A. Costa-Garcia and M. T. Fernandez-Abedul, "Pin-based electrochemical glucose sensor with multiplexing possibilities," *Biosensors and Bioelectronics*, vol. 88, pp. 34-40, 2017. <https://doi.org/10.1016/j.bios.2016.06.068>
9. D. G. Jung, D. Jung and S. H. Kong, "A Lab-on-a-Chip-Based Non-Invasive Optical Sensor for Measuring Glucose in Saliva," *Sensors*, vol. 17, no. 11, p. 2607, 2017.
<https://doi.org/10.3390/s17112607>
10. D. Bruen, C. Delaney, L. Florea, and D. Diamond, "Glucose sensing for diabetes monitoring: Recent developments," *Sensors*, vol.17, no. 8, pp. 1866, 2017.
<http://doi.org/10.3390/s17081866>
11. M. J. Tierney, J. A. Tamada, R. O. Potts, L. Jovanovic and S. Garg, "Clinical evaluation of the GlucoWatch® biographer: a continual, non-invasive glucose monitor for patients with diabetes," *Biosensors & Bioelectronics*, vol. 16, no. 9-12, p. 621–629, 2001.
[https://doi.org/10.1016/S0956-5663\(01\)00189-0](https://doi.org/10.1016/S0956-5663(01)00189-0)
12. J. D. Lane, D. M. Krumholz, R. A. Sack and C. Morris, "Tear Glucose Dynamics in Diabetes Mellitus," *Current Eye Research*, vol. 31, pp. 895-901, 2006.
<https://doi.org/10.1080/02713680600976552>
13. J. Kim, et al, "Wearable smart sensor systems integrated on soft contact lenses for wireless ocular diagnostics," *Nature Communications*, vol. 8, p. 14997, 2017.
<https://doi.org/10.1038/ncomms14997>
14. M. S. Talary, F. Dewarrat, D. Huber and A. Caduff, "In vivo life sign application of dielectric spectroscopy and non-invasive glucose monitoring," *Journal of Non-Crystalline Solids*, vol. 353, no. 47-51, pp. 4515-4517, 2007.
<https://doi.org/10.1016/j.jnoncrysol.2007.03.038>
15. M. A. Arnold and G. W. Small, "Noninvasive Glucose Sensing," *Analytical Chemistry*, vol. 77, pp. 5429-5439, 2005. <https://doi.org/10.1021/ac050429e>

16. Weykamp, C. "HbA1c: A Review of Analytical and Clinical Aspects," *Annals of Laboratory Medicine*, vol. 33, no. 6, pp. 393–400, 2013. <http://doi.org/10.3343/alm.2013.33.6.393>
17. R. J. Koenig and A. Cerami, "Hemoglobin A1c and diabetes mellitus," *Annual Review of Medicine*, vol. 31, pp. 29-34, 1980. <https://doi.org/10.1111/j.1365-2141.1978.tb07101.x>
18. K. P. Peterson, J. G. Pavlovich, R. Little, J. England and C. M. Peterson, "What is hemoglobin A1c? An analysis of glycated hemoglobins by electrospray ionization mass spectrometry," *Clinical Chemistry*, vol. 44, no. 9, pp. 1951-1958, 1998. ISSN: 1530-8561
19. R. Koenig, C. Peterson, R. Jones, C. Saudek, M. Lehrman and A. Cerami, "Correlation of glucose regulation and hemoglobin A1c in diabetes mellitus," *The New England Journal of Medicine*, vol. 295, no. 8, pp. 417-420, 1976. ISSN: 0028-4793
20. E. J. Gallagher, D. L. Roith and Z. Bloomgarden, "Review of hemoglobin A1c in the management of diabetes," *Journal of Diabetes*, vol. 1, pp. 9-17, 2009. <https://doi.org/10.1111/j.1753-0407.2009.00009.x>
21. D. M. Nathan et al, "Translating the A1C assay into estimated average glucose values," *Diabetes Care*, vol. 31, no. 8, pp. 1473-1478, 2008. <https://doi.org/10.2337/dc08-0545>
22. Audit MicroControls, "Control FD Glycohemoglobin A1c," [Online]. Available: <http://www.auditmicro.com/control-fd-glycohemoglobin-a1c.html>. [Accessed 13 March 2018].
23. C. L. Hardin, and Luisa Maffi, "Color Categories in Thought and Language", p. 297, 1997, ISBN 9780521498005
24. D. W. Ball, "Field Guide to Spectroscopy", Bellingham: SPIE Press, 2006. ISBN: 9780819463524
25. E. D. Chan, M. M. Chan and M. M. Chan, "Pulse oximetry: understanding its basic principles facilitates appreciation of its limitations," *Respiratory Medicine*, vol. 107, pp. 789-799, 2013. <https://doi.org/10.1016/j.rmed.2013.02.004>
26. R. N. Pittman, "Regulation of Tissue Oxygenation", in *Colloquium Series on Integrated Systems Physiology: From Molecule to Function*, San Rafael (CA), Morgan & Claypool Life Sciences, 2011. ISBN: 9781615041770. <http://dx.doi.org/10.4199/C00029ED1V01Y201103ISP017>
27. S. Prahl, "Tabulated Molar Extinction Coefficient for Hemoglobin in Water," 4 March 1998. [Online]. Available: <https://omlc.org/spectra/hemoglobin/summary.html>. [Accessed 13 March 2018].
28. H. Zollinger, "Color Chemistry: Syntheses, Properties and Applications of Organic Dyes and Pigments", Weinheim: VCH Verlagsgesellschaft mbH, 1987. ISBN: 3906390233
29. R. Birge, "Kodak Laser Dyes", Kodak publication, 1987. ISBN 10: OCLC: 83459316

30. H. Edelhoch, "Spectroscopic Determination of Tryptophan and Tyrosine in Proteins," *Biochemistry*, vol. 6, no. 7, pp. 1948-1954, 1967. <http://dx.doi.org/10.1021/bi00859a010>
31. S. C. Gill and P. H. Hippel, "Calculation of protein extinction coefficients from amino acid sequence data," *Analytical Biochemistry*, vol. 182, pp. 319-326, 1989. [http://dx.doi.org/10.1016/0003-2697\(89\)90602-7](http://dx.doi.org/10.1016/0003-2697(89)90602-7)
32. N. C. Pace, et al., "How to measure and predict the molar absorption coefficient of a protein," *Protein Science*, vol. 4, no. 11, pp. 2411-2423, 1995. <http://dx.doi.org/10.1002/pro.5560041120>
33. R. W. Burnett, "Accurate Measurement of Molar Absorptivities," *Journal of Research of the National Bureau of Standards-A. Physics and Chemistry*, vol. 76A, no. 5, pp. 483-489, 1972. <http://dx.doi.org/10.6028/jres.076A.042>
34. M. E. Safar and H. S. Boudier, "Vascular Development, Pulse Pressure, and the Mechanisms of Hypertension," *Hypertension*, vol. 46, pp. 205-209, 2005. <http://dx.doi.org/10.1161/01.HYP.0000167992.80876.26>
35. J. T. B. Moyle, "Uses and abuses of pulse oximetry," *Archives of Disease in Childhood*, vol. 74, no. 1, pp. 77-80, 1996. <http://dx.doi.org/10.1136/adc.74.1.77>

CHAPTER 6. CONCLUSION

In this chapter, section 6.1 provides a summary of this dissertation, the limitations of the current work are pointed out in section 6.2, and the outline for the directions of possible future work is described in section 6.3.

6.1 Summary of the Dissertation

The aim of this research is to design and fabricate glucose sensors using simple and inexpensive approaches. The first research approach is the fabrication of amperometric electrochemical glucose sensors by exploiting (1) the optical properties of the semiconductors like zinc oxide (ZnO), and silicon (Si), (2) the electrical properties of metal like gold (Au), silver, titanium and platinum, and (3) the structural properties of nanostructures like nanorods and nanowires.

In this dissertation, chapter 2 focuses on the optimized recipe for the synthesis of high aspect ratio, pure, homogeneous, crystalline, hexagonal-shaped ZnO nanorods. The structural and optical characterization results are discussed in detail. The ZnO nanorods are then employed in the fabrication of a working electrode that is used in a two-electrode electrochemical cell for glucose testing. The modified working electrode (device) is characterized using the cyclic voltammetry and the amperometry methods. We report higher sensor sensitivity and faster response time compared to other published works. The quality of the ZnO nanorods play a crucial role in the adsorbing larger amounts of enzyme glucose oxidase. As a result, the electrochemical reduction oxidation reaction inside the cell lasts longer, thereby demonstrating higher oxidation potentials and resulting in higher sensor current sensitivities.

The chapter 3 introduces the concept of using Au nano-electrode ensembles (NEEs) to enhance the sensitivity of the electrochemical sensor. The Au NEEs act as individual islands of

metal that contribute to an increase in the rate of electron transfer during the electrochemical reaction. The chapter also focusses on the recipe optimization of the metal assisted chemical etching technique for synthesizing Si nanowires. This wet etching technique is a simple, rapid, and cost-effect method that allows etching of Si wafers in a controlled manner. The dimension of the nanowires to be synthesized is controlled by optimizing the etch time and the etching temperature. In this work, we observe that there is an enhancement in the sensor sensitivity after modifying the sensor working electrode with Au NEEs.

In chapter 4, we use the concept of Au NEEs in enhancing the sensitivity of ZnO nanorods based electrochemical sensor discussed in chapter 2. We report that this approach leads to the enhancement in the current sensitivity, faster response time, and lower limit of detection of electrochemical sensors. The electrical conductivity of the nanorods depends upon the degree of their crystallinity. Lower the crystal defects, lesser is the surface scattering in the nanorods, and better be the electron transport behavior during the electrochemical reaction. The sensor sensitivity results are also compared to other peer reported works on nanostructures based electrochemical sensors.

The chapters 2, 3, and 4 in this dissertation discuss different approaches for fabricating electrochemical sensors that are mostly used for invasive glucose detection. In literature, testing glucose non-invasively using optical methods have not yielded consistent results so far. Therefore, diabetic patients primarily dependent upon invasive electrochemical sensors. However, there are various disadvantages associated with the needle-based electrochemical sensors available in the market. Some of the disadvantages include (1) excessive pain, (2) damaged figure tissues, and (3) blood infections like tetanus due to the use of unclean needles.

Therefore, next we wanted to study the possibility of designing a non-invasive optical sensor for computing the long-term glycemic state in patients with diabetes and pre-diabetes.

The second research approach is discussed in chapter 5 that focusses on the design of an optical sensor based on the absorbance properties of glycated hemoglobin (HbA1c). The working of the proposed sensor is grounded on the principles of the Beer's law of optical absorption. We assembled a device using LEDs of two different wavelengths (535 nm and 593 nm), a Si photodiode, and a microcontroller that is capable of (1) measuring the molar extinction coefficient of HbA1c in hemoglobin using a multi-variable regression analysis and (2) detecting the percentage of HbA1c in hemoglobin. In our study to test the proposed sensor, we use different molar concentrations of a chemical marker of HbA1c called Control FD Glycohemoglobin A1c-Level 2 that is commercially purchased from Audit MicroControls. Inc. The photodiode output voltage values with respect to the molar concentration of the HbA1c samples is used for the molar extinction coefficient calculation. The molar extinction coefficient values of HbA1c and non-glycated hemoglobin are then used to calculate the percentage of HbA1c in total hemoglobin by means of measuring a parameter called R. The parameter R is defined as the ratio of change in absorbance as the path length changes at two different wavelengths of light source. The predicted values of HbA1c percentage obtained by our optical sensor prototype are in close agreement with the anticipated results. Our study of the possibility of designing a portable HbA1c optical sensor proves to be a step towards the non-invasive measurement of long-term glycemic state in diabetic and pre-diabetic patients.

6.2 Research Limitations and Recommendations

Besides ZnO nanorods and Si nanowires, titanium oxide nanotubes were also synthesized to attempt the fabrication of electrochemical glucose sensor. We used the electrochemical

anodic oxidation technique for synthesizing (1) nanoporous and (2) free standing titanium oxide nanotubes from commercial foils of pure titanium with a thickness of about 250 μm . However, the limitation we faced in the process of fabricating a working electrode for the electrochemical cell was that the thin titanium foils were not sturdy enough to act as a substrate by itself. Also, we could not find a good approach to transfer the titanium oxide nanotubes on to a glass substrate without damaging the nanostructures.

The metal assisted chemical etching (MACE) technique was used for the synthesis of Si nanowires. In this method, thoroughly clean Si wafers are immersed in a low ratio (1:10) solution of hydrofluoric (HF) acid and deionized water. Also, the etching solution used for the MACE method is a solution of silver nitrate (AgNO_3) and HF acid. It is highly recommended to be very careful while working with HF acid. There exists no material that is completely resistant to HF acid degradation. It is a corrosive acid that is capable of dissolving any oxide. Also, there is no concentration of HF that could be called safe. It is advised to have the commercial Calgonate Gel (calcium gluconate) handy while using HF acid during your research in your laboratory.

The electrochemical sensor technology for glucose detection began in 1962, with the sensor proposed by Clark and Lyons. Since then, electrochemical glucose sensors have emerged as a topic for research because of the low-cost, fast time-response, operational simplicity, and the robust nature. However, there are disadvantages associated with electrochemical sensors and one of the major disadvantage is the need for the extraction of blood via sharp needles. Electrochemical glucose sensors are invasive in nature that leads to excessive pain, damaged finger tissues and high risks of blood infections like tetanus, Human immunodeficiency virus (HIV), and Hepatitis C. Another disadvantage of using electrochemical sensors is their

reusability. In this research, we start with numerous samples of ZnO nanorods or Si nanowires synthesized together, under the same temperature, pressure, and time conditions. Few of these samples were used for characterization purposes while the others were used in device fabrication and testing. Here, we make an assumption that all samples depict consistent structural and optical properties before employing them in the device fabrication and characterization.

6.3 Future works

The possibility of non-invasively detecting glucose will benefit pre-diabetic patients, who are ignorant about their current health conditions. The optical sensor prototype discussed in chapter 5 offers a potential method of estimating long-term glycemic levels by taking the advantage of the absorption properties of the marker compound HbA1c. However, the prototype in its current state is not completely ready for non-invasive detection. We need to further enhance the setup before conducting the finger testing experiments.

Prior to the setup enhancement, there is a need of testing our current setup using pure glycated and non-glycated blood samples. Such blood samples can be obtained from hospitals or clinics, who would also need to run invasive HbA1c tests for the same samples. The results from these invasive tests would be used to compare the results obtained from our prototype. This would be a step towards genuine validation of our sensor outputs.

Another method to validate the results from our prototype is by purchasing a HbA1c point-of-care analyzer or testing kit from a pharmacy or departmental store to run the samples for the percentage of HbA1c analysis. Such a test kit evaluation could prove to be a valid method to determine the accuracy of the proposed optical sensor.